Modelling and Numerical Treatment of Diffuse-Interface Models with Applications in Epitaxial Growth

Dissertation

zur

Erlangung des Doktorgrades (Dr. rer. nat.)

der

Mathematisch-Naturwissenschaftlichen Fakultät

der

Rheinischen Friedrich-Wilhelms-Universität Bonn

vorgelegt von

Andreas Rätz

aus

Bonn

Bonn, 2007

Angefertigt mit Genehmigung der Mathematisch-Naturwissenschaftlichen Fakultät
der Rheinischen Friedrich-Wilhelms-Universität Bonn

1. Referent: PD Dr. Axel Voigt
2. Referent: Prof. Dr. Felix Otto

Tag der Promotion:

Abstract

In this thesis, we are dealing with modelling and numerical treatment of epitaxial growth of thin crystalline films, where we concentrate on diffuse-interface approximations of two descriptions of this process. In the first part, we consider a semi-continuous model resolving atomic distances in the growth direction but being coarse grained in the lateral directions. Mathematically, this leads to a free boundary problem proposed by Burton, Cabrera and Frank for steps separating terraces of different atomic heights coupled to a diffusion equation for the adatom (adsorbed atom) concentration fulfilling certain boundary conditions at the steps. For this sharp-interface model, a diffuse-interface approximation can be given by a viscous Cahn-Hilliard equation, which is based on a Ginzburg-Landau free energy. Great emphasis is put on the incorporation of an Ehrlich-Schwoebel barrier — a higher energy barrier for attachment to a step down, which leads to a jump in the adatom concentration at the steps — as well as diffusion along step edges and anisotropic effects into a diffuse-interface model. We provide a justification by matched asymptotic expansions formally showing the convergence of the diffuse-interface model towards the sharp-interface model as the interface width shrinks to zero. The numerical treatment of the viscous Cahn-Hilliard is based on a semi-implicit finite element discretization, where an adaptive strategy of local mesh refinement and coarsening has been applied. Computational results include the numerical reproduction of the results of the asymptotic analysis in one dimensional situations, the investigation of the stability of a circular island and simulations of anisotropic island growth and spiral growth.

The second model is continuous in all directions. We thereby assume that the interface between the film and the vapour is represented by a smooth surface, whose evolution is given by a geometric law that combines surface diffusion and interface kinetics, which can again be approximated by a viscous Cahn-Hilliard equation. In principle, we reuse the previous numerical approach and validate it with an investigation of an instability caused by an additional elastic energy. Further examples show the smoothing property for closed curves and surfaces as well as the evolution towards anisotropic shapes.

Contents

Chapter 1

Introduction

This work is concerned with modelling and numerical aspects of thin film epitaxy, which is a technology of growing single crystals that inherit atomic structures from substrates. It produces almost defect-free, high quality materials that have a wide range of device applications. One of the most typical and important examples of thin film epitaxy is MBE (molecular beam epitaxy), where the deposition material is thermally evaporated from a source and forms a directed beam of neutral atoms inside the chamber. Due to chemical bonding, such atoms in the vapour are adsorbed by a given substrate or crystal surface. In this thesis, we are interested in two mathematical models for this process, where the first one is semi-continuous in the sense that it resolves atomic distances in the growth direction but is coarse grained in the remaining directions, whereas the second approach is continuous in all directions.

For the semi-continuous model studied in Chapter 2, we first consider a microscopic picture of a stepped surface (see Figure 1.1 for a scanning tunnelling microscopy (STM) image of steps on a Si(001) surface). Once adsorbed by the surface, the deposited atoms are called adatoms. Different mechanisms such as adatom diffusion and desorption, deposition of atoms as well as attachment of adatoms from terraces to steps leading to a movement of steps and detachment from steps to terraces play a role (see Figure 1.2 for a schematic microscopic picture). Furthermore, coalescence of a finite number of adatoms may lead to the nucleation of a new terrace or island and thus contribute to the growth of the film. Burton, Cabrera and Frank [BCF51] proposed a model ("BCF model") for this situation, which is coarse grained in the lateral directions but still discrete in the growth direction (see e.g. [Kru05, MK04, PV98] for overviews on the BCF model). To be more precise, the steps are thought of as continuous curves separating terraces of different atomic height. Then, one is interested in a free boundary problem, which is similar to the Stefan problem modelling solidification processes and includes a diffusion equation for a continuous adatom concentration $\rho : \Omega \times I \to \mathbb{R}$ with some domain $\Omega \subset \mathbb{R}^2$ and time interval $I = [0, t_{\text{end}}]$. The adatom concentration is then coupled to the movement of the steps whose normal velocities are mainly given by the sum of the adatom fluxes into the step from the upper and lower terraces, respectively. On the

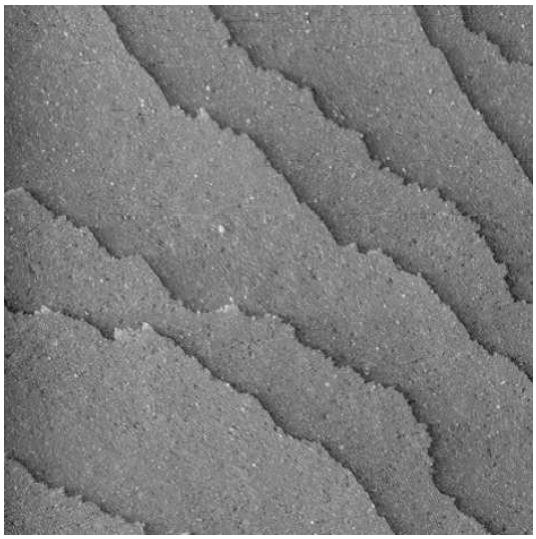

Figure 1.1: STM image of a stepped Si(001)-surface ($\approx 355\text{nm} \times 355\text{nm}$) [Polop, Bleikamp, Michely, I. Phys. Institut, RWTH Aachen].

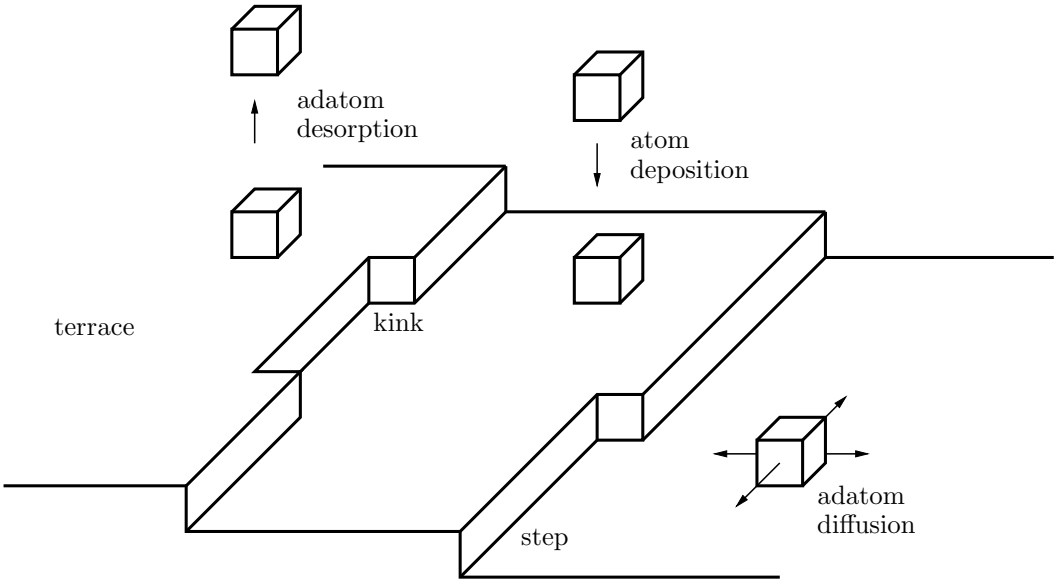

Figure 1.2: Microscopic processes on a stepped surface.

boundaries, we assume in this work either a condition related to the Gibbs-Thomson boundary condition in the context of a Stefan problem including the curvature of the step, or we study the influence of the so-called Ehrlich-Schwoebel (ES) barrier (the denomination going back to [EH66, SS66, Sch69]), a higher energy barrier that must be overcome by an adatom in order to attach from the upper terrace to a step. This is illustrated in Figure 1.3 showing the potential V having a maximum corre-

sponding to an uncomfortable position with few neighbours that has to be crossed for attachment to a step down. In the BCF model, this asymmetry in attachment

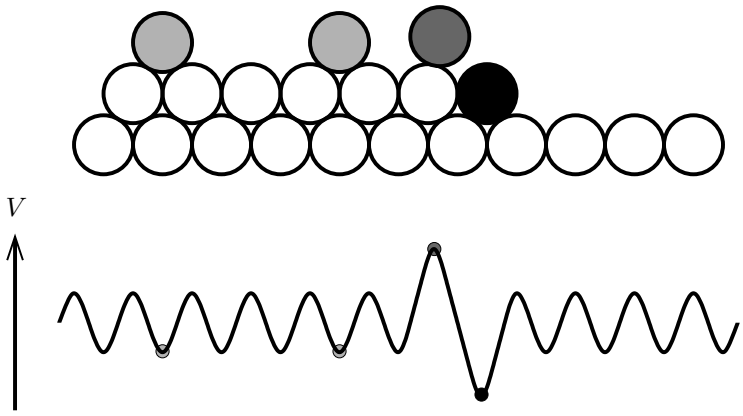

Figure 1.3: Ehrlich Schwoebel barrier.

is modelled by an asymmetry in the so-called kinetic boundary conditions, where one assumes that the adatom fluxes from the upper and lower terraces into the step are each proportional to the deviation from the thermodynamic equilibrium with different proportionality factors, which display the asymmetry in the attachment. This choice of boundary conditions leads to a discontinuity of the adatom density at the step. During growth, the ES barrier may be responsible for a step meandering instability [BZ90] of a train of straight steps, which is due to the fact that diffusing adatoms prefer attachment to a protrusion of a non-straight step as well as attachment from the lower terrace, which leads to an enhancement of the protrusion. A second consequence of the asymmetry in attachment on a more macroscopic scale is a roughening of the growing film caused by reduced filling of valleys and enhanced nucleation on top of mounds, where the adatom concentration is increased. Moreover, during growth the ES barrier stabilizes step trains with respect to step bunching perpendicular to the steps.

For numerical reasons, we study a diffuse-interface approximation of this free boundary problem, where the discrete function counting the atomic monolayers is smeared out on a length of $\mathcal{O}(\varepsilon)$. This approach is based on a Ginzburg-Landau free energy for the smeared out height function ϕ. The evolution of the steps given by the evolution of ϕ is coupled to a diffusion equation for the adatom density ρ. This leads to a viscous Cahn-Hilliard equation (an interpolation between Allen-Cahn [AC79] and Cahn-Hilliard equation [CH58] proposed by Novick-Cohen [NC88]), which can be written as a system of two partial differential equations of second order. One numerical advantage of this ansatz compared to sharp interface approaches (see e.g. [BHL$^+$04, BHV05]) is then that one can use the same grid for the discretization of ρ and ϕ. In addition, such a diffuse-interface approach automatically handles topological changes such as coalescence and vanishing of terraces. For the approximation of the BCF model with thermodynamic boundary conditions, diffuse-interface models

have been treated in [LM94, KP98, RV04], and following [CENC96] and introducing a degenerate mobility (increased to $\mathcal{O}(\varepsilon^{-1})$ in the diffuse-interface region) one can treat in a diffuse-interface model an additional term in the velocity law of the BCF model mainly proportional to the second tangential derivative of the curvature [RV05] modelling the diffusion of atoms along a step edge . For the approximation of the BCF model with kinetic boundary conditions, the asymmetry in the attachment from upper and lower terraces, respectively, is modelled by a degenerate (decreased to $\mathcal{O}(\varepsilon)$ in the diffuse-interface region) and asymmetric mobility function [OPR$^+$04]. Thereby, the degeneracy is crucial for the resolution of the jump in the adatom concentration at the step in a diffuse-interface approximation. The incorporation of edge diffusion into a diffuse-interface model approximating a BCF model with kinetic boundary conditions is not treated in this thesis. For both types of boundary conditions, we introduce a model which accounts for anisotropic attachment kinetics, mobilities and step stiffnesses.

After introducing the details of this approach in Section 2.1, we combine in Section 2.2 the procedure of [RV05] and [OPR$^+$04] with the anisotropic one presented in [RRV06] and provide a justification by matched asymptotic expansions formally showing the convergence towards the desired sharp-interface limits as the width of the diffuse interface shrinks to zero. In Section 2.3, a semi-implicit finite element (FEM) discretization — implemented in the FEM toolbox AMDiS [VV07] — of the diffuse-interface model is described including an adaptive strategy of local mesh refinement and coarsening. As a numerical test, we reproduce the results of the asymptotic analysis for one dimensional examples, where analytic solutions of the BCF model are available. After the numerical investigation of the stability of a circular epitaxial island and anisotropic island growth, we finally obtain similar results as Karma and Plapp [KP98] for spiral growth and, furthermore, study the influence of edge diffusion and an Ehrlich-Schwoebel barrier on the shape of growth spirals.

In the second approach of modelling epitaxial growth processes presented in Chapter 3, we assume that the growth of the film is described by the evolution of a continuous interface between vapour and solid. Thus, the interface is a $(d-1)$-dimensional hypersurface in $\mathbb{R}^d$. Based on Mullins' work [Mul57], where he derived the isotropic surface diffusion equation stating that the normal velocity is proportional to the surface Laplacian (Laplace-Beltrami operator) of the mean curvature, Cahn and Taylor [CT94] introduced a growth law which combines surface diffusion with interface kinetics (see also [GJ02]). In [CENC96], a matched asymptotic analysis has been performed in order to formally show that a Cahn-Hilliard equation with a degenerate mobility function (being zero outside and increased to $\mathcal{O}(\varepsilon^{-1})$ inside the diffuse-interface region) can approximate motion by the surface Laplacian of mean curvature as $\varepsilon \to 0$. Taylor and Cahn [TC94] extended this diffuse-interface model to a viscous Cahn-Hilliard equation accounting for anisotropic as well as kinetic effects. Asymptotic expansions have been performed for this model in [RRV06].

In Section 3.1, we briefly describe the sharp- and diffuse-interface models and some basic properties. In Section 3.2, some details of the discretization of the vis-

cous Cahn-Hilliard equation in this application are described. We validate both the numerical and the modelling approach by investigating the stability of a flat interface, where a (prescribed) elastic energy (as proposed in [BMN05]) is incorporated into the model leading to an instability. With this instability, we compare for curves numerical results of the viscous Cahn-Hilliard equation with numerical results of sharp-interface simulations and analytic results of a linear stability analysis for the two extreme cases motion by mean curvature and motion by surface diffusion. As a second example, we consider the smoothing property of the model starting with different closed curves and surfaces including a simulation showing a pinch-off predicted by sharp-interface simulations in [BMN05]. Furthermore, numerical results showing anisotropic evolutions of curves and surfaces are presented.

Acknowledgements

First and foremost, I would like to express my gratitude to PD Dr. Axel Voigt for sparking my interest in this subject and also for dedicated support. In addition, I am grateful to Professor Felix Otto for many interesting and helpful discussions on this topic during the last four years.

Furthermore, I would like to thank Professor Joachim Krug and Professor Thomas Michely for the inspiring collaboration.

I am also grateful to the members of the Crystal Growth group at the caesar research center for helpful discussions, patient AMDiS support and many useful hints during the last years.

Moreover, financial support from the caesar research center, Bonn, and from the Deutsche Forschungsgemeinschaft through the Priority Program SPP1095 “Analysis, Modeling and Simulation of Multiscale Problems” is acknowledged.

Chapter 2

Diffuse-Interface Approximation of Discrete-Continuous Models

In this chapter, we consider a model proposed by Burton, Cabrera and Frank [BCF51], which is semi-continuous in the sense that it resolves atomic distances in the growth direction but is coarse grained in the lateral directions. That means that we study islands and terraces of discrete atomic heights bounded by continuous curves. Mathematically, this leads to a free boundary problem which is closely related to the Stefan-problem arising in the description of solidification processes and to the Mullins-Sekerka model appearing in phase separation of alloys.

In Section 2.1, we first briefly introduce the sharp-interface model, before we propose diffuse-interface approximations for different types of boundary conditions at the free boundary, which lead to different choices of mobility functions. Justification of this approach is given by matched asymptotic expansions in Section 2.2 and by numerical results in Section 2.3 including a comparison with analytic solutions of the sharp-interface model, investigations of the stability of a circular island as well as studies concerning anisotropic island growth and spiral growth.

2.1 Model Description

Here, we briefly describe the sharp-interface model studied in this chapter, before a diffuse-interface approximation of this model is proposed. For overviews on the sharp-interface model, we refer to [MK04, Kru05, PV98]. Reviews on Cahn-Hilliard systems can be found in [Ell89, NC98, Fif00], whereas overviews on phase-field modelling can be found in [Che02, BWBK02], for example.

2.1.1 Sharp-Interface Model

On an atomic level, we consider a situation, where atoms are deposited from the vapour phase onto a solid surface. Once adsorbed by the surface, these atoms are called adatoms and are able to diffuse on the surface searching for an energetically

favourable position. In this scenario, processes such as atom deposition and diffusion, desorption of adatoms as well as attachment of adatoms from terraces to steps and detachment from steps to terraces are of interest (see Figure 1.2). An additional aspect is related to nucleation of new islands, which is not theoretically studied in this work.

Steps and Terraces

In this chapter, we consider the so-called BCF model introduced by Burton, Cabrera and Frank [BCF51]. This model is discrete in the growth direction and continuous in the lateral directions (see Fig. 2.1) and studied in a time interval $[t_0, t_{\text{end}}]$. Projecting the film surface normal to the growth direction, we obtain a fixed domain $\Omega \subset \mathbb{R}^2$. Introducing the discrete function $\phi_0 = \phi_0(x,t)$ counting the atomic monolayers at

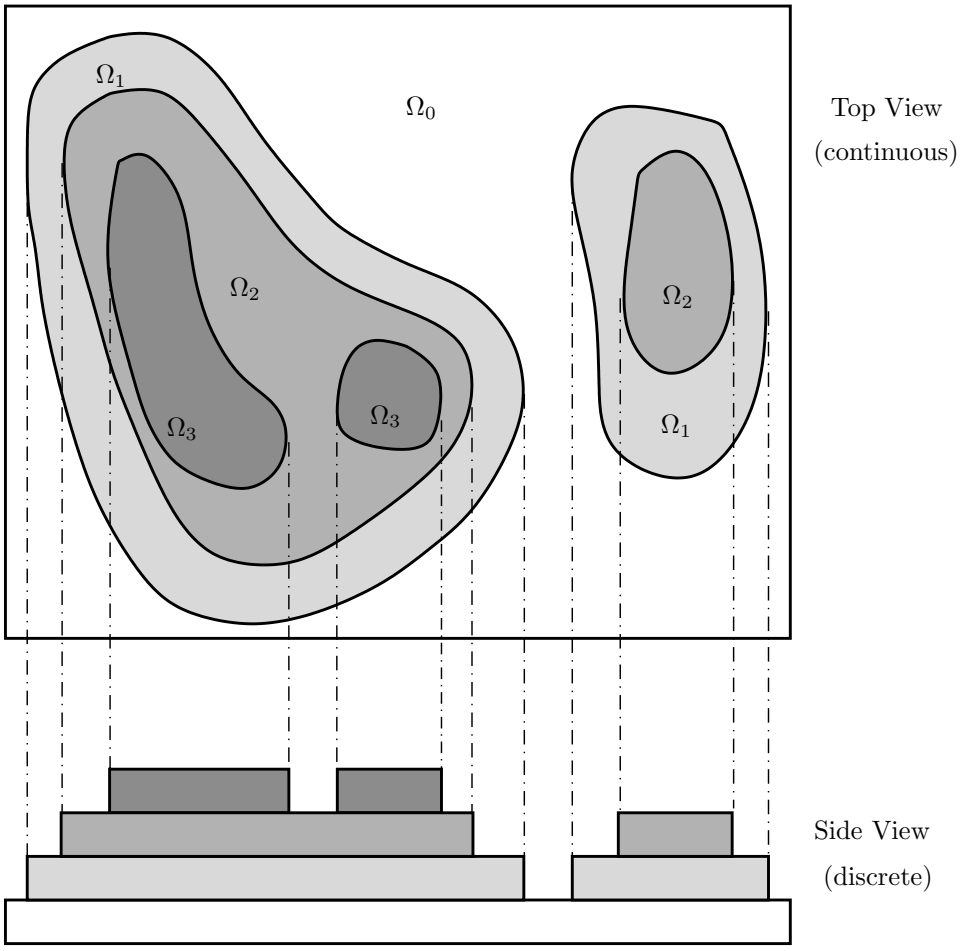

Figure 2.1: Discrete-continuous model for epitaxial islands.

point $x \in \Omega$, we can define the terraces $\Omega_i = \Omega_i(t) := \{x \in \Omega : \phi_0(x,t) = i\}$ of atomic height $i \in \{0, \ldots, K\}$ for a number $K \in \mathbb{N}$. The corresponding island

or terrace boundaries $\Gamma_i = \Gamma_i(t)$ are then given by $\Gamma_i(t) = \overline{\Omega_{i-1}(t)} \cap \overline{\Omega_i(t)}$, $i \in \{1, \dots, K\}$. Furthermore, we denote by $N_i = N_i(t)$, $v_i = v_i(t)$ and $\kappa_i = \kappa_i(t)$ the normal, the normal velocity and the curvature of the boundary $\Gamma_i(t)$. Thereby, we use the conventions that N_i points from the upper terrace Ω_i to the lower terrace Ω_{i-1} and the curvature κ_i of the step is positive, if a closed upper island terrace Ω_i is convex or, if, in a step flow case, the interface is given by the graph of a concave function, and the normal N_i has a positive x_2-component (see also Figure 2.2).

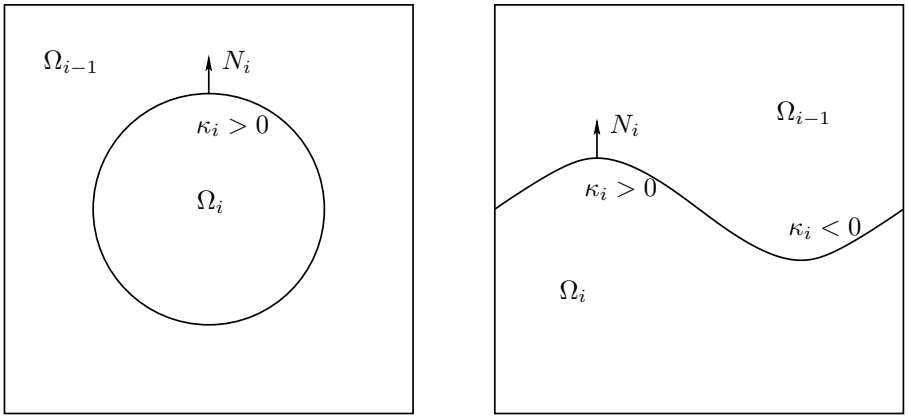

Figure 2.2: Sign conventions for normal N_i and curvature κ_i for islands (left) and step flow (right).

Step Free Energy

Now, we want to present some details on the thermodynamic properties of steps, which are described by the energy

$$\mathcal{S}_\varphi(\Gamma) := \int_\Gamma \varphi(N)\,\mathrm{d}s \tag{2.1}$$

of a step Γ, where $\mathrm{d}s$ denotes the line element and $\varphi = \varphi(N)$ the specific surface free energy depending on the normal N of Γ. The functional derivative with respect to Γ is normal (see Lemma 2 in Section 3.1.1) and yields

$$\frac{\delta \mathcal{S}_\varphi}{\delta \Gamma} \cdot N = (\varphi + \varphi'')\kappa = \tilde{\varphi}\kappa$$

including the step stiffness

$$\tilde{\varphi} = \varphi + \varphi'',$$

where φ' denotes the derivative

$$\varphi'(N) := \frac{\mathrm{d}}{\mathrm{d}\theta}\phi((\cos\theta, \sin\theta)) \quad \text{for} \quad N = (\cos\theta, \sin\theta), \quad \theta \in [0, 2\pi).$$

Let $\tilde{\Omega}$ denote the area of an adsorption site. The step chemical potential $\mu_c = \tilde{\Omega}\tilde{\varphi}\kappa$ is then the free energy change upon adding an atom to the step.

In order to mathematically describe equilibrium shapes of islands related to the step free energy (2.1), we introduce a dimensionless anisotropy function $\gamma : \mathrm{S}^1 \to \mathbb{R}$ satisfying $\varphi = \mu_1 \gamma$ for some dimensional constant quantity μ_1. Concerning the variational problem

$$\text{(2.2)} \qquad \text{Minimize} \quad \mathcal{S}_\gamma(\Gamma) = \int_\Gamma \gamma(N)\,\mathrm{d}s \quad \text{such that} \quad |\Omega| := \int_\Omega \mathrm{d}x = \text{constant}$$

with $\Omega \subset \mathbb{R}^2$ a smooth domain satisfying $\partial\Omega = \Gamma$, it is known that the so-called Wulff set (the denomination going back to [Wul01])

$$\text{(2.3)} \qquad W_\gamma := \left\{ x \in \mathbb{R}^2 \,:\, x \cdot n \leq \gamma(n)\ \forall n \in \mathrm{S}^1 \right\}$$

is a solution of (2.2) (see e.g. [Tay78]), where, for completeness, we mention that $x \cdot y$ denotes the Euclidean standard scalar product for $x, y \in \mathbb{R}^d$. For uniqueness results, we refer to [FM91]. According to the functional derivative

$$\kappa_\gamma := \frac{\delta \mathcal{S}_\gamma}{\delta \Gamma} \cdot N = (\gamma + \gamma'')\kappa = \tilde{\gamma}\kappa,$$

leading to the weighted curvature κ_γ, one obtains that the curvature of the Wulff shape

$$\text{(2.4)} \qquad \mathcal{W}_\gamma := \partial W_\gamma$$

is inversely proportional to $\tilde{\gamma} = \gamma + \gamma''$. As a consequence, the curvature of an equilibrium island shape is inversely proportional to the stiffness $\tilde{\varphi}$.

Free Boundary Problem

For the adatom concentration $\rho = \rho(x,t)$, $(x,t) \in \Omega \times [t_0, t_{\mathrm{end}}]$, we assume the diffusion equation

$$\text{(2.5)} \qquad \partial_t \rho + \nabla \cdot J = F - \tau^{-1}\rho \quad \text{in} \quad \Omega_i$$

with deposition flux rate F, the desorption rate τ^{-1}, the divergence operator $\nabla\cdot$ and the diffusion flux

$$\text{(2.6)} \qquad J = -D\nabla\rho$$

including the diffusion coefficient D. In addition, we prescribe initial conditions $\Gamma_i(t_0) = \Gamma_i^0$ for some initial curves Γ_i^0 and $\rho(x,t_0) = \rho^0(x)$, $x \in \Omega$, for some initial adatom concentration $\rho^0 = \rho^0(x)$, $x \in \Omega$. Moreover, one assumes Dirichlet or no flux boundary conditions

$$\rho = \rho_\partial \quad \text{or} \quad \nabla\rho \cdot N = 0 \quad \text{on} \quad \partial\Omega$$

with some function $\rho_\partial = \rho_\partial(x)$, $x \in \partial\Omega$, and the outer normal N to $\partial\Omega$, or one assumes in the case of rectangular domains Ω that ρ is Ω-periodic. We set $\rho_i := \rho|_{\overline{\Omega}_i}$ and $J_i := J|_{\overline{\Omega}_i}$, and, on the boundaries Γ_i, we define the fluxes

$$J_i^- := J_i \cdot N_i - v_i\rho_i \quad \text{on} \quad \Gamma_i, \tag{2.7}$$

$$J_i^+ := -J_{i-1} \cdot N_i + v_i\rho_{i-1} \quad \text{on} \quad \Gamma_i \tag{2.8}$$

into the steps from the upper and lower terraces, respectively, and we assume for the adatom density one of the following two types of boundary conditions.

1. Thermodynamic Boundary Conditions (TBC)

$$\rho = \rho_i = \rho_{i-1} = \rho^*(1 + \tilde{\sigma}(N_i)\kappa_i) + \frac{1}{k(N_i)a}\frac{v_i}{\tilde{\Omega}} \quad \text{on} \quad \Gamma_i, \tag{2.9}$$

2. Kinetic Boundary Conditions (KBC)

$$J_i^- = ak_-(N_i)(\rho_i - \rho^*(1 + \tilde{\sigma}(N_i)\kappa_i)) \quad \text{on} \quad \Gamma_i, \tag{2.10}$$

$$J_i^+ = ak_+(N_i)(\rho_{i-1} - \rho^*(1 + \tilde{\sigma}(N_i)\kappa_i)) \quad \text{on} \quad \Gamma_i. \tag{2.11}$$

Here, ρ^* denotes the equilibrium density of a straight step and

$$\tilde{\sigma} := \frac{\tilde{\Omega}\tilde{\varphi}}{k_B\Theta}$$

the capillarity length, where k_B denotes the Boltzmann's constant and Θ the temperature. Furthermore, a is the atomic distance and $k = k(N_i)$ is a kinetic coefficient. Then, the right hand side of (2.9) is closely related to the Gibbs-Thomson boundary condition associated with the Stefan problem in the context of solidification processes. It includes the thermodynamic equilibrium

$$\rho^*(1 + \tilde{\sigma}(N_i)\kappa_i) \tag{2.12}$$

of the step. In (2.10), (2.11) $k_- = k_-(N_i)$ and $k_+ = k_+(N_i)$ denote the attachment rates from the upper and the lower terrace to the boundary, respectively, where, for simplicity, we assume

$$k_- = a_-k_0 \quad \text{and} \quad k_+ = a_+k_0 \tag{2.13}$$

for a dimensionless anisotropy function $k_0 : \mathrm{S}^1 \to \mathbb{R}$ and positive constants $a_\pm$. The boundary conditions (2.10) and (2.11) describe a balance between the adatom flux into the step and the deviation from the thermodynamic equilibrium (2.12). In the presence of an Ehrlich-Schwoebel barrier — a higher energy barrier for attachment to a step down [EH66, SS66, Sch69] —, the relation $k_+ > k_-$ models a preferred attachment from the lower terrace to the boundary.

Irrespective of the type of boundary condition, one can assume the evolution of the free boundaries Γ_i is given by

$$\frac{v_i}{\tilde{\Omega}} = J_i^- + J_i^+ + \partial_s \left(\nu(N_i) \partial_s \left(\tilde{\Omega} \tilde{\varphi}(N_i) \kappa_i + \frac{k_B \Theta}{\rho^* k(N_i) a} \frac{v_i}{\tilde{\Omega}} \right) \right) \quad \text{on} \quad \Gamma_i, \tag{2.14}$$

where the first term on the right hand side of (2.14) is due to mass conservation. In addition, ∂_s denotes the derivative with respect to arc length, and the second term is dedicated to model diffusion of adatoms along the boundaries Γ_i, where $\nu = \nu(N_i)$ denotes the mobility of this diffusion. It should be mentioned that this term is mass conserving (see Proposition 1 in Section 3.1.1) and neglected for the diffuse-interface approximation in the case of kinetic boundary conditions.

Quasi-Stationary Approximation

In the following, we will introduce several simplifications and changes in dimensions and notations, before a diffuse-interface approximation will be presented. For this purpose, we assume for the diffusion equation (2.5) a quasi-stationary approximation for the adatom concentration, which yields

$$\nabla \cdot J = F - \tau^{-1} \rho \quad \text{in} \quad \Omega_i.$$

In this regime, one neglects the convective terms in (2.7) and (2.8), and, therefore, we obtain the fluxes

$$\begin{aligned} J_i^- &= J_i \cdot N_i \quad \text{on} \quad \Gamma_i, \\ J_i^+ &= -J_{i-1} \cdot N_i \quad \text{on} \quad \Gamma_i \end{aligned}$$

appearing in the velocity formula and in the kinetic boundary conditions.

Non-Dimensional Quantities

In order to further simplify the notations, we assume $\tilde{\Omega} = a^2$ and introduce the transformations

$$x \mapsto \frac{x}{a}, \;\; \rho \mapsto a^2 \rho, \;\; D \mapsto \frac{D}{a^2}, \;\; \rho^* \mapsto a^2 \rho^*, \;\; \tilde{\sigma} \mapsto \frac{\tilde{\sigma}}{a}, \;\; \tilde{\varphi} \mapsto \frac{\tilde{\varphi}}{a}, \;\; \nu \mapsto \frac{\nu}{a}, \; F \mapsto a^2 F,$$

which means that lengths are measured in units of the atomic distance a. Furthermore, we consider non-dimensional times and assume that energies are measured in units of $k_B \Theta$. In addition, we will consider in the following the excess density $w := \rho - \rho^*$ with $w_i := w|_{\overline{\Omega}_i}$, introduce $\tilde{F} := F - \tau^{-1} \rho^*$ and denote $\tilde{F}$ with F again. Finally, we introduce $\mu := \rho^* \tilde{\sigma}$. Then, we obtain the diffusion equation

$$\nabla \cdot J = F - \tau^{-1} w \quad \text{in} \quad \Omega_i \tag{2.15}$$

with the adatom flux

$$J = -D \nabla w. \tag{2.16}$$

Furthermore, we obtain the boundary conditions

$$w = \mu(N_i)\kappa_i + \frac{1}{k(N_i)} v_i \quad \text{on} \quad \Gamma_i \tag{2.17}$$

in the TBC case and

$$J_i^- = k_-(N_i)(w_i - \mu(N_i)\kappa_i) \quad \text{on} \quad \Gamma_i, \tag{2.18}$$

$$J_i^+ = k_+(N_i)(w_{i-1} - \mu(N_i)\kappa_i) \quad \text{on} \quad \Gamma_i \tag{2.19}$$

in the KBC case. The velocity formula is now given by

$$v_i = J_i^- + J_i^+ + \partial_s \left(\nu(N_i) \partial_s \left(\tilde{\varphi}(N_i)\kappa_i + (\rho^* k(N_i))^{-1} v_i \right) \right). \tag{2.20}$$

Before we introduce a Cahn-Hilliard approximation of this model, we write

$$\mu = \mu_0 \tilde{\gamma} = \mu_0(\gamma + \gamma'') \tag{2.21}$$

with a constant quantity μ_0 and an anisotropy function $\gamma : \mathrm{S}^1 \to \mathbb{R}$, for which we assume $\gamma = 1$, if we regard the isotropic situation as a special case. Therefore and by the choice of non-dimensionalization, one can rewrite

$$\tilde{\varphi} = \tilde{\sigma} = \frac{\mu}{\rho^*} = \frac{\mu_0 \tilde{\gamma}}{\rho^*},$$

and, therefore, (2.20) reads

$$v_i = J_i \cdot N_i - J_{i-1} \cdot N_i + \partial_s \left((\rho^*)^{-1} \nu \partial_s \left(\mu\kappa_i + k^{-1} v_i \right) \right). \tag{2.22}$$

Energy Dissipation

One essential property of the BCF model with diffusion equation (2.15) and (2.16) and either thermodynamic boundary condition (2.17) or kinetic boundary conditions (2.18), (2.19) and velocity law (2.22) is that it is thermodynamically consistent in the sense that for $F = 0$, $\tau^{-1} = 0$ and no adatom flux boundary conditions on the boundary $\partial\Omega$ the total energy of the steps — which, in the isotropic case, is proportional to the total length of the steps — is reduced during time (see[OPR$^+$04])

$$\frac{\mathrm{d}}{\mathrm{d}t} \sum_{i=1}^{K} \int_{\Gamma_i} \varphi(N_i) \, \mathrm{d}s \leq 0. \tag{2.23}$$

To the author's knowledge existence results for the BCF model are only in one dimensional situations and for thermodynamic boundary conditions without edge diffusion (see e.g. [Rad91, CR92]) available. A linear stability analysis for step flow is presented in [BZ90]. The result is the morphological Bales-Zangwill instability which shows up for perturbations with small wave numbers. For circular shaped islands, there have been stability investigations performed in [Avi71, Avi72, LRV04]. Numerically, the BCF model has been investigated in a framework of a finite element method (FEM) in [BHL$^+$04] in the KBC case and in [BHV05] in the TBC case (see also [HV05b]). Level set approaches for island growth can be found in [CMK$^+$01], for example.

2.1.2 Diffuse-Interface Model

We provide a diffuse-interface approximation for this type of free boundary problems. The basic idea in this context is to introduce a small parameter $\varepsilon > 0$ and a function $\phi : \Omega \times [t_0, t_{\text{end}}] \to \mathbb{R}$ obtained by smearing out the discrete function $\phi_0 : \Omega \times [t_0, t_{\text{end}}] \to \mathbb{R}$ counting the atomic monolayers on a length scale of $\mathcal{O}(\varepsilon)$ (see Figure 2.3). This approximation is based on a Ginzburg-Landau free energy

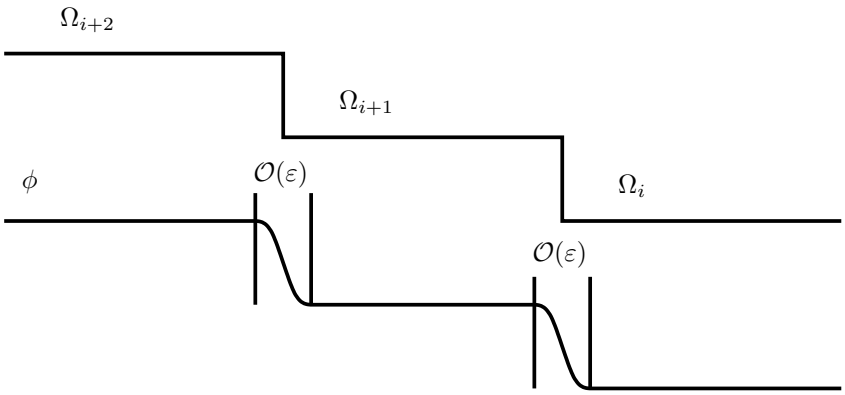

Figure 2.3: Idea of smeared out height function ϕ.

$$\mathcal{E}(\phi) := \int_\Omega E(\phi, \nabla\phi)\,\mathrm{d}x := \int_\Omega \left(\frac{1}{2}\varepsilon|\gamma\nabla\phi|^2 + \varepsilon^{-1}G(\phi)\right)\,\mathrm{d}x, \tag{2.24}$$

where the energy density $E = E(z, p) : Q \subset \mathbb{R} \times \mathbb{R}^2 \to \mathbb{R}$ contains a multi well potential $G = G(\phi)$

$$G(\phi) = 18(\phi - i)^2(\phi - (i-1))^2, \quad \phi \in [i-1, i], \quad i \in \mathbb{Z} \tag{2.25}$$

attaining its minimum $G(\phi) = 0$ in all integer values $\phi \in \mathbb{Z}$ representing the terraces (see Figure 2.4). In this context, the moving boundaries are given by the level sets

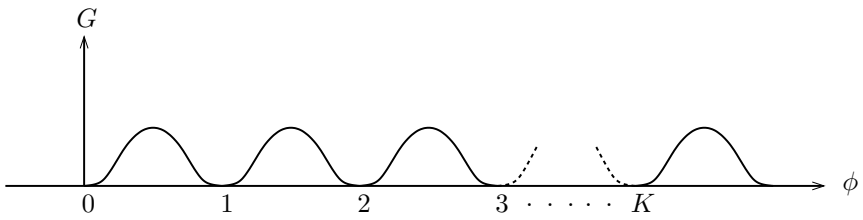

Figure 2.4: Multi well potential G.

$$\Gamma_i(t;\varepsilon) := \left\{x \in \Omega \,:\, \phi(x,t) = i - \frac{1}{2}\right\} \quad \text{for} \quad i \in \mathbb{Z}.$$

The gradient term in the free energy (2.24) accounts for the interactions between the terraces. Furthermore, it includes a function $\gamma : \mathrm{S}^1 \to \mathbb{R}$ leading to anisotropic

contributions to the free energy, where the normal to the level set $\Gamma_i(t;\varepsilon)$ is given by $n_i(\nabla\phi) := -\frac{\nabla\phi}{|\nabla\phi|}|_{\Gamma_i}$. Therefore, we have $\gamma = \gamma(-\frac{\nabla\phi}{|\nabla\phi|})$, where neither $n(\nabla\phi) := -\frac{\nabla\phi}{|\nabla\phi|}$ is defined for $\nabla\phi = 0$ nor $\hat{\gamma}(p) := \gamma(-\frac{p}{|p|})$ for $p = 0$. However, the corresponding term in the energy (2.24) includes the positively one-homogeneous function

$$\gamma_0(p) := \gamma\left(-\frac{p}{|p|}\right)|p| \quad \text{for} \quad p \in \mathbb{R}^2 \setminus \{0\}.$$

By defining $\gamma_0(0) := 0$ one obtains Lipschitz-continuity of $\gamma_0 : \mathbb{R}^2 \to \mathbb{R}$, which ensures the existence of the energy (2.24), if $\phi \in \mathrm{H}^1(\Omega)$ holds.

A diffuse-interface approximation of the quasi-stationary BCF model is then given by a viscous Cahn-Hilliard-like equation

$$\partial_t\phi + \nabla\cdot j = F - \tau^{-1}w, \tag{2.26}$$

$$j = -M_\varepsilon\nabla w, \tag{2.27}$$

$$\varepsilon\tilde{k}^{-1}\partial_t\phi = -\mu_0\frac{\delta\mathcal{E}}{\delta\phi} + w = \mu_0\left(\nabla\cdot E_p(\phi,\nabla\phi) - \varepsilon^{-1}G'(\phi)\right) + w \tag{2.28}$$

for $\phi, w : \Omega\times[t_0,t_{\mathrm{end}}] \to \mathbb{R}$, $j : \Omega\times[t_0,t_{\mathrm{end}}] \to \mathbb{R}^2$ and an initial condition $\phi(x,t_0) = \tilde{\phi}(x)$ for some $\tilde{\phi} : \Omega \to \mathbb{R}$ obtained by smearing out the discrete function $\phi_0(x,t_0)$. Moreover, one assumes Dirichlet or no flux boundary conditions

$$\phi = \phi_\partial, \quad w = w_\partial \quad \text{or} \quad \nabla\phi\cdot N = \nabla w\cdot N = 0 \quad \text{on} \quad \partial\Omega$$

for $\phi_\partial, w_\partial : \partial\Omega \to \mathbb{R}$, or one may assume Ω-periodicity of ϕ and w or a combination of these boundary conditions. In addition, the concrete choices of kinetic coefficient $\tilde{k}$ and mobility function M_ε depend on the type of boundary conditions assumed in the BCF model at the steps. Due to the fact that the energy (2.24) is an approximation of the total energy of steps, one can state that the energy dissipation

$$\frac{\mathrm{d}}{\mathrm{d}t}\mathcal{E}(\phi) \le 0$$

one obtains for system (2.26)–(2.28) (see [OPR$^+$04]) displays the reduction of the total energy of the steps (2.23) one gets for the BCF model. Furthermore, one concludes that (2.28) is a parabolic equation if the anisotropy function γ is convex, which is assumed throughout this paper.

Mobility for TBC

Phase-field approximations of an isotropic BCF model with thermodynamic boundary conditions (2.17) have been proposed by Liu and Metiu [LM94] for the numerical investigation of one dimensional step trains, whereas Karma and Plapp used a similar model in order to study spiral growth [KP98], which will also be a topic in Section 2.3.5. Formal justification by matched asymptotic analysis has been provided in [RV04] and in [RV05] for the incorporation of an additional edge diffusion

term in the velocity law into a diffuse-interface model. An anisotropic phase-field model in a solidification application has been proposed in [MWB+93].

Here, we combine the approach in [RV05] for the isotropic case with the one in [RRV06], where a model for anisotropic surface diffusion has been treated. Defining

$$\tilde{\nu}(n(\nabla\phi)) := \frac{\nu(n(\nabla\phi))}{\rho^*\gamma(n(\nabla\phi))} \quad \text{and} \quad B(\phi) := 2G(\phi), \tag{2.29}$$

we use the mobility function

$$M_\varepsilon(\phi,\nabla\phi) := D + \varepsilon^{-1}\tilde{\nu}(n(\nabla\phi))B(\phi) = D + 2\varepsilon^{-1}\tilde{\nu}(n(\nabla\phi))G(\phi), \tag{2.30}$$

which is based on ideas in [CENC96], where a degenerate mobility has been used vanishing in the phases and being increased to $\mathcal{O}(\varepsilon^{-1})$ at the interface in order to obtain a diffuse-interface approximation of motion by surface diffusion. This corresponds to setting $D = 0$ in (2.30). A similar approach with a mobility being increased at the interface has been proposed by Fife and Penrose in order to incorporate a surface diffusion term into the formula for the normal velocity of a Mullins-Sekerka model ([FP95]). From (2.30) one obtains that for $\phi \in \mathbb{Z}$, i.e. on the terraces, one has $M_\varepsilon(\phi,\nabla\phi) = D$, whereas for $\phi \notin \mathbb{Z}$ the mobility M_ε is increased to $\mathcal{O}(\varepsilon^{-1})$ leading in the sharp-interface limit to an additional term in the velocity formula modelling the diffusion of atoms along step edges (see (2.22)).

Furthermore, for reasons explained in Section 2.2.1, the kinetic coefficient

$$\tilde{k}(n(\nabla\phi)) := \frac{k(n(\nabla\phi))}{\gamma(n(\nabla\phi))} \tag{2.31}$$

has to be introduced in order to obtain the desired asymptotics for $\varepsilon \to 0$.

Mobility for KBC

In order to provide a diffuse-interface approximation of a BCF model with kinetic boundary conditions (2.18), (2.19), we generalize the matched asymptotic analysis presented in [OPR+04] to the anisotropic situation, again using the approach presented in [RRV06]. The basic idea thereby, in turn, lies in the mobility function M_ε, which is now degenerate in a different sense compared to (2.30). A different approach for the approximation of a BCF model with kinetic boundary conditions has been proposed in [PL03].

The question is, how kinetic boundary conditions modelling the ES barrier can be incorporated into the diffuse-interface approximation. The ES barrier is a higher energy barrier that must be overcome by an adatom in order to attach to a step from the upper terrace, i.e. the attachment of an adatom to a step down is penalized compared to a step up (see Figure 2.5). This asymmetry in attachment of adatoms is modelled in the BCF system (2.15), (2.18), (2.19), (2.22) by the asymmetry in the boundary conditions. These yield a discontinuity in the adatom density at the steps, which requires a degenerate diffusion coefficient, and the idea is now to introduce

a variable mobility, which is $\mathcal{O}(\varepsilon)$ at the steps but constant on the terraces. This mobility is asymmetric in the sense that it is reduced for adatoms coming from the upper terrace to the step and kept constant for adatoms coming from the lower terrace to the step (see Figure 2.5).

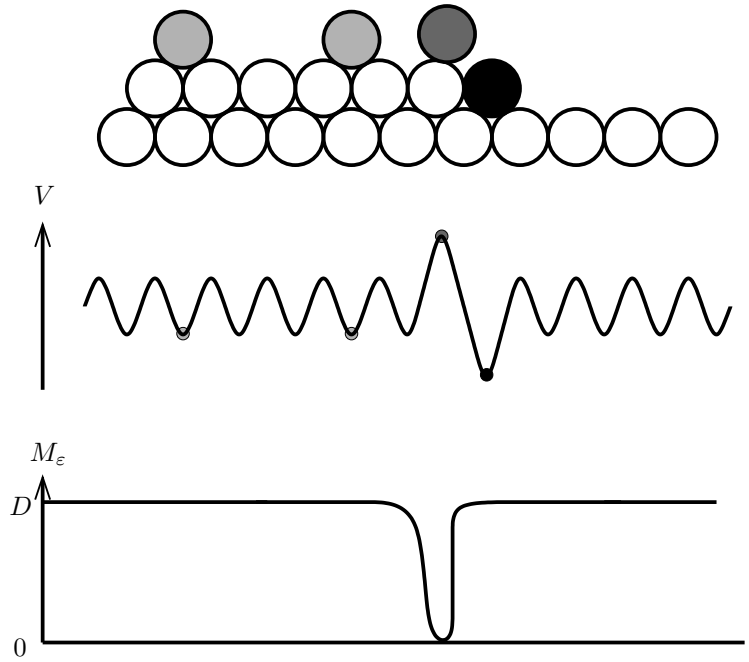

Figure 2.5: Idea of asymmetric mobility M_ε.

These ideas are now fixed by the concrete choice of the mobility function

$$M_\varepsilon(\phi, \nabla\phi) := \frac{D}{1 + \varepsilon^{-1} k_1^{-1}(n(\nabla\phi))\zeta(\phi)}, \tag{2.32}$$

where $k_1 := \gamma k_0 : \mathrm{S}^1 \to \mathbb{R}$ is an anisotropy function and $\zeta = \zeta(\phi)$ is periodic and asymmetric. Furthermore, we require ζ to vanish at all integer values of ϕ, i.e. on the different terraces (see Figure 2.6). This can be achieved by a choice $\zeta(\phi) \sim \phi^2(1-\phi)^2\phi^{p_\zeta}$ for $\phi \in [0,1]$ and periodically extended to all $\phi \in \mathbb{R}$ with $p_\zeta \in \mathbb{R}$, $p_\zeta > 0$ (see (2.95) in Section 2.2.2). Such a choice of the function ζ implies that the mobility is asymmetric and $M_\varepsilon = D$ on the terraces. Moreover, we see from (2.32) that

$$M_\varepsilon(\phi, \nabla\phi) = \varepsilon \frac{D k_1(n(\nabla\phi))}{\zeta(\phi)} + \mathcal{O}(\varepsilon^2) \quad \text{whenever} \quad \zeta(\phi) > 0, \tag{2.33}$$

if we expand M_ε in powers of ε. Finally, the asymmetric function ζ can be interpreted as an additional friction coefficient for the adatom movement. As the position of the steps can be given by the level sets, where ϕ attains half numbered values, the

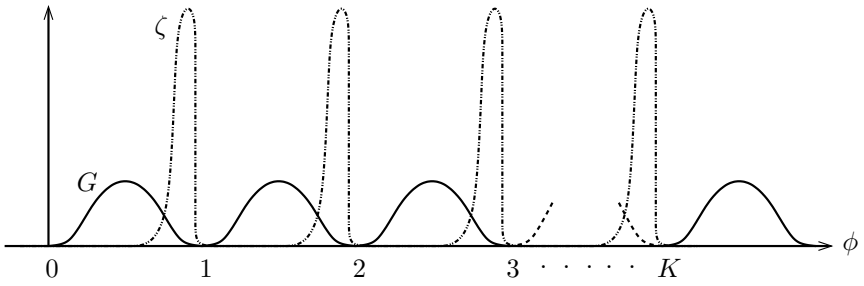

Figure 2.6: Multi well potential G, asymmetric friction ζ.

friction coefficient increases for an adatom coming from the upper terrace to the step (Figure 2.6).

Again, by the results of the asymptotic analysis in Section 2.2.2, one obtains that a choice $\tilde{k} \sim \frac{k_0}{\gamma}$ yields the desired asymptotics as $\varepsilon \to 0$. For the precise choice of ζ and $\tilde{k}$ we refer to (2.95), (2.99), (2.98) and (2.100) in Section 2.2.2. Furthermore, it should be mentioned that for the approximation of the BCF model with kinetic boundary conditions we have to restrict ourselves to a velocity law (2.22) with $\nu = 0$, i.e. we are not able to include the edge diffusion term modelling the diffusion of atoms along the step edges.

Derivative of Energy Density E

Here, we want to calculate the derivative of the energy density E_p needed in (2.28), where $E(z,\cdot) \in \mathrm{C}^1(\mathbb{R}^2)$, since the function $p \mapsto \gamma(-\frac{p}{|p|})$ belongs to $\mathrm{C}^1(\mathbb{R}^2 \setminus \{0\})$ and is bounded, and, therefore, $\gamma_0^2(p) := |p|^2\gamma^2(-\frac{p}{|p|}) \in \mathrm{C}^1(\mathbb{R}^2)$ holds with $\mathrm{D}_p\gamma_0^2(0) = 0$. Thus, for the given anisotropy function

$$\gamma : \mathrm{S}^1 \to \mathbb{R},$$

we consider an extension

$$\hat{\gamma} : \mathbb{R}^2 \setminus \{0\} \to \mathbb{R}, \quad \hat{\gamma}(p) := \gamma\left(-\frac{p}{|p|}\right).$$

Furthermore, we are interested in

$$h : I := [0, 2\pi) \to \mathrm{S}^1, \quad h = h(\theta) = (\cos(\theta), \sin(\theta)) \tag{2.34}$$

and in the angle $\theta := h^{-1} : \mathrm{S}^1 \to I$ of $n \in \mathrm{S}^1$ with the x-axis

$$\theta = \theta(n) = \begin{cases} \arctan(n_2/n_1) & \text{for } n_1 \geq 0,\ n_2 \geq 0, \\ \pi + \arctan(n_2/n_1) & \text{for } n_1 < 0, \\ 2\pi + \arctan(n_2/n_1) & \text{for } n_1 \geq 0,\ n_2 < 0. \end{cases} \tag{2.35}$$

This leads to the anisotropy function

$$\gamma \circ h : I \to \mathbb{R}.$$

Then, we have

$$\begin{aligned} \mathrm{D}_p\hat{\gamma}(p) &= (\gamma \circ h)'(\theta(-p/|p|))|p|^{-2}(-p_2, p_1) \\ &= \gamma'(-p/|p|)|p|^{-2}(-p_2, p_1). \end{aligned} \tag{2.36}$$

For the proof of (2.36), we write

$$n : \mathbb{R}^2 \setminus \{0\} \to \mathrm{S}^1, \quad n(p) := -\frac{p}{|p|}$$

and compute

$$\mathrm{D}_p\hat{\gamma} = \mathrm{D}_p(\gamma \circ h \circ h^{-1} \circ n) = \gamma' \mathrm{D}_p(h^{-1} \circ n),$$

where

$$\mathrm{D}_p(h^{-1} \circ n)(p) = \mathrm{D}_p \arctan(p_2/p_1) = |p|^{-2}(-p_2, p_1),$$

from which one gets (2.36). This yields for the Lagrange function E the derivative

$$\begin{aligned} \mathrm{D}_p E(z,p) &= \varepsilon \mathrm{D}_p \gamma_0^2(p) = \varepsilon \left\{ \hat{\gamma}^2(p)p + \hat{\gamma}(p)|p|^2 \mathrm{D}_p\hat{\gamma}(p) \right\} \\ &= \varepsilon \left\{ \gamma^2 \left(-\frac{p}{|p|} \right) p + \gamma \left(-\frac{p}{|p|} \right) \gamma' \left(-\frac{p}{|p|} \right) (-p_2, p_1) \right\} \end{aligned}$$

for $p \neq 0$ and $\mathrm{D}_p E(z, 0) = 0$ and, therefore,

$$E_p(\phi, \nabla\phi) = \varepsilon \left\{ \gamma^2(n(\nabla\phi))\nabla\phi + \gamma(n(\nabla\phi))\gamma'(n(\nabla\phi))(-\partial_{x_2}\phi, \partial_{x_1}\phi) \right\} \tag{2.37}$$

and $E_p(\phi, 0) = 0$. In (2.37), one can recognize a splitting of E_p into a normal and a tangential component.

Regularization of Mobility and Kinetic Coefficient

One difficulty that has not been addressed yet is due to the fact that the anisotropy functions $\tilde{\nu}$ and k_1 appearing in the mobility functions in the TBC and KBC case, respectively, as well as the kinetic coefficient $\tilde{k}$ are not defined for $p = \nabla\phi = 0$, unless they are constant, or, in other words, $\tilde{\nu} \circ n$, $k_1 \circ n$ and $\tilde{k} \circ n$ are only of class $\mathrm{C}^0(\mathbb{R}^2 \setminus \{0\})$ and discontinuous in $p = 0$. As a consequence, it is not clear how to define a weak formulation of the viscous Cahn-Hilliard equation (2.26)–(2.28) in the anisotropic situation. One can avoid this difficulty by introducing regularizations of the form $\tilde{\nu}_\varepsilon \circ n \in \mathrm{C}^0(\mathbb{R}^2)$ satisfying

$$\tilde{\nu}_\varepsilon(n(p)) = \tilde{\nu}(n(p)) \quad \text{for} \quad |p| > \alpha(\varepsilon)$$

with $\alpha(\varepsilon) = \mathcal{O}(\varepsilon)$ with corresponding regularizations for k_1 and $\tilde{k}$ (see [EPS96] for analytic results concerning the anisotropic Allen-Cahn equation).

2.2 Asymptotic Analysis

In this section, we want provide matched asymptotic expansions (see e.g. [Peg89]) for the approximation of the quasi-stationary BCF model with thermodynamic boundary conditions and of the quasi-stationary BCF model with kinetic boundary conditions by a viscous Cahn-Hilliard equation (2.26)–(2.28). In order to achieve more rigorous results, one would have to apply techniques from [ABC94].

2.2.1 Quasi-stationary BCF Model with Thermodynamic Boundary Conditions

Matched asymptotic expansions showing formal convergence towards a BCF model with thermodynamic boundary conditions have been provided in [RV04] and [RV05]. For the treatment by asymptotic analysis of anisotropic phase-field models in different applications, we refer to [MWB$^+$93, RRV06]. Here, both approaches are now combined.

New Coordinates

New coordinates are established in a neighbourhood of the curve Γ_i. To this end, $r = r(x_1, x_2, t; \varepsilon)$ is defined as the signed distance of (x_1, x_2) from $\Gamma_i(t; \varepsilon)$, where $r < 0$, if $(x_1, x_2) \in \Omega_i$ and $r > 0$ if $(x_1, x_2) \in \Omega_{i-1}$. Then for $0 < \rho_\varepsilon \ll 1$ there exists a neighbourhood

$$U_i(t; \varepsilon) = \{(x_1, x_2) \in \Omega : |r(x_1, x_2, t; \varepsilon)| < \rho_\varepsilon\}$$

of $\Gamma_i(t; \varepsilon)$ such that a orthogonal curvilinear coordinate system (r, s) in U_i can be defined, where for $(x_1, x_2) \in \Gamma_i(t; \varepsilon)$ one defines $s = s(x_1, x_2, t; \varepsilon)$ to be the arc length along $\Gamma_i(t; \varepsilon)$ to (x_1, x_2) from some point $(x_1, x_2) \in \Gamma_i(t; \varepsilon)$. The curve Γ_i then can be parametrized with respect to arc length by

$$X_i = X_i(s, t; \varepsilon) : I \subset \mathbb{R} \to \Gamma_i(t; \varepsilon), \quad I := [0, L(\Gamma_i)].$$

Now, one transforms w, j and ϕ to the new coordinate system:

$$\begin{aligned}
\hat{w}^i(r, s, t; \varepsilon) &:= w(X_i(s, t; \varepsilon) + rN_i(s, t; \varepsilon), t; \varepsilon), && (x_1, x_2) \in U_i(t; \varepsilon),\\
\hat{j}^i(r, s, t; \varepsilon) &:= j(X_i(s, t; \varepsilon) + rN_i(s, t; \varepsilon), t; \varepsilon), && (x_1, x_2) \in U_i(t; \varepsilon),\\
\hat{\phi}^i(r, s, t; \varepsilon) &:= \phi(X_i(s, t; \varepsilon) + rN_i(s, t; \varepsilon), t; \varepsilon), && (x_1, x_2) \in U_i(t; \varepsilon).
\end{aligned}$$

Furthermore, a stretched variable is introduced by $z := \frac{r}{\varepsilon}$, and one defines

$$\begin{aligned}
W^i(z, s, t; \varepsilon) &:= \hat{w}^i(r, s, t; \varepsilon),\\
J^i(z, s, t; \varepsilon) &:= \hat{j}^i(r, s, t; \varepsilon),\\
\Phi^i(z, s, t; \varepsilon) &:= \hat{\phi}^i(r, s, t; \varepsilon).
\end{aligned}$$

In addition, the following Taylor expansion approximations for small ε are assumed to be valid:

$$w(x_1, x_2, t; \varepsilon) = w_0(x_1, x_2, t) + \mathcal{O}(\varepsilon), \tag{2.38}$$

$$\hat{w}^i(r, s, t; \varepsilon) = \hat{w}_0^i(r, s, t) + \mathcal{O}(\varepsilon), \tag{2.39}$$

$$W^i(z, s, t; \varepsilon) = W_0^i(z, s, t) + \mathcal{O}(\varepsilon), \tag{2.40}$$

$$j(x_1, x_2, t; \varepsilon) = j_0(x_1, x_2, t) + \mathcal{O}(\varepsilon), \tag{2.41}$$

$$\hat{j}^i(r, s, t; \varepsilon) = \hat{j}_0^i(r, s, t) + \mathcal{O}(\varepsilon), \tag{2.42}$$

$$J^i(z, s, t; \varepsilon) = \varepsilon^{-2} J_{-2}^i(z, s, t) + \varepsilon^{-1} J_{-1}^i(z, s, t) + J_0^i(z, s, t) + \mathcal{O}(\varepsilon), \tag{2.43}$$

$$\phi(x_1, x_2, t; \varepsilon) = \phi_0(x_1, x_2, t) + \mathcal{O}(\varepsilon), \tag{2.44}$$

$$\hat{\phi}^i(r, s, t; \varepsilon) = \hat{\phi}_0^i(r, s, t) + \mathcal{O}(\varepsilon), \tag{2.45}$$

$$\Phi^i(z, s, t; \varepsilon) = \Phi_0^i(z, s, t) + \varepsilon \Phi_1^i(z, s, t) + \mathcal{O}(\varepsilon^2). \tag{2.46}$$

Thereby, (2.38), (2.39), (2.41), (2.42), (2.44) and (2.45) are called outer expansions while (2.40), (2.43) and (2.46) are called inner expansions. It is assumed that these hold simultaneously in some overlapping region and represent the same functions, which yields the matching conditions

$$\lim_{r \to \pm 0} \hat{w}_0^i(r, s, t) = \lim_{z \to \pm\infty} W_0^i(z, s, t), \tag{2.47}$$

$$\lim_{r \to \pm 0} \hat{j}_0^i(r, s, t) = \lim_{z \to \pm\infty} J_0^i(z, s, t), \tag{2.48}$$

$$\lim_{r \to \pm 0} \hat{\phi}_0^i(r, s, t) = \lim_{z \to \pm\infty} \Phi_0^i(z, s, t). \tag{2.49}$$

Let $T_i = T_i(s, t; \varepsilon) := \partial_s X_i(s, t; \varepsilon)$, $N_i = N_i(s, t; \varepsilon)$, $v_i = v_i(s, t; \varepsilon) := \partial_t X_i(s, t; \varepsilon) \cdot N_i(s, t; \varepsilon)$ and $\kappa_i = \kappa_i(s, t; \varepsilon)$ denote the tangent, the normal, the normal velocity and the curvature, where the normal is pointing from the subset of $U_i(t; \varepsilon)$ where $\phi > i - 1/2$ to the subset of $U_i(t; \varepsilon)$ where $\phi < i - 1/2$, i.e. from the upper to the lower terrace. Due to the Frenet formulas (note that the sign is different from the usual notation, where the normal points into the opposite direction)

$$\partial_s T_i = -\kappa_i N_i, \quad \partial_s N_i = \kappa_i T_i,$$

one can transform the derivatives into the new coordinates (r, s) as follows:

$$\partial_s \hat{\phi}^i = \nabla\phi \cdot (\partial_s X_i + r \partial_s N_i) = \nabla\phi \cdot (\partial_s X_i + r\kappa_i \partial_s X_i) = (1 + r\kappa_i) \nabla\phi \cdot T_i,$$

which yields

$$\nabla\phi \cdot T_i = (1 + r\kappa_i)^{-1} \partial_s \hat{\phi}^i. \tag{2.50}$$

Moreover, we get

$$\partial_r \hat{\phi}^i = \nabla\phi \cdot N_i \tag{2.51}$$

as well as

$$\partial_t \hat{\phi}^i = \partial_t \phi + \nabla\phi \cdot (\partial_t X_i + r\partial_t N_i),$$

in which one plugs in (2.50) and (2.51) in order to obtain

$$\begin{aligned}
\partial_t \phi &= \partial_t \hat{\phi}^i - \nabla\phi \cdot \{(\partial_t X_i \cdot N_i)N_i + (\partial_t X_i \cdot T_i)T_i + r\partial_t N_i\} \\
&= \partial_t \hat{\phi}^i - \nabla\phi \cdot \{v_i N_i + (\partial_t X_i \cdot T_i)T_i + r\partial_t N_i\} \\
&= \partial_t \hat{\phi}^i - v_i \partial_r \hat{\phi}^i - \nabla\phi \cdot \{(\partial_t X_i \cdot T_i)T_i + r\partial_t N_i\} \\
&= \partial_t \hat{\phi}^i - v_i \partial_r \hat{\phi}^i - (1 + r\kappa_i)^{-1} \partial_s \hat{\phi}^i (\partial_t X_i + r\partial_t N_i) \cdot T_i. \qquad (2.52)
\end{aligned}$$

By (2.50) and (2.51), one can express the gradient of ϕ as follows

$$\nabla\phi = (\nabla\phi \cdot T_i)T_i + (\nabla\phi \cdot N_i)N_i = \partial_r \hat{\phi}^i \; N_i + (1 + r\kappa_i)^{-1} \partial_s \hat{\phi}^i \; T_i. \qquad (2.53)$$

From this, one computes the divergence of a vector field j in terms of the transformed one $\hat{j}^i$

$$\begin{aligned}
\nabla \cdot j &= \partial_r \hat{j}^i \cdot N_i + (1 + r\kappa_i)^{-1} \partial_s \hat{j}^i \cdot T_i \\
&= \partial_r (\hat{j}^i \cdot N_i) + (1 + r\kappa_i)^{-1} (\partial_s (\hat{j}^i \cdot T_i) - \hat{j}^i \cdot \partial_s T_i) \\
&= \partial_r (\hat{j}^i \cdot N_i) + (1 + r\kappa_i)^{-1} (\partial_s (\hat{j}^i \cdot T_i) + \kappa_i \hat{j}^i \cdot N_i). \qquad (2.54)
\end{aligned}$$

Thus, (2.52), (2.53) and (2.54) read in the (z, s)-coordinate system

$$\partial_t \phi = -\varepsilon^{-1} v_i \partial_z \Phi^i + \partial_t \Phi^i - (1 + \varepsilon z \kappa_i)^{-1} \partial_s \Phi^i (\partial_t X_i + \varepsilon z \partial_t N_i) \cdot T_i, \qquad (2.55)$$

$$\nabla\phi = \varepsilon^{-1} \partial_z \Phi^i \; N_i + (1 + \varepsilon z \kappa_i)^{-1} \partial_s \Phi^i \; T_i, \qquad (2.56)$$

$$\nabla \cdot j = \varepsilon^{-1} \partial_z (J^i \cdot N_i) + (1 + \varepsilon z \kappa_i)^{-1} (\partial_s (J^i \cdot T_i) + \kappa_i J^i \cdot N_i). \qquad (2.57)$$

As consequence of (2.56), one has

$$|\nabla\phi| = \varepsilon^{-1} \left\{ |\partial_z \Phi^i|^2 + \left(\varepsilon (1 + \varepsilon z \kappa_i)^{-1} \partial_s \Phi^i \right)^2 \right\}^{1/2}. \qquad (2.58)$$

For later purposes in the inner expansion, we need

Lemma 1. *For sufficiently smooth $\gamma : \mathrm{S}^1 \to \mathbb{R}$, one has*

$$\partial_s \gamma(N_i) = \gamma'(N_i)\kappa_i \quad \textit{and} \quad \partial_s \gamma'(N_i) = \gamma''(N_i)\kappa_i. \qquad (2.59)$$

Proof. First, we drop the index i, and with $N = (N_1, N_2)$ we write, with h defined in (2.34),

$$\partial_s(\gamma(N)) = \partial_s(\gamma \circ h \circ h^{-1} \circ N) = \gamma'(N) \partial_s (h^{-1} \circ N),$$

where $T = (-N_2, N_1)$ and the Frenet formula

$$\partial_s N = \kappa T$$

yield

$$\begin{aligned}\partial_s(h^{-1}\circ N) &= \frac{1}{1+N_2^2/N_1^2}\frac{\partial_s N_2 N_1 - N_2\partial_s N_1}{N_1^2}\\ &= \partial_s N_2 N_1 - N_2\partial_s N_1 = \partial_s N\cdot T = \kappa T\cdot T = \kappa,\end{aligned}$$

which completes the proof. □

Outer Expansion

By inserting the outer expansion (2.45) into (2.28), one obtains

$$G'(\phi_0) = 0 \quad \Rightarrow \quad \phi_0 \in \mathbb{Z} \tag{2.60}$$

and

$$\lim_{r\to+0}\hat{\phi}_0^i = i-1, \qquad \lim_{r\to-0}\hat{\phi}_0^i = i,$$

which, by matching condition (2.49), yields

$$\lim_{z\to+\infty}\Phi_0^i = i-1, \qquad \lim_{z\to-\infty}\Phi_0^i = i. \tag{2.61}$$

Now, we insert the outer expansions (2.38) and (2.41) into (2.26) and (2.27), which yields

$$\nabla\cdot j_0 = F - \tau^{-1}w_0, \tag{2.62}$$

$$j_0 = -D\nabla w_0 \tag{2.63}$$

corresponding to (2.15) and (2.16) in the BCF model.

Inner Expansion

The main difficulty in the inner expansion of (2.28) is the inner expansion of the term $\nabla\cdot E_p(\phi,\nabla\phi)$, which is denoted by $C := \nabla\cdot E_p(\phi,\nabla\phi)$. Then, by introducing

$$n = n(z,s,t;\varepsilon) := -\frac{\nabla\phi}{|\nabla\phi|}$$

and by using

$$(-\partial_{x_2}\phi, \partial_{x_1}\phi) = \varepsilon^{-1}\partial_z\Phi^i T_i - (1+\varepsilon z\kappa_i)^{-1}\partial_s\Phi^i N_i,$$

(2.56) as well as (2.37), one obtains

$$\begin{aligned}C &= \nabla\cdot\varepsilon\left\{\gamma^2(n)\nabla\phi + \gamma(n)\gamma'(n)(-\partial_{x_2}\phi,\partial_{x_1}\phi)\right\}\\ &= \partial_z\left\{\gamma^2(n)\varepsilon^{-1}\partial_z\Phi^i - \gamma(n)\gamma'(n)(1+\varepsilon z\kappa_i)^{-1}\partial_s\Phi^i\right\}\\ &\quad + \varepsilon(1+\varepsilon z\kappa_i)^{-1}\kappa_i\left\{\gamma^2(n)\varepsilon^{-1}\partial_z\Phi^i - \gamma(n)\gamma'(n)(1+\varepsilon z\kappa_i)^{-1}\partial_s\Phi^i\right\}\\ &\quad + \varepsilon(1+\varepsilon z\kappa_i)^{-1}\partial_s\left\{\gamma^2(n)(1+\varepsilon z\kappa_i)^{-1}\partial_s\Phi^i + \gamma(n)\gamma'(n)\varepsilon^{-1}\partial_z\Phi^i\right\}.\end{aligned}$$

Then, we introduce the formal expansions

$$C = \varepsilon^{-1}C_{-1} + C_0 + \mathcal{O}(\varepsilon) \quad \text{and} \quad n = n_0 + \varepsilon n_1 + \mathcal{O}(\varepsilon^2)$$

and obtain in highest order

$$C_{-1} = \partial_z(\gamma^2(n_0)\partial_z\Phi_0^i). \tag{2.64}$$

Inserting the inner expansion (2.46) into (2.28) yields for $\mathcal{O}(\varepsilon^{-1})$ in (2.28)

$$\partial_z(\gamma^2(n_0)\partial_z\Phi_0^i) - G'(\Phi_0^i) = 0.$$

From this and (2.61), one easily gets $\partial_z\Phi_0^i < 0$. Now, we use (2.58), expand

$$n = -\frac{\nabla\phi}{|\nabla\phi|} = -\frac{\partial_z\Phi^i N_i + \varepsilon(1+\varepsilon z\kappa_i)^{-1}\partial_s\Phi^i T_i}{[\ (\partial_z\Phi^i)^2 + (\varepsilon(1+\varepsilon z\kappa_i)^{-1}\partial_s\Phi^i)^2]^{1/2}}$$

and, thus, obtain

$$n_0 = -\frac{\partial_z\Phi_0^i N_i}{|\partial_z\Phi_0^i|} = N_i \tag{2.65}$$

as well as

$$\begin{aligned} n_1 = \frac{\mathrm{d}}{\mathrm{d}\varepsilon}n\big|_{\varepsilon=0} &= -\frac{\partial_z\Phi_1^i N_i + \partial_s\Phi_0^i T_i}{|\partial_z\Phi_0^i|} + \frac{\partial_z\Phi_0^i 2\partial_z\Phi_0^i\partial_z\Phi_1^i N_i}{2|\partial_z\Phi_0^i|^3} \\ &= -\frac{\partial_s\Phi_0^i}{|\partial_z\Phi_0^i|}T_i = \frac{\partial_s\Phi_0^i}{\partial_z\Phi_0^i}T_i. \end{aligned} \tag{2.66}$$

Using (2.65) and (2.66) and additionally taking (2.36) into account, one ends up with

$$\gamma(n)\big|_{\varepsilon=0} = \gamma(n_0) = \gamma(N_i), \tag{2.67}$$

$$\frac{\mathrm{d}}{\mathrm{d}\varepsilon}\left(\gamma(n)\right)\big|_{\varepsilon=0} = \gamma'(N_i)n_1\cdot T_i = \gamma'(N_i)\frac{\partial_s\Phi_0^i}{\partial_z\Phi_0^i}. \tag{2.68}$$

Finally, by (2.67) and (2.68), we arrive at

$$\begin{aligned} C_0 = \frac{\mathrm{d}}{\mathrm{d}\varepsilon}C\big|_{\varepsilon=0} &= \partial_z\left(\gamma^2\partial_z\Phi_1^i + 2\gamma\gamma'\partial_s\Phi_0^i - \gamma\gamma'\partial_z\partial_s\Phi_0^i\right) \\ &\quad + \kappa_i\gamma^2\partial_z\Phi_0^i + \partial_s(\gamma\gamma'\partial_z\Phi_0^i) \\ &= \gamma^2\partial_z^2\Phi_1^i + 2\gamma\gamma'\partial_s\partial_z\Phi_0^i + \kappa_i\gamma^2\partial_z\Phi_0^i + \left((\gamma')^2 + \gamma\gamma''\right)\kappa_i\partial_z\Phi_0^i, \end{aligned} \tag{2.69}$$

where we have used (2.59) in Lemma 1. Because of (2.64) and (2.65) one obtains

$$\gamma^2\partial_z^2\Phi_0^i - G'(\Phi_0^i) = 0. \tag{2.70}$$

Here, we want to remark that in contrast to isotropic situations the solution Φ_0^i of (2.70) depends on the arc length s. By multiplying (2.70) by $\partial_z \Phi_0^i$ and integrating along the z-axis

$$\gamma^2 (\partial_z \Phi_0^i)^2 = 2G(\Phi_0^i),$$

which yields

$$\partial_z \Phi_0^i = -\frac{\sqrt{2G(\Phi_0^i)}}{\gamma} \tag{2.71}$$

leading to

$$\int_{-\infty}^{+\infty} (\partial_z \Phi_0^i)^2 \,\mathrm{d}z = \frac{1}{\gamma} \int_{i-1}^{i} \sqrt{2G(\phi)}\,\mathrm{d}\phi = \frac{1}{\gamma}, \tag{2.72}$$

by the concrete choice of $G = G(\phi)$ (see (2.25)). This will be used for the inner expansions in (2.26) and (2.27). The transformation rules (2.55)–(2.57) thereby yield for (2.26)

$$\begin{aligned} &-\varepsilon^{-1} v_i \partial_z \Phi^i + \partial_t \Phi^i - (1+\varepsilon z \kappa_i)^{-1} \partial_s \Phi^i (\partial_t X_i + \varepsilon z \partial_t N_i) \cdot T_i \\ &+ \varepsilon^{-1} \partial_z (J^i \cdot N_i) + (1+\varepsilon z \kappa_i)^{-1} (\partial_s (J^i \cdot T_i) + \kappa_i J^i \cdot N_i) \\ &\quad = F - \tau^{-1} W^i \end{aligned} \tag{2.73}$$

and for (2.27)

$$\begin{aligned} J^i &= -(\varepsilon^{-1} \tilde{\nu}(n) B(\Phi^i) + D)(\varepsilon^{-1} \partial_z W^i N_i + (1+\varepsilon z \kappa_i)^{-1} \partial_s W^i T_i) \\ &= -\varepsilon^{-2} \tilde{\nu}(n) B(\Phi^i) \partial_z W^i N_i - \varepsilon^{-1} \tilde{\nu}(n) B(\Phi^i)(1+\varepsilon z \kappa_i)^{-1} \partial_s W^i T_i \\ &\quad - \varepsilon^{-1} D \partial_z W^i N_i - D(1+\varepsilon z \kappa_i)^{-1} \partial_s W^i T_i. \end{aligned} \tag{2.74}$$

Then, we get to $\mathcal{O}(\varepsilon^{-3})$ in (2.73)

$$\partial_z (J_{-2}^i \cdot N_i) = 0.$$

From this, one gets to $\mathcal{O}(\varepsilon^{-2})$ in (2.74)

$$\text{const} = J_{-2}^i \cdot N_i = -\tilde{\nu}(N_i) B(\Phi_0^i) \partial_z W_0^i$$

the constant being zero because of $\lim_{|z|\to\infty} B(\Phi_0^i) = 0$. So, one finally arrives at

$$J_{-2}^i \cdot N_i = 0 \tag{2.75}$$

and

$$\partial_z W_0^i = 0 \quad \Rightarrow \quad W_0^i \equiv W_0^i(s,t). \tag{2.76}$$

Using (2.75), (2.76) and

$$J_{-2}^i \cdot T_i = 0,$$

one obtains to $\mathcal{O}(\varepsilon^{-2})$ in (2.73)

$$\partial_z(J^i_{-1}\cdot N_i)=0.$$

As before, this yields to $\mathcal{O}(\varepsilon^{-1})$ in (2.74)

$$J^i_{-1}\cdot N_i=0. \tag{2.77}$$

Finally, one makes use of (2.75) and (2.77) to obtain to $\mathcal{O}(\varepsilon^{-1})$ in (2.73)

$$-v_i\partial_z\Phi^i_0+\partial_z(J^i_0\cdot N_i)+\partial_s(J^i_{-1}\cdot T_i)=0, \tag{2.78}$$

where we have to $\mathcal{O}(\varepsilon^{-1})$ in (2.74)

$$J^i_{-1}\cdot T_i=-\tilde{\nu}(N_i)B(\Phi^i_0)\partial_s W^i_0.$$

Integrating (2.78) along the z-axis, one obtains

$$v_i=\lim_{z\to-\infty}J^i_0\cdot N_i-\lim_{z\to+\infty}J^i_0\cdot N_i+\partial_s\left(\tilde{\nu}\int_{-\infty}^{+\infty}B(\Phi^i_0)\,\mathrm{d}z\partial_s W^i_0\right),$$

where

$$\int_{-\infty}^{+\infty}B(\Phi^i_0)\,\mathrm{d}z=\int_{-\infty}^{+\infty}2G(\Phi^i_0)\,\mathrm{d}z=\gamma^2\int_{-\infty}^{+\infty}(\partial_z\Phi^i_0)^2\,\mathrm{d}z=\gamma.$$

So, using matching condition (2.48) and the definition (2.29) of $\tilde{\nu}$, one ends up with

$$v_i=\lim_{r\to-0}\hat{j}^i_0\cdot N_i-\lim_{r\to+0}\hat{j}^i_0\cdot N_i+\partial_s((\rho^*)^{-1}\nu\partial_s W^i_0), \tag{2.79}$$

where

$$\lim_{r\to\pm0}\hat{j}^i_0\cdot N_i=-\lim_{r\to\pm0}D\nabla\hat{w}_0\cdot N_i. \tag{2.80}$$

Now, we consider $\mathcal{O}(\varepsilon^0)$ in (2.28)

$$-\tilde{k}^{-1}(N_i)v_i\partial_z\Phi^i_0=\mu_0\left(C_0-G''(\Phi^i_0)\Phi^i_1\right)+W^i_0$$

with C_0 given by (2.69). Testing this equation with $\partial_z\Phi^i_0$, one gets

$$\begin{aligned}-\tilde{k}^{-1}v_i\int_{-\infty}^{+\infty}(\partial_z\Phi^i_0)^2\,\mathrm{d}z=\mu_0\gamma^2\int_{-\infty}^{+\infty}\partial_z^2\Phi^i_1\partial_z\Phi^i_0\,\mathrm{d}z+\mu_0\gamma\gamma'\partial_s\int_{-\infty}^{+\infty}(\partial_z\Phi^i_0)^2\,\mathrm{d}z\\+\mu_0\gamma^2\kappa_i\int_{-\infty}^{+\infty}(\partial_z\Phi^i_0)^2\,\mathrm{d}z\\+\mu_0\left((\gamma')^2+\gamma\gamma''\right)\kappa_i\int_{-\infty}^{+\infty}(\partial_z\Phi^i_0)^2\,\mathrm{d}z\\-\mu_0\int_{-\infty}^{+\infty}G''(\Phi^i_0)\Phi^i_1\partial_z\Phi^i_0\,\mathrm{d}z+W^i_0\int_{-\infty}^{+\infty}\partial_z\Phi^i_0\,\mathrm{d}z\end{aligned}$$

First, we use integration by parts in order to obtain

$$\begin{aligned}\gamma^2 \int_{-\infty}^{+\infty} \partial_z^2 \Phi_1^i \partial_z \Phi_0^i \,\mathrm{d}z - \int_{-\infty}^{+\infty} G''(\Phi_0^i)\Phi_1^i \partial_z \Phi_0^i \,\mathrm{d}z \\ = \gamma^2 \int_{-\infty}^{+\infty} \Phi_1^i \partial_z^3 \Phi_0^i \,\mathrm{d}z - \int_{-\infty}^{+\infty} \partial_z (G'(\Phi_0^i))\Phi_1^i \,\mathrm{d}z \\ = \int_{-\infty}^{+\infty} \Phi_1^i \partial_z (\gamma^2 \partial_z^2 \Phi_0^i - G'(\Phi_0^i)) \,\mathrm{d}z = 0.\end{aligned}$$

Using (2.72), we then arrive at

$$-\frac{\tilde{k}^{-1} v_i}{\gamma} = \mu_0 \left(\gamma\gamma' \partial_s \frac{1}{\gamma} + \gamma\kappa_i + \left((\gamma')^2 + \gamma\gamma''\right) \frac{\kappa_i}{\gamma} \right) - W_0^i$$

and, by (2.59) and the definition (2.31) of $\tilde{k}$, finally get

$$\begin{aligned} W_0^i &= \frac{\tilde{k}^{-1} v_i}{\gamma} + \mu_0 \left(-\frac{(\gamma')^2}{\gamma}\kappa_i + \gamma\kappa_i + \frac{(\gamma')^2}{\gamma}\kappa_i + \gamma''\kappa_i \right) \\ &= k^{-1} v_i + \mu_0(\gamma + \gamma'')\kappa_i = k^{-1} v_i + \mu_0 \tilde{\gamma} \kappa_i. \end{aligned} \tag{2.81}$$

Thus, by matching condition (2.47) and by (2.21), one arrives at the equilibrium condition

$$\lim_{r \to \pm 0} w_0 = k^{-1} v_i + \mu_0 \tilde{\gamma} \kappa_i = k^{-1} v_i + \mu \kappa_i$$

as desired in (2.17). Furthermore, by inserting (2.81) into (2.79), one arrives at

$$v_i = \left(\lim_{r \to -0} \hat{j}_0^i - \lim_{r \to +0} \hat{j}_0^i \right) \cdot N_i + \partial_s((\rho^*)^{-1} \nu \partial_s (k^{-1} v_i + \mu \kappa_i)),$$

and, due to the convention that $r > 0$ holds on the lower terrace and $r < 0$ on the upper terrace and (2.80), we have obtained the velocity law (2.22) to leading order.

2.2.2 Quasi-stationary BCF Model with Kinetic Boundary Conditions

For the approximation of the BCF model with kinetic boundary conditions (2.18), (2.19), we have to restrict ourselves to a velocity law without additional edge diffusion term, i.e. in (2.22) one has to set $\nu = 0$. For the asymptotic analysis in this case, we follow the approach described in [OPR$^+$04] and adjust it to the anisotropic situation using the framework in [RRV06]. Thereby, we assume the expansions (2.38)–(2.46) with (2.43) replaced by

$$J^i(z, s, t; \varepsilon) = J_0^i(z, s, t) + \mathcal{O}(\varepsilon). \tag{2.82}$$

Outer Expansion

The outer expansion of (2.28) of the TBC case remains valid in this situation. Because of this, one obtains, by the definition of the mobility function (2.32) and from (2.60), the relation

$$M_\varepsilon(\phi_0) = D$$

and, therefore, the same stationary diffusion equation (2.62), (2.63) as in the TBC case.

Inner Expansion

As in the TBC case, we obtain from (2.28) the expressions (2.70), (2.71) and (2.72). Again, by the transformation rules (2.55)–(2.57) inserted in (2.26), one ends up with

$$\begin{aligned} &-\varepsilon^{-1}v_i\partial_z\Phi^i + \partial_t\Phi^i - (1+\varepsilon z\kappa_i)^{-1}\partial_s\Phi^i(\partial_t X_i + \varepsilon z\partial_t N_i)\cdot T_i \\ &+\varepsilon^{-1}\partial_z(J^i\cdot N_i) + (1+\varepsilon z\kappa_i)^{-1}(\partial_s(J^i\cdot T_i) + \kappa_i J^i\cdot N_i) \\ &\quad = F - \tau^{-1}W^i \end{aligned} \tag{2.83}$$

and in (2.27)

$$J^i = -\frac{D}{1+\varepsilon^{-1}k_1^{-1}(n)\zeta(\Phi^i)}(\varepsilon^{-1}\partial_z W^i N_i + (1+\varepsilon z\kappa_i)^{-1}\partial_s W^i T_i). \tag{2.84}$$

From this, one gets to $\mathcal{O}(\varepsilon^{-1})$ in (2.83)

$$-v_i\partial_z\Phi_0^i + \partial_z(J_0^i\cdot N_i) = 0. \tag{2.85}$$

Integration of this equation and matching conditions (2.48) and (2.49) yield

$$v_i = \lim_{z\to-\infty} J_0^i\cdot N_i - \lim_{z\to+\infty} J_0^i N_i = \lim_{r\to-0}\hat{j}_0^i\cdot N_i - \lim_{r\to+0}\hat{j}_0^i\cdot N_i,$$

where

$$\lim_{r\to\pm0}\hat{j}_0^i\cdot N_i = -\lim_{r\to\pm0} D\nabla\hat{w}_0\cdot N_i$$

yields the desired velocity law (2.22) with $\nu = 0$. Besides, one obtains from (2.85) that there exists a function $\lambda_i = \lambda_i(s,t)$ independent of z such that

$$-v_i\Phi_0^i + \lambda_i = -J_0^i\cdot N_i, \tag{2.86}$$

which yields in the limit $z\to-\infty$

$$\lambda_i = -\lim_{r\to-0}\hat{j}_0^i\cdot N_i + iv_i, \tag{2.87}$$

and for $z\to+\infty$ one gets

$$\lambda_i = -\lim_{r\to+0}\hat{j}_0^i\cdot N_i + (i-1)v_i. \tag{2.88}$$

Now, we consider the terms of order $\mathcal{O}(\varepsilon^0)$ in (2.84) and keep (2.33) in mind and obtain

$$J_0^i = -\frac{Dk_1(N_i)}{\zeta(\Phi_0^i)}\partial_z W_0^i N_i, \tag{2.89}$$

which together with (2.86) and (2.87) yields

$$\partial_z W_0^i = \frac{\zeta(\Phi_0^i)}{Dk_1(N_i)}(\lambda_i - v_i\Phi_0^i) = \frac{\zeta(\Phi_0^i)}{Dk_1(N_i)}\left(-\lim_{r\to -0}\hat{j}_0^i\cdot N_i + v_i(i-\Phi_0^i)\right). \tag{2.90}$$

Similarly, (2.89), (2.86) and (2.88) lead to

$$\partial_z W_0^i = \frac{\zeta(\Phi_0^i)}{Dk_1(N_i)}\left(-\lim_{r\to +0}\hat{j}_0^i\cdot N_i + v_i(i-1-\Phi_0^i)\right). \tag{2.91}$$

As in the TBC case, we get to $\mathcal{O}(\varepsilon^0)$ in (2.28)

$$-\tilde{k}^{-1}(N_i)v_i\partial_z\Phi_0^i = C_0 - G''(\Phi_0^i)\Phi_1^i + W_0^i.$$

The only difference is that W_0^i does not have to be constant in z. Again, we test the above equation with $\partial_z\Phi_0^i$. Thus, by using (2.91) we compute

$$\begin{aligned}
\int_{-\infty}^{+\infty} W_0^i\partial_z\Phi_0^i\,\mathrm{d}z &= \int_{-\infty}^{+\infty} W_0^i\partial_z(\Phi_0^i - i)\,\mathrm{d}z\\
&= -\lim_{z\to+\infty} W_0^i - \int_{-\infty}^{+\infty}\partial_z W_0^i(\Phi_0^i - i)\,\mathrm{d}z\\
&= -\lim_{z\to+\infty} W_0^i + \int_{-\infty}^{+\infty}\frac{\zeta(\Phi_0^i)}{Dk_1}\lim_{r\to+0}\hat{j}_0^i\cdot N_i(\Phi_0^i - i)\,\mathrm{d}z\\
&\quad + \int_{-\infty}^{+\infty}\frac{\zeta(\Phi_0^i)}{Dk_1}v_i(\Phi_0^i - (i-1))(\Phi_0^i - i)\,\mathrm{d}z\\
&= -\lim_{r\to+0}\hat{w}_0^i + \frac{\lim_{r\to+0}\hat{j}_0^i\cdot N_i}{Dk_1}\int_{-\infty}^{+\infty}\zeta(\Phi_0^i)(\Phi_0^i - i)\,\mathrm{d}z\\
&\quad + \frac{v_i}{Dk_1}\int_{-\infty}^{+\infty}\zeta(\Phi_0^i)(\Phi_0^i - (i-1))(\Phi_0^i - i)\,\mathrm{d}z\\
&= -\lim_{r\to+0}\hat{w}_0^i - \gamma\frac{\lim_{r\to+0}\hat{j}_0^i\cdot N_i}{Dk_1}\int_0^1\frac{\zeta(\phi)}{\sqrt{2G(\phi)}}(1-\phi)\,\mathrm{d}\phi\\
&\quad - \gamma\frac{v_i}{Dk_1}\int_0^1\frac{\zeta(\phi)}{\sqrt{2G(\phi)}}\phi(1-\phi)\,\mathrm{d}\phi.
\end{aligned}$$

As in the TBC case, we use (2.70) and (2.72) in order to obtain

$$-\int_{-\infty}^{+\infty} W_0^i\partial_z\Phi_0^i\,\mathrm{d}z = \frac{v_i}{\tilde{k}\gamma} + \mu_0(\gamma+\gamma'')\kappa_i$$

and, finally, the boundary condition

$$\lim_{r\to+0}\hat{w}_0^i-\mu_0(\gamma+\gamma'')\kappa_i=-\lim_{r\to+0}\hat{j}_0^i\cdot N_i\frac{\gamma}{Dk_1}\int_0^1\frac{\zeta(\phi)}{\sqrt{2G(\phi)}}(1-\phi)\,\mathrm{d}\phi + \frac{v_i}{\tilde{k}\gamma}-\frac{\gamma v_i}{Dk_1}\int_0^1\frac{\zeta(\phi)}{\sqrt{2G(\phi)}}\phi(1-\phi)\,\mathrm{d}\phi.$$

If one chooses the friction function ζ and k_1 such that

$$\frac{\gamma}{Dk_1}\int_0^1\frac{\zeta(\phi)}{\sqrt{2G(\phi)}}(1-\phi)\,\mathrm{d}\phi=\frac{1}{k_+}=\frac{1}{a_+k_0} \tag{2.92}$$

as well as $\tilde{k}$ such that

$$\frac{1}{\tilde{k}\gamma}=\frac{\gamma}{Dk_1}\int_0^1\frac{\zeta(\phi)}{\sqrt{2G(\phi)}}\phi(1-\phi)\,\mathrm{d}\phi, \tag{2.93}$$

one arrives at

$$k_+\left(\lim_{r\to+0}\hat{w}_0^i-\mu\kappa_i\right)=-\lim_{r\to+0}\hat{j}_0^i\cdot N_i,$$

which is the desired boundary condition (2.19) for attachment from the lower terrace.

To obtain the appropriate boundary condition for attachment to a step down, we use (2.90) and similarly compute

$$\begin{aligned}
\int_{-\infty}^{+\infty}W_0^i\partial_z\Phi_0^i\,\mathrm{d}z&=\int_{-\infty}^{+\infty}W_0^i\partial_z(\Phi_0^i-(i-1))\,\mathrm{d}z\\
&=-\lim_{z\to-\infty}W_0^i-\int_{-\infty}^{+\infty}\partial_zW_0^i(\Phi_0^i-(i-1))\,\mathrm{d}z\\
&=-\lim_{z\to-\infty}W_0^i+\int_{-\infty}^{+\infty}\frac{\zeta(\Phi_0^i)}{Dk_1}\lim_{r\to-0}\hat{j}_0^i\cdot N_i(\Phi_0^i-(i-1))\,\mathrm{d}z\\
&\quad-\int_{-\infty}^{+\infty}\frac{\zeta(\Phi_0^i)}{Dk_1}v_i(i-\Phi_0^i)(\Phi_0^i-(i-1))\,\mathrm{d}z\\
&=-\lim_{r\to-0}\hat{w}_0^i+\frac{\lim_{r\to-0}\hat{j}_0^i\cdot N_i}{Dk_1}\int_{-\infty}^{+\infty}\zeta(\Phi_0^i)(\Phi_0^i-(i-1))\,\mathrm{d}z\\
&\quad-\frac{v_i}{Dk_1}\int_{-\infty}^{+\infty}\zeta(\Phi_0^i)(\Phi_0^i-(i-1))(i-\Phi_0^i)\,\mathrm{d}z\\
&=-\lim_{r\to-0}\hat{w}_0^i+\gamma\frac{\lim_{r\to-0}\hat{j}_0^i\cdot N_i}{Dk_1}\int_0^1\frac{\zeta(\phi)}{\sqrt{2G(\phi)}}\phi\,\mathrm{d}\phi\\
&\quad-\gamma\frac{v_i}{Dk_1}\int_0^1\frac{\zeta(\phi)}{\sqrt{2G(\phi)}}\phi(1-\phi)\,\mathrm{d}\phi.
\end{aligned}$$

So, we obtain the boundary condition

$$\lim_{r\to-0}\hat{w}_0^i-\mu_0(\gamma+\gamma'')\kappa_i=\lim_{r\to-0}\hat{j}_0^i\cdot N_i\frac{\gamma}{Dk_1}\int_0^1\frac{\zeta(\phi)}{\sqrt{2G(\phi)}}\phi\,\mathrm{d}\phi + \frac{v_i}{\tilde{k}\gamma}-\frac{\gamma v_i}{Dk_1}\int_0^1\frac{\zeta(\phi)}{\sqrt{2G(\phi)}}\phi(1-\phi)\,\mathrm{d}\phi.$$

Besides (2.92), we are able to choose the asymmetric friction coefficient ζ such that

$$\frac{\gamma}{Dk_1}\int_0^1\frac{\zeta(\phi)}{\sqrt{2G(\phi)}}\phi\,\mathrm{d}\phi=\frac{1}{k_-}=\frac{1}{a_-k_0}. \tag{2.94}$$

The choice (2.93) of $\tilde{k}$ then yields

$$k_-\left(\lim_{r\to-0}\hat{w}_0^i-\mu\kappa_i\right)=\lim_{r\to-0}\hat{j}_0^i\cdot N_i$$

and, therefore, the boundary condition (2.18) to leading order.

Precise Choice of the Functions ζ, k_1 and $\tilde{k}$

Now, we want to present the concrete choices of the functions ζ, k_1 and $\tilde{k}$, which yield for given γ, $k_\pm$ and D the relations (2.92), (2.94) and (2.93). Here, we concentrate on the non-inverse ES barrier modelled by the relation $k_-\le k_+$. Thereby, we define

$$k_1:=k_0\gamma,$$

and we make the ansatz

$$\zeta(\phi):=\zeta_0\phi^2(1-\phi)^2\phi^{p_\zeta} \tag{2.95}$$

with $p_\zeta,\zeta_0\in\mathbb{R}$ satisfying $\zeta_0>0$ and $p_\zeta\ge0$. With this definition of ζ, one easily verifies that

$$\int_0^1\frac{\zeta(\phi)}{\sqrt{2G(\phi)}}(1-\phi)\,\mathrm{d}\phi=\frac{\zeta_0}{3(p_\zeta+2)(p_\zeta+3)(p_\zeta+4)}.$$

With this relation, (2.92) yields

$$\frac{\gamma\zeta_0}{3Dk_1(p_\zeta+2)(p_\zeta+3)(p_\zeta+4)}=\frac{1}{k_+}. \tag{2.96}$$

Similarly, one obtains

$$\int_0^1\frac{\zeta(\phi)}{\sqrt{2G(\phi)}}\phi\,\mathrm{d}\phi=\frac{\zeta_0}{6(p_\zeta+3)(p_\zeta+4)},$$

which is inserted into (2.94), and, therefore, we arrive at

$$\frac{\gamma\zeta_0}{6Dk_1(p_\zeta+3)(p_\zeta+4)} = \frac{1}{k_-}. \tag{2.97}$$

Now, we divide (2.96) by (2.97) in order to obtain for

$$q := k_-/k_+ = a_-/a_+$$

the relation

$$q = \frac{2}{p_\zeta+2},$$

from which we derive

$$p_\zeta = \frac{2}{q} - 2. \tag{2.98}$$

We insert (2.98) into (2.97) and get

$$\zeta_0 = \frac{6D(p_\zeta+3)(p_\zeta+4)}{a_-} = \frac{6D}{a_-}\left(\frac{2}{q}+1\right)\left(\frac{2}{q}+2\right). \tag{2.99}$$

From the definitions of p_ζ and q, it is clear that p_ζ displays the strength of the asymmetry in the attachment rates $k_\pm$, whereas ζ_0 is determined by the precise values of $k_\pm$ for a given ratio q. Finally, we use (2.93) in order to derive

$$\begin{aligned}\frac{1}{\tilde{k}} &= \frac{\gamma^2}{Dk_1}\int_0^1 \frac{\zeta(\phi)}{\sqrt{2G(\phi)}}\phi(1-\phi)\,\mathrm{d}\phi = \frac{\gamma}{6Dk_0}\int_0^1 \zeta(\phi)\,\mathrm{d}\phi \\ &= \frac{\zeta_0\gamma}{3Dk_0(p_\zeta+3)(p_\zeta+4)(p_\zeta+5)} = \frac{2\gamma}{k_0a_-(p_\zeta+5)} = \frac{2\gamma}{2k_+ + 3k_-}.\end{aligned} \tag{2.100}$$

Thus, one concludes that defining $\tilde{k}$ by (2.100) and ζ by (2.95) with p_ζ and ζ_0 given by (2.98) and (2.99), respectively, yields the equations (2.92), (2.94) and (2.93) as desired. If one is interested in a situation, where the attachment rates $k_\pm$ additionally include an asymmetry in the anisotropy — that means that $q = q(N_i)$ is anisotropic —, one obtains by (2.98) an anisotropic choice of p_ζ. Moreover, one sets $k_1 = 1$ and defines $\zeta_0 = \zeta_0(N_i)$ by the relation

$$\zeta_0 = \frac{6D(p_\zeta+3)(p_\zeta+4)}{\gamma k_-} = \frac{6D}{\gamma k_-}\left(\frac{2}{q}+1\right)\left(\frac{2}{q}+2\right)$$

and obtains, with (2.100) unchanged, the desired conditions (2.92), (2.94) and (2.93) in this situation. In order to model an inverse ES barrier implying $k_- > k_+$, one would have to make the ansatz

$$\zeta(\phi) = \zeta_0\phi^2(1-\phi)^2(1-\phi)^{p_\zeta}$$

for the asymmetric friction function ζ.

2.3 Numerical Treatment

In order to numerically treat the viscous Cahn-Hilliard equation (2.26)–(2.28), we apply an adaptive FEM strategy implemented in the FEM toolbox AMDiS [VV07]. After that, we validate in (2.3.2) the results of the asymptotic analysis in Section 2.2 in a simple one dimensional as well as in a rotationally symmetric situation. In Section 2.3.4, the influence of different anisotropies in different quantities on the island shape is discussed. Finally, following [KP98], a diffuse-interface approach is applied to spiral growth in Section 2.3.5.

Finite differences schemes have been applied for the simulation of one dimensional step trains [LM94] and spiral growth [KP98] by phase-field approximations of BCF models with thermodynamic boundary conditions. An Ehrlich-Schwoebel barrier in a diffuse-interface approximation has numerically been treated by finite differences in [OPR05] for a quantitative investigation of step bunching and the Bales-Zangwill instability of a periodic train of straight steps, which has also been numerically studied in [PL03].

2.3.1 Discretization

In this section, we present some details of a FEM discretization of the viscous Cahn-Hilliard equation, where we first show time- and space-discretizations of a semi-implicit scheme. Furthermore, a strategy of local mesh refinement and coarsening, based on an L^2-like error indicator for the phase-field variable ϕ, is described.

Weak Formulation and Discretization

First, we write the system of the viscous Cahn-Hilliard equation (2.26)–(2.28) as a system of two second order equations

$$\partial_t \phi = \nabla \cdot (M_\varepsilon(\phi, \nabla\phi)\nabla w) + F - \tau^{-1} w, \tag{2.101}$$

$$\varepsilon \tilde{k}^{-1}(n(\nabla\phi))\partial_t \phi = \mu_0 \left(\nabla \cdot E_p(\phi, \nabla\phi) - \varepsilon^{-1} G'(\phi)\right) + w \tag{2.102}$$

with $E_p(\phi, \nabla\phi)$ given by (2.37). In the simulation presented here, we will consider circular shaped domains with radius $r > 0$

$$\Omega = B_r(x_0) = \{x \in \mathbb{R}^2 : |x - x_0| < r\}$$

and square shaped domains

$$\Omega = (a, b) \times (a, b), \quad b > a.$$

In the first case, we assume no flux boundary conditions

$$\nabla\phi \cdot N = \nabla w \cdot N = 0 \quad \text{on} \quad \partial\Omega,$$

N denoting the outer normal to the boundary $\partial\Omega$, whereas, in the second case, we will assume either no flux boundary conditions on $\partial\Omega$ or (in Chapter 3) ϕ and w

to be Ω-periodic or different types of boundary conditions on different parts of the boundary $\partial\Omega$.

The time interval $[0, t_{\text{end}}]$ is split by discrete time instants $0 = t_0 < t_1 < \dots$, from which one gets the time steps $\Delta t_m := t_{m+1} - t_m$, $m = 0, 1, \dots$. The derivative of the multi well potential is linearized by

$$\begin{aligned} G'(\phi^{(m+1)}) &\approx G'(\phi^{(m)}) + G''(\phi^{(m)})(\phi^{(m+1)} - \phi^{(m)}) \\ &= G''(\phi^{(m)})\phi^{(m+1)} + G'(\phi^{(m)}) - G''(\phi^{(m)})\phi^{(m)}. \end{aligned} \tag{2.103}$$

Since $n(p) = -\frac{p}{|p|}$ is not defined for $p = 0$, one has to decide how to define the anisotropy functions γ, k_0 and ν occurring in the mobility M_ε and in the kinetic coefficient $\tilde{k}$ for $p = 0$. For the applications in this chapter, we choose anisotropy functions depending on the angle $\theta = \theta(n)$, where we rewrite those functions as polynomials in n. Then, we obtain by introducing a regularization of the form

$$n_\varepsilon(p) = -\frac{p}{|p| + \alpha(\varepsilon)}, \quad \alpha(\varepsilon) = \mathcal{O}(\varepsilon),$$

continuous anisotropy functions $\gamma \circ n_\varepsilon$, $\nu \circ n_\varepsilon$ and $k_0 \circ n_\varepsilon$ for the use in kinetic coefficients and mobility functions. Similarly, for applications in Chapter 3, we choose anisotropy functions (also for higher dimensions), where a regularization of the form $n_\varepsilon(p) = -\frac{p}{|p|+\alpha(\varepsilon)}$ leads to well defined anisotropic quantities for all vectors p. In the following of this section, we drop the ε in n_ε, and, in addition, we do not change the notation M_ε for the mobility function and denote the mobility function including regularized anisotropy functions with M_ε. Furthermore, we set

$$A = A(\nabla\phi) := \begin{pmatrix} \gamma^2 & -\gamma\gamma' \\ \gamma\gamma' & \gamma^2 \end{pmatrix} (n(\nabla\phi)).$$

By explicit treatment of the phase-field variable in the mobility M_ε and in all anisotropy functions, one ends up with the weak formulation and semi-implicit time discretization (see also [BP03])

$$\begin{aligned} &\frac{1}{\Delta t_m}\int_\Omega \phi^{(m+1)}\psi + \int_\Omega M_\varepsilon(\phi^{(m)}, \nabla\phi^{(m)})\nabla w^{(m+1)} \cdot \nabla\psi + \tau^{-1}\int_\Omega w^{(m+1)}\psi \\ &= \frac{1}{\Delta t_m}\int_\Omega \phi^{(m)}\psi + \int_\Omega F\psi \qquad \forall \psi \in X, \\ &\frac{\varepsilon}{\Delta t_m}\int_\Omega \tilde{k}^{-1}(n(\nabla\phi^{(m)}))\phi^{(m+1)}\psi + \varepsilon\mu_0\int_\Omega A(\nabla\phi^{(m)})\nabla\phi^{(m+1)} \cdot \nabla\psi \\ &\qquad + \varepsilon^{-1}\mu_0\int_\Omega G''(\phi^{(m)})\phi^{(m+1)}\psi - \int_\Omega w^{(m+1)}\psi \\ &= \frac{\varepsilon}{\Delta t_m}\int_\Omega \tilde{k}^{-1}(n(\nabla\phi^{(m)}))\phi^{(m)}\psi \\ &\qquad + \varepsilon^{-1}\mu_0\int_\Omega (G''(\phi^{(m)})\phi^{(m)} - G'(\phi^{(m)}))\psi \qquad \forall \psi \in X, \end{aligned}$$

where $X := \mathrm{H}^1(\Omega)$ in the case of no flux boundary conditions and $X := \mathrm{H}^1_{\mathrm{per}}(\Omega)$ in the periodic case, where $\mathrm{H}^1_{\mathrm{per}}(\Omega) := \mathrm{H}^1(T_{a,b})$ denotes the Sobolev space on the torus $T_{a,b} := (\mathbb{R}/(b-a)\mathbb{Z})^2$.

Furthermore, a simple strategy of time adaptivity is used, where the time step is inversely proportional to the maximum of the normal velocity of the Cahn-Hilliard interface. The concrete choice of the time step, thereby, guarantees that the interface is not able to move in one time step through a whole element.

To discretize in space, let $\mathcal{T}_h^m$ be a conforming triangulation of Ω at time instant t_m. Denote the set of polynomials of degree 1 with $\mathbb{P}^1$ and define the finite element space of globally continuous, piecewise linear elements

$$\mathbb{V}_h^m = \left\{ v_h \in X \ : \ v_h|_T \in \mathbb{P}^1 \ \ \forall T \in \mathcal{T}_h^m \right\}.$$

The space discretization now reads: Find $\phi_h^{m+1}, w_h^{m+1} \in \mathbb{V}_h^m$ such that

$$\begin{aligned}
&\frac{1}{\Delta t_m}\int_\Omega \phi_h^{(m+1)}\psi_h + \int_\Omega M_\varepsilon(\phi_h^{(m)}, \nabla\phi_h^{(m)})\nabla w_h^{(m+1)} \cdot \nabla\psi_h + \tau^{-1}\int_\Omega w_h^{(m+1)}\psi_h \\
&= \frac{1}{\Delta t_m}\int_\Omega \phi_h^{(m)}\psi_h + \int_\Omega F\psi_h \qquad \forall \psi_h \in \mathbb{V}_h^m, \\
&\frac{\varepsilon}{\Delta t_m}\int_\Omega \tilde{k}^{-1}(n(\nabla\phi_h^{(m)}))\phi_h^{(m+1)}\psi_h + \varepsilon\mu_0\int_\Omega A(\nabla\phi_h^{(m)})\nabla\phi_h^{(m+1)} \cdot \nabla\psi_h \\
&\qquad + \varepsilon^{-1}\mu_0\int_\Omega G''(\phi_h^{(m)})\phi_h^{(m+1)}\psi_h - \int_\Omega w_h^{(m+1)}\psi_h \\
&= \frac{\varepsilon}{\Delta t_m}\int_\Omega \tilde{k}^{-1}(n(\nabla\phi_h^{(m)}))\phi_h^{(m)}\psi_h \\
&\qquad + \varepsilon^{-1}\mu_0\int_\Omega (G''(\phi_h^{(m)})\phi_h^{(m)} - G'(\phi_h^{(m)}))\psi_h \qquad \forall \psi_h \in \mathbb{V}_h^m.
\end{aligned}$$

With $(\psi_i)_i$ the standard nodal basis of $\mathbb{V}_h^m$ and $\phi_h^{(m+1)} = \sum_i \Phi_i^{(m+1)}\psi_i$ and $w_h^{(m+1)} = \sum_i W_i^{(m+1)}\psi_i$, these equations lead to a linear system of equations

$$\begin{aligned}
&\frac{1}{\Delta t_m}\boldsymbol{M}\Phi^{(m+1)} + \boldsymbol{A}^1 W^{(m+1)} + \tau^{-1}\boldsymbol{M}W^{(m+1)} = \boldsymbol{F} + \frac{1}{\Delta t_m}\boldsymbol{M}\Phi^{(m)}, \\
&\frac{\varepsilon}{\Delta t_m}\boldsymbol{M}^k\Phi^{(m+1)} + \varepsilon\mu_0\boldsymbol{A}^2\Phi^{(m+1)} + \varepsilon^{-1}\mu_0\boldsymbol{G}^{\mathrm{impl}}\Phi^{(m+1)} - \boldsymbol{M}W^{(m+1)} \\
&\qquad = \varepsilon^{-1}\mu_0\boldsymbol{G}^{\mathrm{expl}} + \frac{\varepsilon}{\Delta t_m}\boldsymbol{M}^k\Phi^{(m)}
\end{aligned}$$

for $\Phi^{(m+1)}$ and $W^{(m+1)}$ with

$$\begin{aligned}
\boldsymbol{M} &= (M_{ij}) & M_{ij} &= (\psi_i, \psi_j)_\Omega, \\
\boldsymbol{M}^k &= (M_{ij}^k) & M_{ij}^k &= (\tilde{k}^{-1}(n(\nabla\phi_h^{(m)}))\psi_i, \psi_j)_\Omega, \\
\boldsymbol{A}^1 &= (A_{ij}^1) & A_{ij}^1 &= (M_\varepsilon(\phi_h^{(m)}, \nabla\phi_h^{(m)})\nabla\psi_i, \nabla\psi_j)_\Omega, \\
\boldsymbol{A}^2 &= (A_{ij}^2) & A_{ij}^2 &= (A(\nabla\phi_h^{(m)})\nabla\psi_i, \nabla\psi_j)_\Omega, \\
\boldsymbol{F} &= (F_i) & F_i &= (F, \psi_i)_\Omega, \\
\boldsymbol{G}^{\mathrm{impl}} &= (G_{ij}^{\mathrm{impl}}) & G_{ij}^{\mathrm{impl}} &= (G''(\phi_h^{(m)})\psi_i, \psi_j)_\Omega, \\
\boldsymbol{G}^{\mathrm{expl}} &= (G_i^{\mathrm{expl}}) & G_i^{\mathrm{expl}} &= (G''(\phi_h^{(m)})\phi_h^{(m)} - G'(\phi_h^{(m)}), \psi_i)_\Omega,
\end{aligned}$$

where $(\cdot,\cdot)_\Omega$ denotes L^2-scalar product. Thus, written in block-matrix-form the non-symmetric linear system

$$\begin{pmatrix} \boldsymbol{A}^1 + \tau^{-1}\boldsymbol{M} & \frac{1}{\Delta t_m}\boldsymbol{M} \\ -\boldsymbol{M} & \frac{\varepsilon}{\Delta t_m}\boldsymbol{M}^k + \varepsilon\mu_0\boldsymbol{A}^2 + \varepsilon^{-1}\mu_0\boldsymbol{G}^{\mathrm{impl}} \end{pmatrix} \begin{pmatrix} W^{(m+1)} \\ \Phi^{(m+1)} \end{pmatrix} = \begin{pmatrix} \boldsymbol{F} + \frac{1}{\Delta t_m}\boldsymbol{M}\Phi^{(m)} \\ \varepsilon^{-1}\mu_0\boldsymbol{G}^{\mathrm{expl}} + \frac{\varepsilon}{\Delta t_m}\boldsymbol{M}^k\Phi^{(m)} \end{pmatrix}$$

has to be solved in every time step, which is done by a stabilized bi-conjugate gradient method (BiCGStab). In order to verify the regularity of the system matrix on the left hand side of the above system (see [RV06]), we assume that (W, Φ) is a solution of the homogeneous linear system. We denote the corresponding functions in $\mathbb{V}_h$ by w_h and ϕ_h. Then, we arrive at the homogeneous system

$$\frac{1}{\Delta t_m}\int_\Omega \phi_h\psi + \int_\Omega M_\varepsilon(\phi^0, \nabla\phi^0)\nabla w_h \cdot \nabla\psi + \tau^{-1}\int_\Omega w_h\phi = 0, \tag{2.104}$$

$$\begin{aligned} -\int_\Omega w_h\psi + \varepsilon\int_\Omega A(\nabla\phi^0)\nabla\phi_h \cdot \nabla\psi \\ + \varepsilon^{-1}\int_\Omega G''(\phi^0)\phi_h\psi + \frac{\varepsilon}{\Delta t_m}\int_\Omega \tilde{k}^{-1}(\nabla\phi^0)\phi_h\psi = 0 \end{aligned} \tag{2.105}$$

for all $\psi \in \mathbb{V}_h$ and for some $\phi^0 \in \mathbb{V}_h$. Then, by using in (2.104) the test function $\psi = w_h$, we obtain

$$\frac{1}{\Delta t_m}(\phi_h, w_h)_\Omega + (M_\varepsilon(\phi^0, \nabla\phi^0)\nabla w_h, \nabla w_h)_\Omega + \tau^{-1}(w_h, w_h)_\Omega = 0$$

and, therefore,

$$(\phi_h, w_h)_\Omega \le 0. \tag{2.106}$$

Now, we use in (2.105) the test function $\psi = \phi_h$ and arrive at

$$\begin{aligned} -(\phi_h, w_h)_\Omega + \frac{\varepsilon}{\Delta t_m}(\tilde{k}^{-1}(\nabla\phi^0)\phi_h, \phi_h)_\Omega \\ + \varepsilon(A(\nabla\phi^0)\nabla\phi_h, \nabla\phi_h)_\Omega + \varepsilon^{-1}(G''(\phi^0)\phi_h, \phi_h)_\Omega = 0. \end{aligned}$$

Using (2.106) and

$$(A(\nabla\phi^0)\nabla\phi_h, \nabla\phi_h)_\Omega \geq 0,$$

one gets with $\|\phi_h\|_\Omega := \sqrt{(\phi_h, \phi_h)_\Omega}$

$$\frac{\varepsilon}{\Delta t_m}\|\phi_h\|_\Omega^2 \leq \varepsilon^{-1} \sup\left(\tilde{k}\right) \sup\left(|G''|\right) \ \|\phi_h\|_\Omega^2.$$

If we choose Δt_m sufficiently small, we obtain $\|\phi_h\|_\Omega = 0$ and, therefore, $\phi_h = w_h = 0$ showing the regularity of the system matrix in the above linear system.

Adaptive Strategy of Local Refinement and Coarsening

To obtain satisfactory computational results, a mesh with a sufficiently fine resolution near the interface (ϕ changes rapidly) is needed. Noting that a uniform refinement would be prohibitive from the computational point of view, we are naturally led to adopt local mesh refinement. Since the interface is moving, it is indispensable to use some adaptive strategy for local mesh refinement and coarsening. At every time step, the finite element mesh from the previous time step is locally refined and/or coarsened. For local mesh adaptation, we use an L^2-like error indicator for the smeared height function ϕ. For every element T, we define

$$\eta_T(\phi_h) := \left(\sum_{e \in \partial T} \int_e h^3 \left| \left[\frac{\partial \phi_h}{\partial n_e} \right] \right|^2 \right)^{1/2}, \tag{2.107}$$

where $\left[\frac{\partial \phi_h}{\partial n_e}\right]$ denotes the jump of the normal derivative of ϕ_h across an edge $e \subset \partial T$. This can be used to define an indicator for the error $\|\phi - \phi_h\|$ on the whole domain

$$\eta(\phi_h) := \left(\sum_{T \in \mathcal{T}_h^m} \eta_T^2(\phi_h) \right)^{1/2}.$$

The criterion for refinement and coarsening is based on an equidistribution strategy, which attempts to enforce $\eta_T(\phi_h) = \eta_{T'}(\phi_h)$ for all $T, T' \in \mathcal{T}_h^m$. If this condition was enforced, at least approximately, then, we would have

$$\eta(\phi_h) \approx N_m^{1/2} \eta_T(\phi_h),$$

where N_m is the number of triangular finite elements in $\mathcal{T}_h^m$. Thus, we mark an element $T \in \mathcal{T}_h^m$ for refinement and/or coarsening, if

$$\eta_T(\phi_h) > \frac{\eta(\phi_h)}{N_m^{1/2}}, \quad \eta_T(\phi_h) \leq \xi \frac{\eta(\phi_h)}{N_m^{1/2}},$$

respectively, with some $\xi \in (0, 1)$. Heuristic arguments yield that the local indicator (2.107) is large, where the graph of ϕ has a large curvature, i.e. in exactly those regions, where one wants to have a high resolution.

2.3.2 Comparison with Analytic Solutions

In this section, we compare numerical solutions of the diffuse-interface approximation (2.26)–(2.28) with analytic solutions of the BCF model in one dimension and radially symmetric solutions in two dimensions, where both types of boundary conditions (TBC and KBC) are considered. Furthermore, no anisotropy functions are used.

Single Step in One Dimension

To be more precise, we first consider the system (2.15), (2.16), (2.17), (2.22) in the interval $I := [-1, 1]$ without the curvature terms in (2.17) and (2.22), which are meaningless in the one dimensional case. We assume no flux boundary conditions for the adatom concentration

$$w'(\pm 1) = 0$$

on the boundary of I. In addition, the time interval $[0, 1]$ and the initial interface $\Gamma(0) = \{0\}$, representing a single step, are considered, where $I_0 = (0, 1)$ and $I_1 = (-1, 0)$ denote the lower and upper terrace, respectively, at time $t = 0$. Let $R = R(t)$ denote the interface position, i.e. $\Gamma(t) = \{R(t)\}$. Then, the analytic solution to the quasi-stationary BCF model with thermodynamic boundary conditions is then given by

$$\begin{aligned} w_0(x) &= -\frac{F}{2D}\left(x^2 - R^2\right) + \frac{F}{D}(x - R) + \frac{2}{k}F \quad \text{for} \quad x > R, \\ w_1(x) &= -\frac{F}{2D}\left(x^2 - R^2\right) - \frac{F}{D}(x - R) + \frac{2}{k}F \quad \text{for} \quad x \leq R, \end{aligned}$$

where

$$R(t) = 2Ft \tag{2.108}$$

holds. For the viscous Cahn-Hilliard equation, we assume no flux boundary conditions

$$\phi'(\pm 1) = w'(\pm 1) = 0$$

on ∂I and the initial condition

$$\phi(x, 0) = \frac{1}{2}\left(1 - \tanh\left(\frac{3x}{\varepsilon}\right)\right).$$

Additionally, we have used constant time steps of length $\Delta t = 2 \cdot 10^{-4}$ and uniform meshes. Then, we choose the following set of academic parameters

$$k = 1; \quad \mu = 1; \quad D = 10; \quad F = 0.1; \quad \tau^{-1} = 0. \tag{2.109}$$

First, we consider for $\varepsilon = 0.1$ the behaviour of the discrete adatom density w_h for different grid sizes h with the adatom profile at time $t = 1$ in Figure 2.7 (left). One can see in Figure 2.7 in the left picture a monotone convergence of w_h as h decreases

to a function which differs from the analytic solution due to the ε-error of the diffuse-interface model. One can investigate this more quantitatively by introducing the relative L^2-error

$$e_{w_h} := \frac{\|w - w_h\|_{\mathrm{L}^2(I)}}{\|w\|_{\mathrm{L}^2(I)}},$$

which is considered in the time interval $[0, 1]$ in the picture on the right of Figure 2.7, where, for the analytic adatom density, we have used the numerically by $\phi_h = 1/2$ determined interface position. Now, we want to numerically reproduce the results of

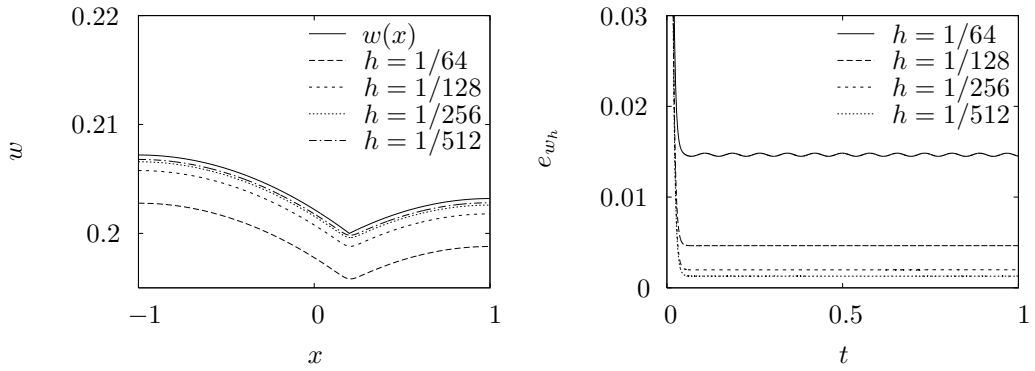

Figure 2.7: Behaviour of profiles of w_h at $t = 1.0$ (left) and of relative L^2-error e_{w_h} (right) as $h \to 0$ (TBC).

the asymptotic analysis, i.e. we compare the numerical results for decreasing ε with the analytic solution in the right picture of Figure 2.8 and in the relative L^2-error on the right. Here, we have used a constant resolution of the diffuse interface region determined by $2\varepsilon/h = 51.2$.

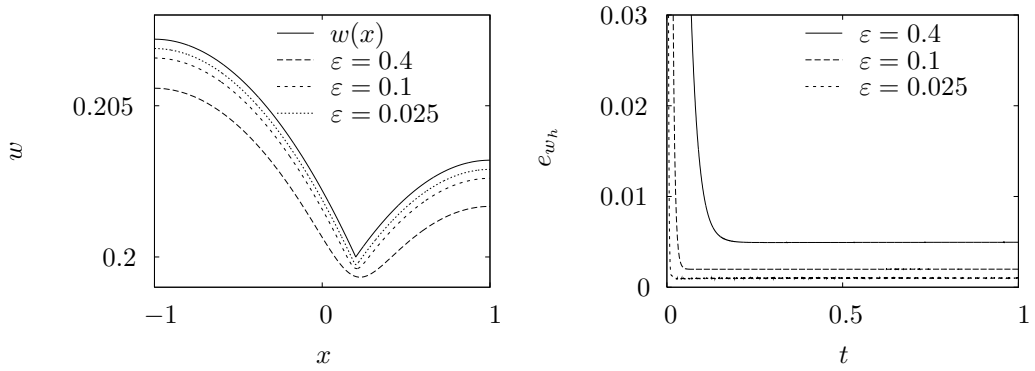

Figure 2.8: Convergence of profiles of w_h at $t = 1.0$ towards analytic solution w (left) and relative L^2-error e_{w_h} (right) as $\varepsilon \to 0$ (TBC).

In the case of kinetic boundary conditions, we consider in a one dimensional situation the same interval with the same initial and boundary conditions. Here,

the analytic solution of the adatom concentration in the quasi-stationary BCF model is

$$w_0(x) = -\frac{F}{2D}\left(x^2 - R^2\right) + \frac{F}{D}(x - R) + \frac{F}{k_+}(1 - R) \quad \text{for} \quad x > R,$$
$$w_1(x) = -\frac{F}{2D}\left(x^2 - R^2\right) - \frac{F}{D}(x - R) + \frac{F}{k_-}(1 + R) \quad \text{for} \quad x \leq R$$

with the interface position given by (2.108). We have reused the parameters (2.109), where instead of k, we have used

$$k_+ = 10; \quad k_- = 1. \tag{2.110}$$

The pictures corresponding to Figure 2.7 in the KBC case showing the convergence of the discrete adatom densities w_h as $h \to 0$ can be found in Figure 2.9. The results

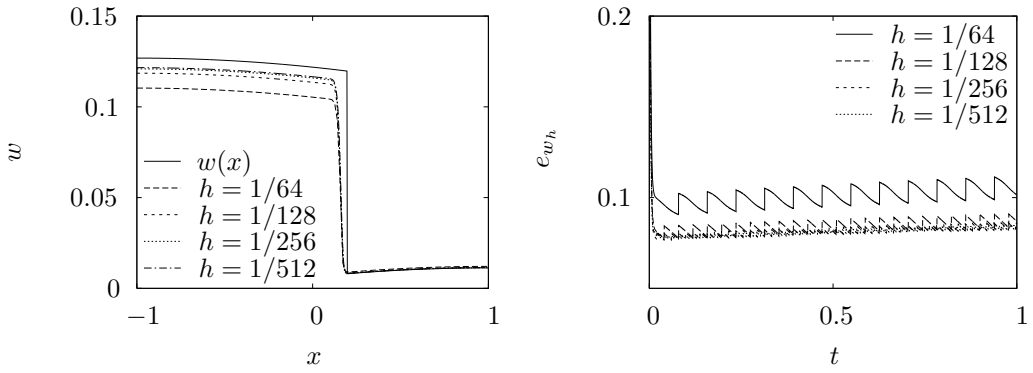

Figure 2.9: Behaviour of profiles of w_h at $t = 1.0$ (left) and of relative L^2-error e_{w_h} (right) as $h \to 0$ (KBC).

of the numerical validation of the asymptotic analysis are given in Figure 2.10, where on the left one can see the excellent resolution of the jump at the interface for decreasing ε for $t = 1$. This convergence can again be recognized in the plots of the relative L^2-errors on the right.

Circular Epitaxial Island

In the two dimensional case, we consider for the isotropic situation ($\gamma = 1$, $\mu = \mu_0$) a circular shaped domain $\Omega := B_{R_\infty}(0)$ with $R_\infty = 5$ and the time interval $[0, t_\infty]$ with $t_\infty := \frac{1-(R_0/R_\infty)^2}{F}$. Besides no flux boundary conditions

$$\nabla w(x,t) \cdot N = 0 \quad \text{for} \quad x \in \partial\Omega,$$

the initial circular shaped epitaxial island $\Gamma(t = 0) = \partial B_{R_0}(0)$ with $R_0 = 2$ is introduced. The quasi-stationary rotationally symmetric analytic solution of the

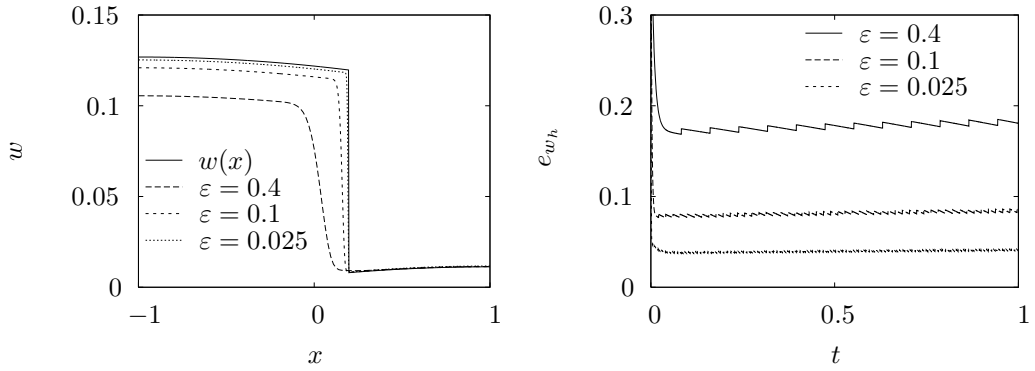

Figure 2.10: Convergence of profiles of w_h at $t = 1.0$ towards analytic solution w (left) and relative L^2-error e_{w_h} (right) as $\varepsilon \to 0$ (KBC).

adatom density in this situation is (see [LRV04])

$$w_0(r) = \frac{F}{4D}\left(R^2 - r^2\right) + \frac{FR_\infty^2}{2D}\log\left(\frac{r}{R}\right) + \frac{\mu}{R} + \frac{FR_\infty^2}{2kR} \quad \text{for} \quad r > R,$$
$$w_1(r) = \frac{F}{4D}\left(R^2 - r^2\right) + \frac{\mu}{R} + \frac{FR_\infty^2}{2kR} \quad \text{for} \quad r \leq R$$

with $r := |x|$ and $\Gamma(t) = \partial B_{R(t)}(0)$, where

$$R(t) = \sqrt{R_0^2 + FR_\infty^2 t}. \tag{2.111}$$

By (2.111) one obtains the relation $R(t_\infty) = R_\infty$. As before, for the viscous Cahn-Hilliard equation, no flux boundary conditions

$$\nabla w(x,t) \cdot N = \nabla \phi(x,t) \cdot N = 0 \quad \text{for} \quad x \in \partial\Omega$$

are assumed, and the initial condition corresponding to the ones of the sharp-interface model is

$$\phi(x,0) = \frac{1}{2}\left(1 - \tanh\left(\frac{3(|x| - R_0)}{\varepsilon}\right)\right). \tag{2.112}$$

Furthermore, we use the same parameters as in the one dimensional case, except $\mu = 0.1$ instead of $\mu = 1$ and $k = 100$ instead of $k = 1$ and $\nu = 0$. For this test case, a simple adaptive strategy of mesh refinement and coarsening has been applied, where a basic mesh with 4096 elements and uniform local refinement with at least $P \in \mathbb{N}$ vertices in the diffuse interface region (see mesh for $P = 10$ in Figure 2.11 and details of meshes for different values of P in Figure 2.12). Moreover, we have used the constant time steps $\Delta t = 2 \cdot 10^{-4}$. With this in mind, we consider cross sections of profiles of the discrete adatom density w_h at time $t = 0.5$ for different resolutions in Figure 2.13. In the first picture on the left, one can hardly notice a difference in the plots. The zoomed in one on the right shows a slight difference

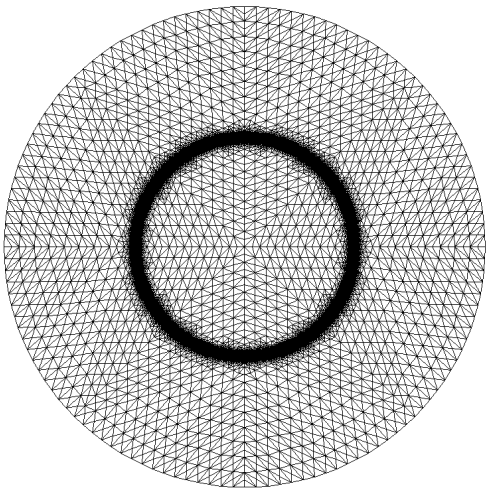

Figure 2.11: Mesh for $P = 10$.

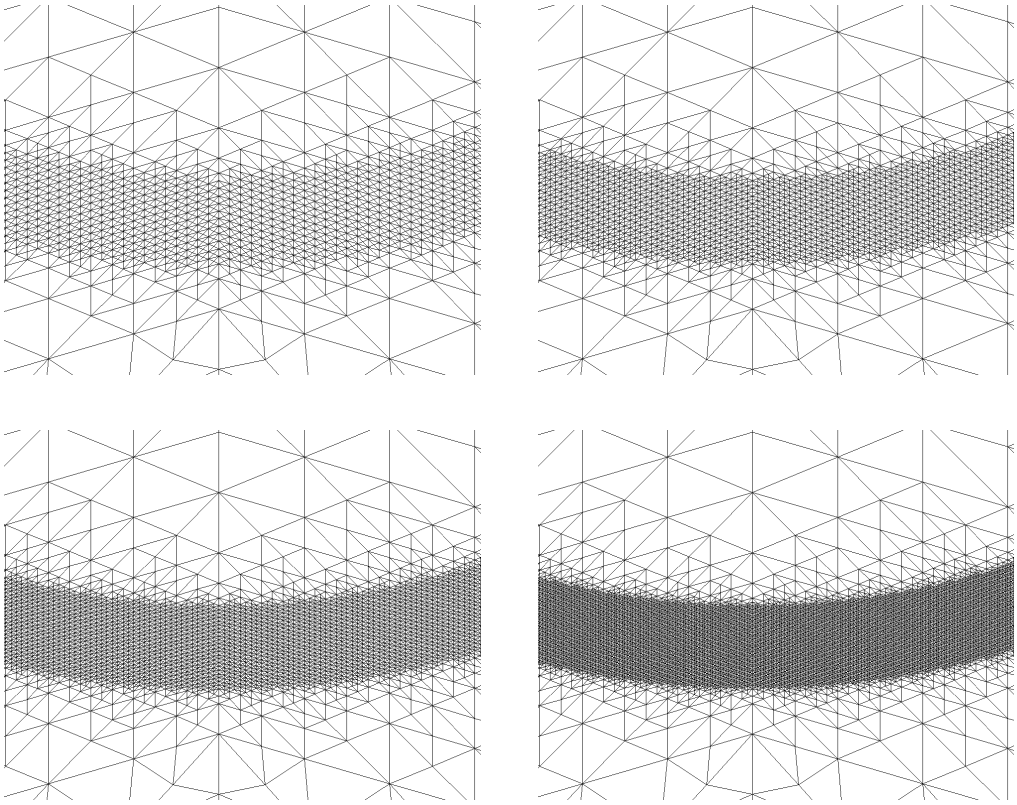

Figure 2.12: Meshes for $P = 10$, $P = 15$, $P = 20$ and $P = 25$ (top left to bottom right).

for different resolutions and that the graphs for 20 and 25 grid points per interface region are indistinguishable. For a more detailed investigation, we consider the

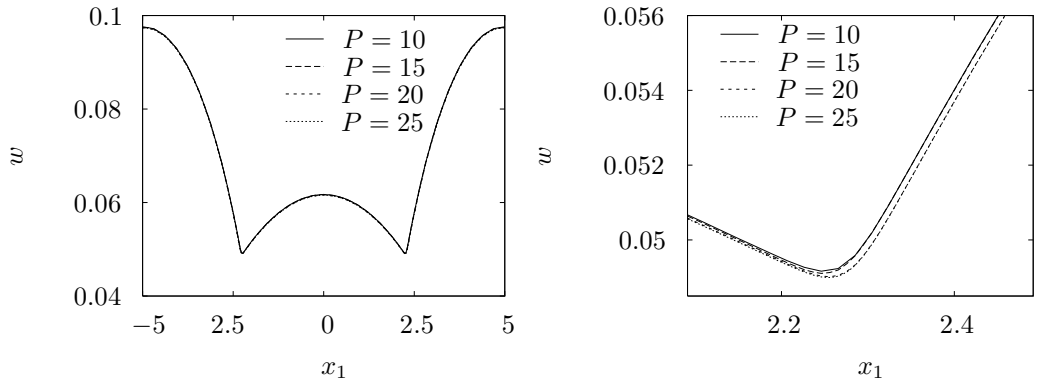

Figure 2.13: Behaviour of w_h at $t = 0.5$ for $x_1 \in [-5, 5]$ (left) and zoomed in (right) as $h \to 0$ (TBC).

relative L^2-error e_{w_h} of the discrete adatom density w_h

$$e_{w_h} := \frac{\|w - w_h\|_{\mathrm{L}^2(\Omega)}}{\|w\|_{\mathrm{L}^2(\Omega)}}.$$

In Figure 2.14, one can see, how e_{w_h} behaves in the time interval $[0, 0.5]$. Here, it is remarkable that the convergence of the relative error with $h \to 0$ does not have to be monotone, one gets a better approximation of the analytic solution with a coarser mesh due to the fact that there is also an error contribution from ε-approximation of the diffuse-interface model. However, these differences are on a very fine level. In the case of kinetic boundary conditions, the situation is different due to the jump of the adatom concentration at the interface, which has to be resolved and is there responsible of the main error contribution.

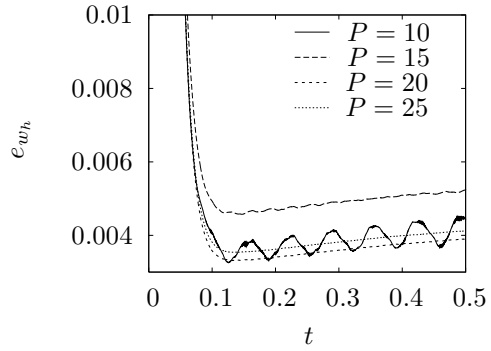

Figure 2.14: Relative L^2-error e_{w_h} of the discrete adatom density w_h in the time interval $[0, 0.5]$ for different values of h (TBC).

Denoting by $\phi_0 = \phi_0(x, t)$ the indicator function being one on the upper terrace and zero on the lower and given by (2.111) we consider the approximation of ϕ_0

for $t = 0.5$ for different values of ε with fixed resolution $P = 20$ (see Figure 2.15 for cross sections through the profile of the smeared out height function ϕ) by the solution of the diffuse-interface approximation. One can see that the diffuse-interface

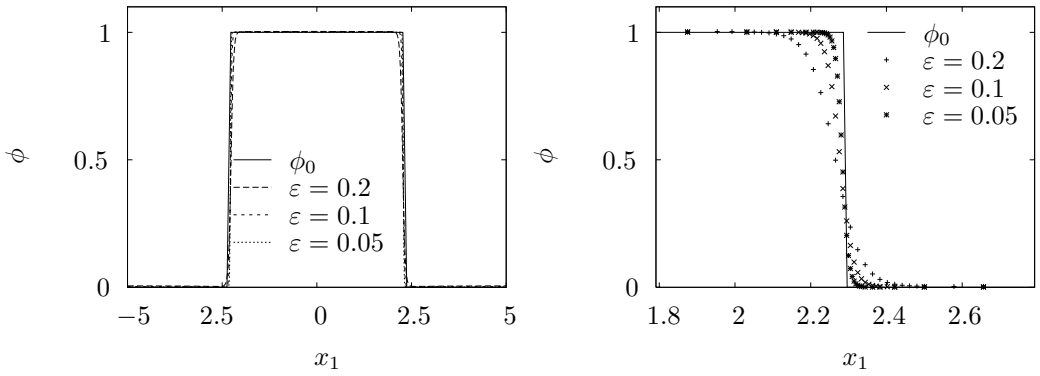

Figure 2.15: Approximation of indicator function ϕ_0 by smeared out height function ϕ_h at $t = 0.5$ for $x_1 \in [-5, 5]$ (left) and zoomed in (right) as $\varepsilon \to 0$.

approximation is "behind" ϕ_0 (see also the comparison of the numerically determined radii with the theoretical one for $t = 0.5$ in Table 2.1), however, this distance shrinks to zero as $\varepsilon \to 0$. The reason for this is that the values of the smeared out height function are slightly above zero on the lower terrace and above one on the upper terrace. According to this aspect some part of the mass is not used for the propagation of the step given by the level set $\{\phi = 1/2\}$. This property of a diffuse-interface approximation of a BCF model has already been pointed out in [OPR05].

$R(\varepsilon = 0.2)$	$R(\varepsilon = 0.1)$	$R(\varepsilon = 0.05)$	R(theory)
2.265	2.278	2.284	2.291

Table 2.1: Comparison of numerically and theoretically determined radii for $t = 0.5$.

Now we want to investigate the behaviour of solutions of the viscous Cahn-Hilliard equation for decreasing ε, where the resolution at the interface has been fixed by $P = 20$. Figure 2.16 shows cross sections of profiles of the analytic adatom concentration and of discrete adatom densities for different values of ε at time $t = 0.5$ illustrating the convergence of the solutions of the diffuse-interface approximations towards the analytic solution as $\varepsilon \to 0$. This convergence can also be demonstrated by the plots of the relative error in the time interval $[0, 0.5]$ in Figure 2.17. It also indicates that it takes some time for the adatom concentration to build up and that this time decreases with decreasing ε as stated in [OPR05].

Now similar considerations are presented in the case of kinetic boundary conditions (KBC), where one obtains for the quasi-stationary BCF model in this situation

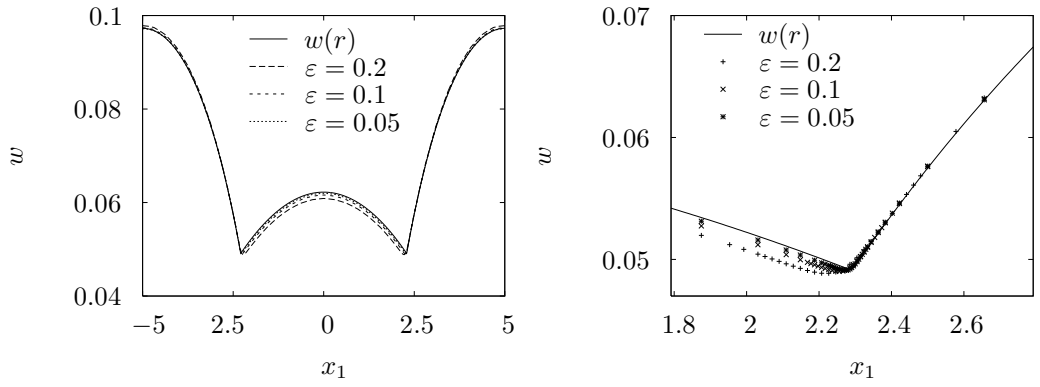

Figure 2.16: Approximation of the analytic adatom concentration w by discrete adatom concentrations at $t = 0.5$ for $x_1 \in [-5, 5]$ (left) and zoomed in (right) as $\varepsilon \to 0$ (TBC).

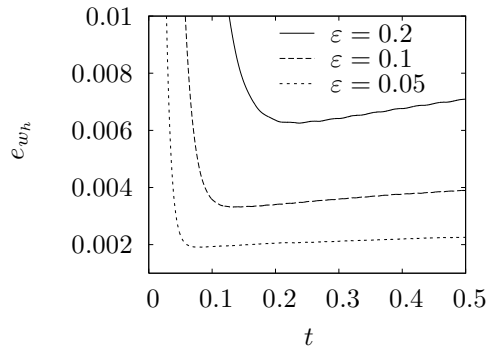

Figure 2.17: Relative L^2-error e_{w_h} of the discrete adatom density w_h in the time interval $[0, 0.5]$ for different values of ε (TBC).

the rotationally symmetric analytic adatom concentration (see [LRV04])

$$w_0(r) = \frac{F}{4D}\left(R^2 - r^2\right) + \frac{FR_\infty^2}{2D}\log\left(\frac{r}{R}\right) + \frac{\mu}{R} + \frac{F}{2k_+}\left(\frac{R_\infty^2}{R} - R\right) \quad \text{for} \quad r > R,$$

$$w_1(r) = \frac{F}{4D}\left(R^2 - r^2\right) + \frac{\mu}{R} + \frac{FR}{2k_-} \quad \text{for} \quad r \le R$$

with $R = R(t)$ still given by (2.111). Again, we have used the same adaptive strategy and basic mesh as well as the same constant time steps and parameters as in the case of thermodynamic boundary conditions (additionally using the kinetic coefficients (2.110)). Then we first look at the adatom concentration w_h at time $t = 0.5$ for different resolutions in Figure 2.18, where one can observe a monotone convergence for increasing P, which can also be noticed in Figure 2.19 showing the relative errors of w_h in the time interval $[0, 0.5]$. This error is one order of magnitude larger than the corresponding errors in the case of thermodynamic boundary conditions.

Now, we concentrate on the resolution of the jump in the adatom density at the interface as $\varepsilon \to 0$, where in Figure 2.20, again cross sections of the profiles of the

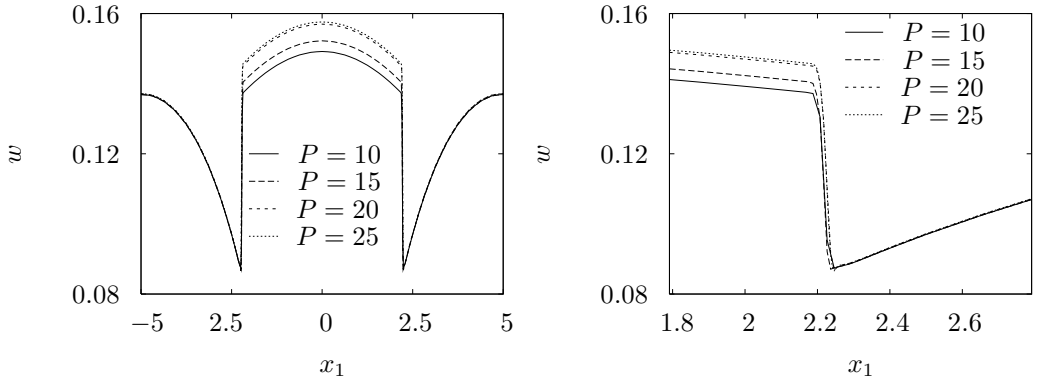

Figure 2.18: Behaviour of w_h at $t = 0.5$ for $x_1 \in [-5, 5]$ (left) and zoomed in (right) as $h \to 0$ (KBC).

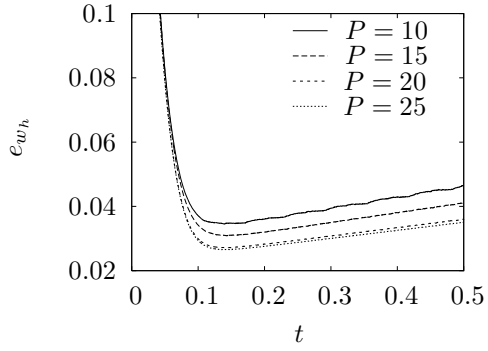

Figure 2.19: Relative L^2-error e_{w_h} of the discrete adatom density w_h in the time interval $[0, 0.5]$ for different values of h (KBC).

adatom concentrations for different values of ε are compared to those of the analytic solution of the rotationally symmetric problem. This convergence is also illustrated in the relative L^2-errors in Figure 2.21.

Thus, the numerical results for mathematically one dimensional situations in this section support the results of the asymptotic expansions in (2.2) showing that the viscous Cahn-Hilliard equation (2.26)–(2.28) with either mobility function (2.30) or (2.32) yields a reasonable quantitative approximation of the BCF model with either thermodynamic or kinetic boundary conditions for small ε. Especially the resolution of a jump in the adatom concentration for kinetic boundary conditions by a diffuse-interface approximation could be shown.

2.3.3 Comparison with Stability Analysis

In this section, we follow the stability analysis for a single circular island presented in [LRV04] and consider the circular domain $\Omega := B_{R_\infty}(0)$, the boundary of a circular island ∂B_{R_0} and a perturbed interface $\tilde{\Gamma} := \partial B_{\tilde{R}}(0)$ with a perturbation

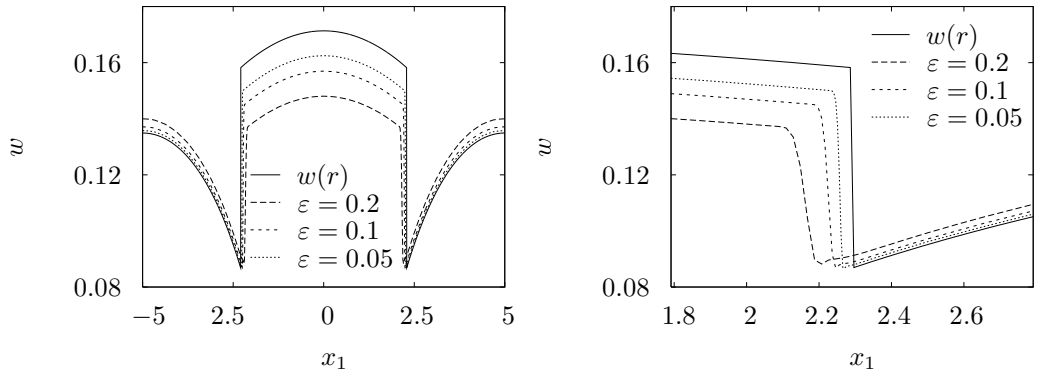

Figure 2.20: Approximation of the analytic adatom concentration w by discrete adatom concentrations at $t = 0.5$ for $x_1 \in [-5, 5]$ (left) and zoomed in (right) as $\varepsilon \to 0$ (KBC).

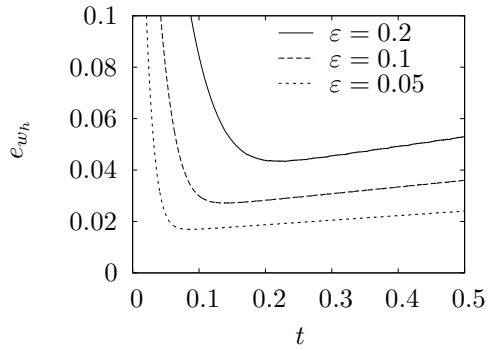

Figure 2.21: Relative L^2-error e_{w_h} of the discrete adatom density w_h in the time interval $[0, 0.5]$ for different values of ε (KBC).

$\tilde{R} := R_0 + A_0 \cos l\theta$ of the radius R_0 with amplitude A_0 and wavenumber l. For the growth rate $\omega = \omega(l, t)$, one obtains (see [LRV04])

$$\begin{aligned}\partial_t\omega(l,t) = &-\frac{F}{2\mathcal{A}} - \frac{Dl\left(\frac{F}{2} + \frac{k_- F R_\infty \mathcal{A}^{1/2}}{2D} + \frac{k_-\mu(l^2-1)}{R_\infty^2\mathcal{A}}\right)}{Dl + k_- R_\infty \mathcal{A}^{1/2}} \\ &+ \frac{Dl\left(1-\mathcal{A}^l\right)\left(\frac{F}{2}\left(1+\frac{1}{\mathcal{A}}\right) + \frac{k_+ F R_\infty \mathcal{A}^{1/2}}{2D}\left(\frac{1}{\mathcal{A}}-1\right) - \frac{k_+\mu(l^2-1)}{R_\infty^2\mathcal{A}}\right)}{k_+ R_\infty \mathcal{A}^{1/2}\left(\mathcal{A}^l+1\right) + Dl\left(1-\mathcal{A}^l\right)},\end{aligned} \tag{2.113}$$

where $\mathcal{A} = \mathcal{A}(t) := R^2(t)/R_\infty^2$ denotes the rescaled area of the unperturbed island (see (2.111)). For the extreme case $k_+ = \infty, k_- = 0, \mu = 0$ relation (2.113) reduces to

$$\partial_t\omega(l,t) = -\frac{F}{2\mathcal{A}} - \frac{F}{2} - \frac{Fl(1-\mathcal{A}^l)}{2(1+\mathcal{A}^l)} + \frac{Fl(1-\mathcal{A}^l)}{2\mathcal{A}(1+\mathcal{A}^l)}.$$

Hence, one obtains $\partial_t \omega(l,t) > 0$, if

$$-\frac{1}{\mathcal{A}} - 1 - l\frac{1-\mathcal{A}^l}{1+\mathcal{A}^l} + \frac{l}{\mathcal{A}}\frac{1-\mathcal{A}^l}{1+\mathcal{A}^l} > 0$$

holds, which is the case, if $\mathcal{A}$ (i.e. the island) is sufficiently small and the wavenumber $l \geq 2$ sufficiently large. For moderate values of $k_\pm$ and μ and for F/D sufficiently large, one can, therefore, expect unstable behaviour of sufficiently small islands. Here, we choose

$$k_+ = 10; \quad k_- = 1; \quad F = 1; \quad D = 1; \quad \mu = 0.05.$$

In addition, we have used $\varepsilon = 0.025$, $R_\infty = 5$ and the initial condition

$$\phi(x,0) = \frac{1}{2}\left(1 - \tanh\left(\frac{3\left(|x| - \tilde{R}\right)}{\varepsilon}\right)\right)$$

with $R_0 = 1$, $A_0 = 0.025$ and an unstable wavenumber $l = 6$. This leads to the numerical results of the viscous Cahn-Hilliard equation in Figure 2.22 showing the level sets $\{\phi = 1/2\}$ at different times. Thereby, one observes an unstable behaviour

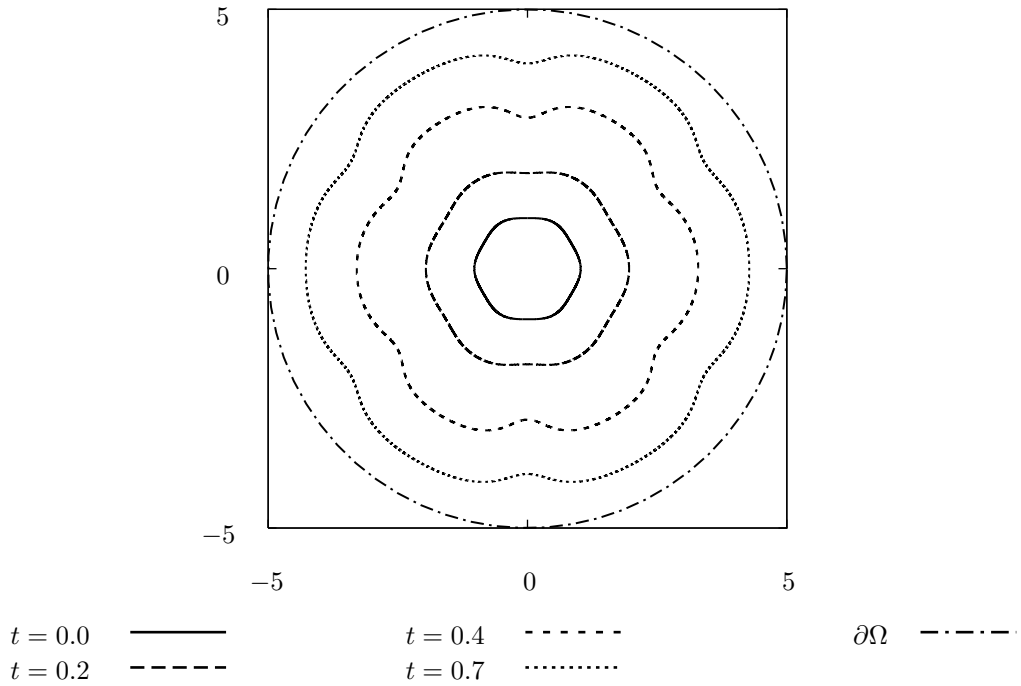

Figure 2.22: Unstable growth of perturbed circular island.

at the beginning and a stabilization starting, when the island is sufficiently large,

which corresponds to the fact that $\partial_t \omega(l,t) < 0$ holds for any wavenumber l and for islands satisfying

$$\mathcal{A}(t) \geq k_+/(k_+ + k_-)$$

as shown in [LRV04]. However, a quantitative comparison of the numerical approach with the dispersion relation (2.113) is difficult due to the facts that the diffuse-interface simulation is behind the actual solution as stated in the previous section and that for $t = t_\infty$ the island vanishes (see also Figure 2.23 for a comparison of

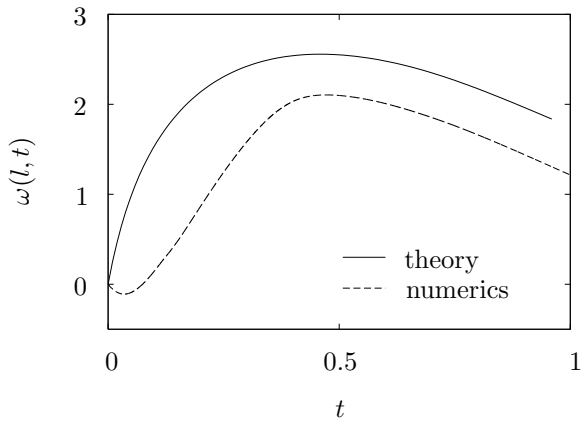

Figure 2.23: Comparison of theoretical and numerical growth rate.

the growth rate determined by numerical integration (with Mathematica [Wol01]) of (2.113) with the one obtained by numerical treatment of the viscous Cahn-Hilliard equation).

2.3.4 Anisotropic Island Growth

Here, we will concentrate on the case of kinetic boundary conditions and present results similar to those obtained in [HV05b] by sharp-interface simulations with edge diffusion included, which is not incorporated into the diffuse-interface model in the case of kinetic boundary conditions. In the numerical results presented in this section, we consider anisotropies in the attachment/detachment rates k_- and k_+ and in the step free energy density φ, which is proportional to the anisotropy function γ. Note that for the viscous Cahn-Hilliard equation (2.26)–(2.28) this also yields an angle dependence for the mobility M_ε and the kinetic coefficient $\tilde{k}$ due to (2.32) and (2.93).

We have used the anisotropy function

$$\gamma(\theta) = 1 + a_\gamma \cos(k_\gamma \theta)$$

with $k_\gamma = 6$ and $a_\gamma = 0.028$ (see Figure 2.24 for polar plot parametrized by

$$\left\{ \gamma(\theta) \begin{pmatrix} \cos(\theta) \\ \sin(\theta) \end{pmatrix} \ : \ \theta \in [0, 2\pi) \right\}$$

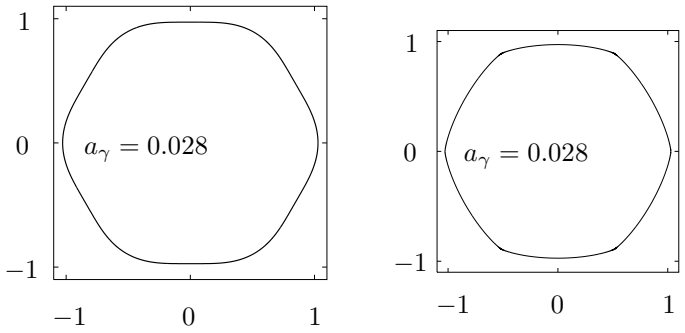

Figure 2.24: Polar plot of anisotropy function γ (left); Wulff shape $\mathcal{W}_\gamma$ corresponding to γ (right).

and corresponding Wulff shape $\mathcal{W}_\gamma$ (defined in (2.4) and (2.3)) and (2.35) for the definition of the angle). This choice yields that γ has a sixfold symmetry and is convex, i.e. $\gamma + \gamma'' > 0$, and, therefore, the viscous Cahn Hilliard equation is parabolic. A parametrization for the Wulff shape $\mathcal{W}_\gamma$ is given by (see [POMZ99])

$$\mathcal{W}_\gamma = \left\{ c(\vartheta) = \gamma(\vartheta)\hat{n}(\vartheta) + \gamma'(\vartheta)\hat{\tau}(\vartheta) \ : \ \vartheta \in [0, 2\pi) \right\},$$

where

$$\hat{n}(\vartheta) := \begin{pmatrix} \cos(\vartheta) \\ \sin(\vartheta) \end{pmatrix} \quad \text{and} \quad \hat{\tau}(\vartheta) := \begin{pmatrix} -\sin(\vartheta) \\ \cos(\vartheta) \end{pmatrix}.$$

This parametrization has been used for the plot in Figure 2.24.

For a comparison of a Wulff shape obtained by a numerical investigation of a viscous Cahn-Hilliard equation with the one with the same enclosed area obtained by theoretical considerations in Figure 2.25, we have started the diffuse-interface approximation with a circular island, i.e. with the initial condition (2.112) with $R_0 = 2$, and let the model find its stationary solution (with $F = 0$). The solid line in Figure 2.25 then shows the level set $\{\phi = 1/2\}$, whereas the points are obtained by theory, which demonstrates the applicability of the diffuse-interface approximation in this anisotropic situation. For the theoretical Wulff shape we chose a parameter $\lambda \in \mathbb{R}$ such that the enclosed area of the curve

$$\lambda(\gamma(\vartheta)\hat{n}(\vartheta) + \gamma'(\vartheta)\hat{\tau}(\vartheta)), \quad \vartheta \in [0, 2\pi)$$

is the same as the area of the level set of the stationary solution of the viscous Cahn-Hilliard equation.

Next, we want to study the growth of an island initially given by the Wulff shape in Figure 2.25. Thus, we start the phase-field simulation with a smeared out height function given by a stationary solution of the viscous Cahn-Hilliard equation obtained by the procedure just mentioned. For this purpose, we introduce kinetic coefficients with a threefold symmetry (see Figure 2.26)

$$k_-(\theta) = k_+(\theta) = a_- k_0(\theta) = a_+ k_0(\theta) = a_\pm \frac{1 + a_k \cos^2(k_k \frac{\theta}{2} - \beta)}{1 + a_k}$$

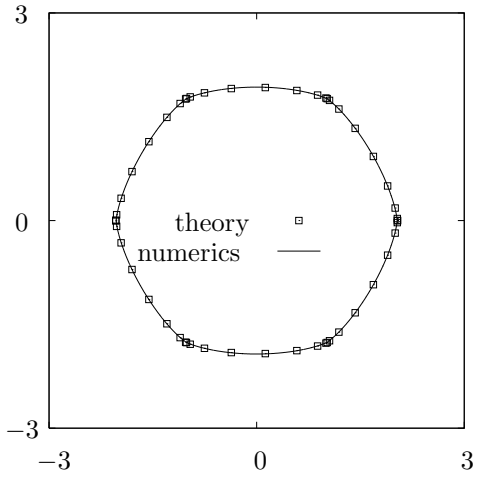

Figure 2.25: Comparison of numerically by diffuse-interface approach determined Wulff shape (solid line) with theoretically determined Wulff shape of same enclosed area (points).

with $k_k = 3$, $\beta = \frac{3\pi}{4}$, $a_\pm = 10$ and different values of a_k. Thereby, we use a set

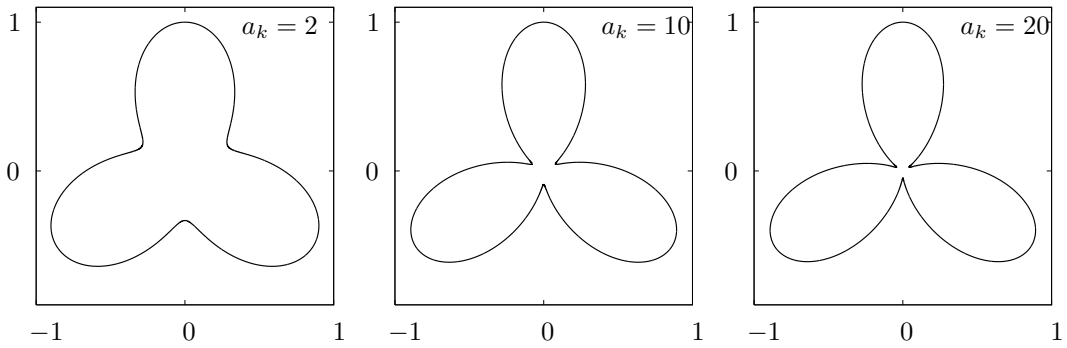

Figure 2.26: Polar plots of anisotropy function k_0 for different values of a_k.

of parameters similar to the one used for the simulation of the growth of circular shaped islands in the isotropic situation in Section 2.3.2

$$F = 0.1; \quad D = 10; \quad \tau^{-1} = 0; \quad \mu_0 = 0.1; \quad \varepsilon = 0.1.$$

In Figure 2.27, one can see the results of phase-field simulations for different values of a_k at corresponding time steps. To be more precise, one has in each picture of Figure 2.27 the level sets $\{\phi = 1/2\}$ at different time steps, i.e. the growth of an island starting with a Wulff shape corresponding to the step free energy. The first picture shows the evolution in the case of isotropic attachment rates, whereas the following examples show the formation of more and more triangular and facetted shapes for increasing values of a_k.

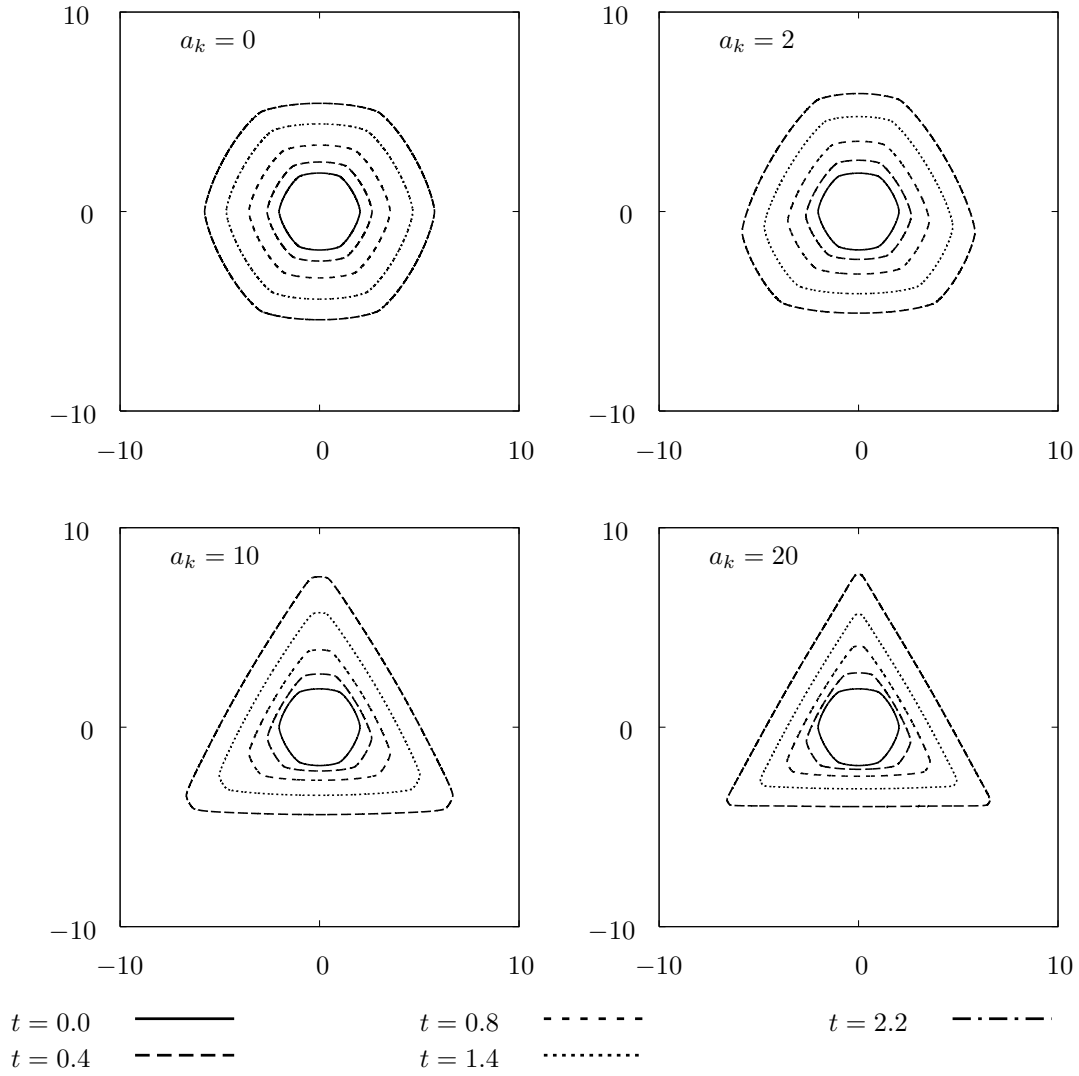

Figure 2.27: Anisotropic growth of initially "Wulff shaped" islands for different strengths of anisotropic attachment rates, i.e. for different values of a_k.

Further examples of Wulff shapes (including 2-dimensional shapes) are shown in Section 3.2.

2.3.5 Spiral Growth

Here, we are concerned with a slightly different application of the diffuse-interface approximation of the BCF model. Following [KP98], we introduce a phase-field model for the simulation of spiral growth.

Phase-field Model in Spiral Growth

Before the details of the model and the numerical results are presented, a few ideas of the physics behind spiral growth are shown. The origin of a growth spiral is a screw dislocation (see Figure 2.28 for a schematic picture). Due to a pinning of the singularity of the screw dislocation, one can observe a spiral shaped step formation, which makes the BCF model applicable. This application has already been a topic in the original work [BCF51].

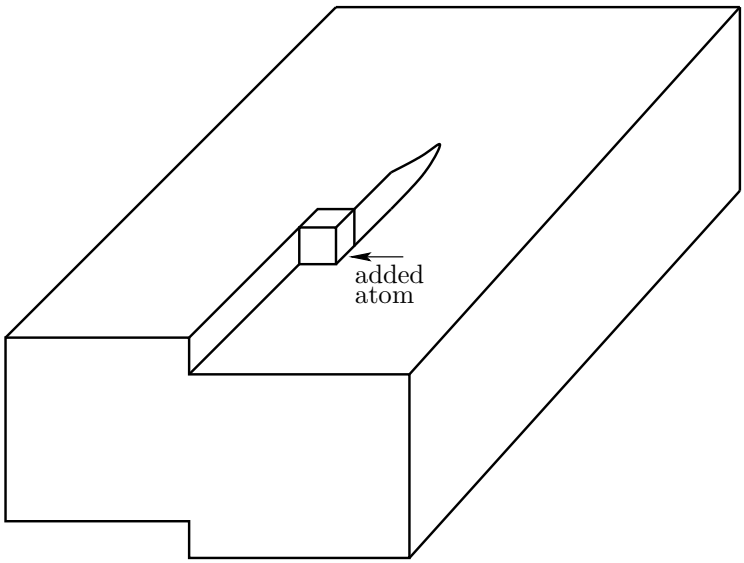

Figure 2.28: Schematic picture of screw dislocation.

Let $\theta := \theta(x) : \mathbb{R}^2 \setminus \{0\} \to [0, 2\pi)$ denote the function returning the angle the point $x = (x_1, x_2)$ makes with the positive x_1-axis (see (2.35)). Then, for the diffuse-interface approximation of the BCF model, the basic idea is to model the screw dislocation by the function $\phi_s : \Omega \to [0, 1)$ as

$$\phi_s(x) := \begin{cases} \frac{1}{2\pi}\theta(x) & \text{for } x \neq 0, \\ 0 & \text{for } x = 0, \end{cases}$$

where we consider the domain $\Omega = (-L/2, L/2)^2$ for some $L > 0$. The height field of ϕ_s is shown in Figure 2.29 (top left) showing the singularity in $x = 0$. Then, following [KP98], we modify the viscous Cahn-Hilliard equation (2.26)–(2.28) for the application in spiral growth, where we restrict ourselves to the isotropic situation. By adding $\partial_t w$ to (2.26), we then obtain the phase-field model

$$\partial_t \phi + \partial_t w + \nabla \cdot j = F - \tau^{-1} w \tag{2.114}$$

$$j = -M_\varepsilon(\phi - \phi_s)\nabla w \tag{2.115}$$

$$\varepsilon k^{-1} \partial_t \phi = \mu \left(\varepsilon \Delta \phi - \varepsilon^{-1} \frac{\partial G}{\partial \phi}(\phi - \phi_s) \right) + g(\phi - \phi_s) w, \tag{2.116}$$

where the multi well potential G as well as the mobility function M_ε have been shifted by the above defined function ϕ_s. In addition, for the case of thermodynamic boundary conditions we have replaced in (2.116) w by $g(\phi-\phi_s)w$ with a stabilizing function $g(\phi) = 30\phi^2(1-\phi)^2$ for $\phi \in [0,1]$ and periodically extended to all $\phi \in \mathbb{R}$ which has been used in order to enforce the phase-field variable to stay in the phases (given by the relation $\phi(x,t)-\phi_s(x) \in \mathbb{Z}$) outside the diffuse interface region without changing the asymptotics for $\varepsilon \to 0$. However, this stabilization is not possible for a proper approximation of the BCF model with kinetic boundary conditions. For the application in spiral growth, the interface or step $\Gamma = \Gamma(t)$ is now given by

$$\Gamma(t) = \left\{ x \in \Omega \ : \ \phi(x,t) - \phi_s(x) - \frac{1}{2} \in \mathbb{Z} \right\}.$$

For the case of thermodynamic boundary conditions, the change from the viscous Cahn-Hilliard equation to the phase-field model, thereby, corresponds to the change from the quasi-stationary BCF model to the BCF model including the diffusion equation (2.5) for the adatom density (see [RV05] for matched asymptotic expansions). However, for the inclusion of an ES barrier by an asymmetric degenerate mobility function (2.32) the phase-field model does not yield the correct asymptotics as $\varepsilon \to 0$ towards the BCF model with kinetic boundary conditions. Therefore, one interprets the additional term $\partial_t w$ as a numerical regularization and ensures by a parameter choice with $\frac{F}{D}$ sufficiently small that the system is in the quasi-stationary regime. In all cases, we have assumed the initial condition $w(x,0) = 0$.

For all computations in this section, we have used uniform grids, and the derivative of the multi well potential has explicitly been treated in contrast to the previous cases, where we have used the linearization (2.103).

Numerical Results (TBC)

First, we present numerical investigations of spiral growth for the case of thermodynamic boundary conditions (TBC) (see also [KP98, BCE$^+$06]), where we have used the following set of parameters:

$$D = 10; \quad \mu = 0.1; \quad \tau^{-1} = 0; \quad k^{-1} = 0.1; \quad \varepsilon = 1,$$

where we first exclude edge diffusion by setting $\nu = 0$. As a first numerical example, one can see in Figure 2.29 profiles (shifted to the same height) of the smeared out height function ϕ at different times. In addition, Figure 2.30 showing cross sections of profiles of ϕ at different time steps further illustrates the shape of the spirals. Thereby, starting with a screw dislocation given by the function ϕ_s, one obtains after deposition of 20 monolayers the formation of a spiral, and after deposition of a sufficient number of monolayers, one notices a constant step spacing and a periodic growth, where after deposition of one monolayer one gets the same shape shifted by height 1 (see also [KP98]). In the following, the above mentioned stepspacing will be denoted by l. Then, one can investigate the dependency of the stepspacing on

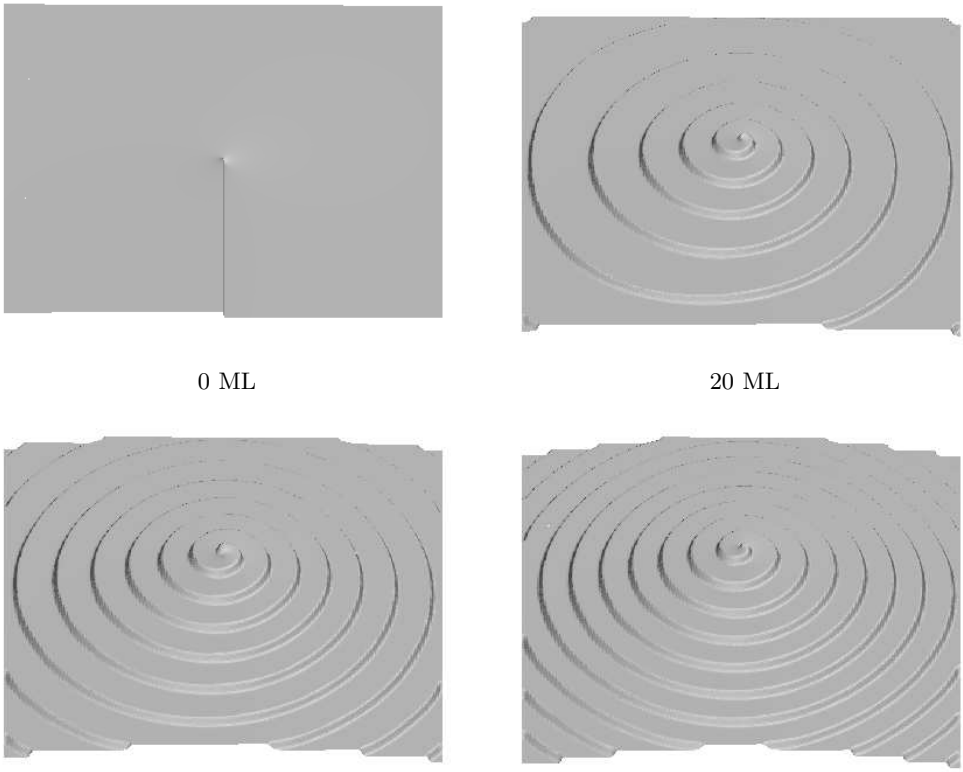

Figure 2.29: Profiles of smeared height function ϕ after growth of different numbers of monolayers (ML) with $F = 0.2$, $\nu = 0$ and $L = 100$ (TBC).

the deposition flux F. In [KP98], theoretical considerations lead to the relation

$$19\mu = \frac{Fl^3}{4D}\left(1 + \frac{4D}{kl}\right). \tag{2.117}$$

Tab. 2.2 shows a comparison of the physical relevant solution of the cubic equation (2.117) with numerically determined values of l illustrating the dependency of l on F and a deviation of the numerical results (with $L = 0$) from the theoretically predicted of less than 10%.

deposition flux F	0.2	0.1	0.05	0.025
step spacing l theory	6.1	8.0	10.3	13.3
step spacing l numerics	6.7	8.7	11.3	14.4

Table 2.2: Step spacing l versus deposition flux F.

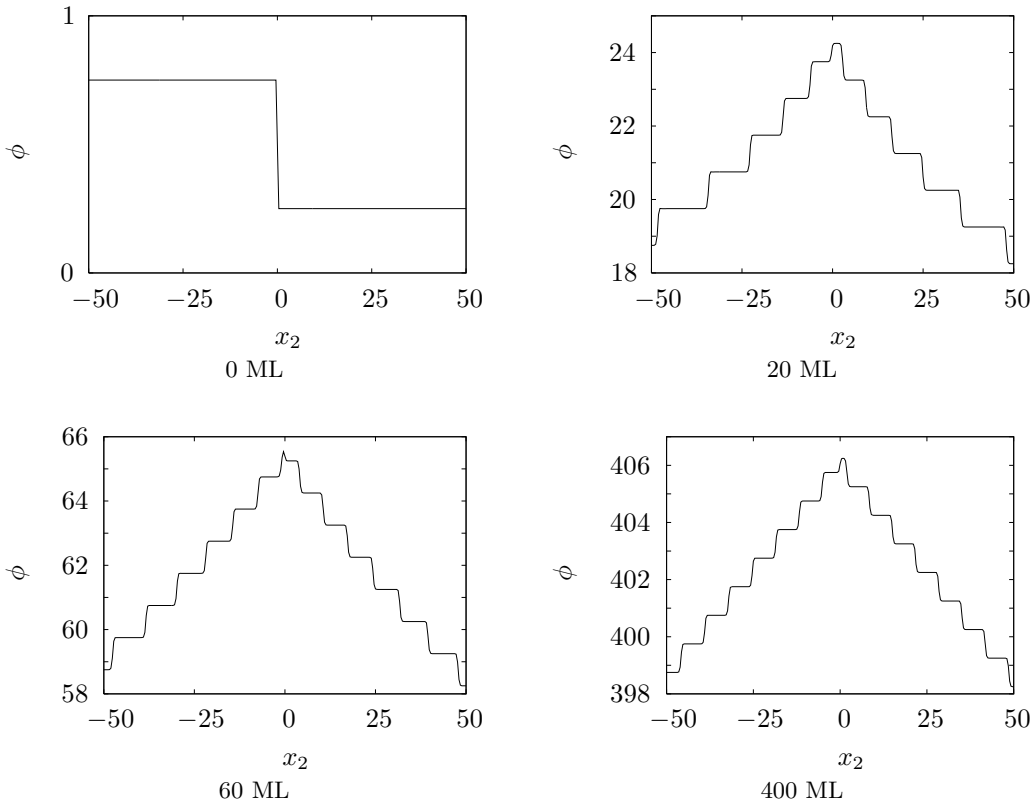

Figure 2.30: Cross sections ($x_1 = 0$) of profiles of smeared height function ϕ after growth of different numbers of monolayers (ML) with $F = 0.2$, $\nu = 0$ and $L = 100$ (TBC).

As a second interesting property of the film, we consider the surface width

$$W = W(t) = \frac{1}{2}\left(\frac{1}{|\Omega|}\int_\Omega \left(\phi^2 - \left(\bar{\phi}\right)^2\right)\, dx\right)^{1/2},$$

which is a measure for the roughness of the film (see e.g. [MK04, KP98]). One obtains

$$W(t \to \infty) \sim \frac{L}{l}.$$

Plotting $W(t)/(L/l)$ versus $Ft/(L/l)^3$ (see Figure 2.31 and [KP98]) for fixed $F = 0.1$, one can see that the data collapse, from which one concludes that the time to reach steady state scales as $(L/l)^3$, which can be confirmed by theoretical considerations [KP98].

Further numerical investigations deal with the incorporation of edge diffusion into the model corresponding to the case $\nu \neq 0$. In Figure 2.32, cross sections of height profiles with ($\nu = 100$) and without ($\nu = 0$) edge diffusion are presented, where we have used $L = 100$ and $F = 0.2$. These show that for $\nu = 100$ the

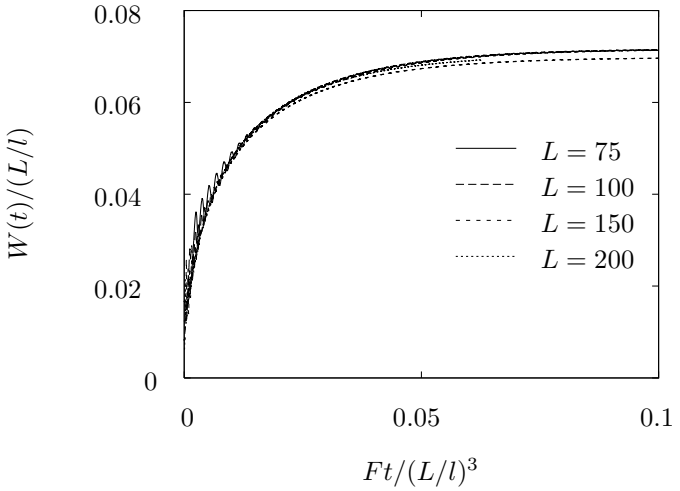

Figure 2.31: Rescaled surface width as a function of rescaled time for different edge lengths L of the domains $\Omega = (-L/2, L/2)^2$ and for $F = 0.1$ (TBC).

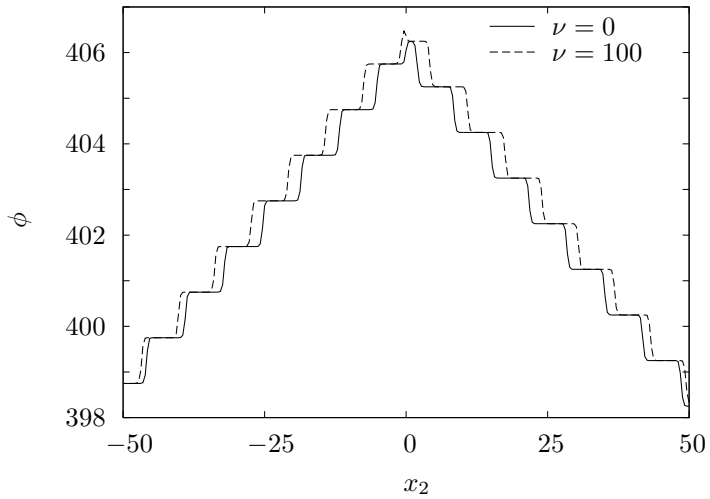

Figure 2.32: Cross sections of profile of smeared out height function with ($\nu = 100$) and without ($\nu = 0$) edge diffusion after deposition of 400 ML (TBC).

stepspacing is not constant. In the lower part of the spiral it is decreased compared to the example with $\nu = 0$, while in the upper part the stepspacing is the same with and without edge diffusion. Thus, the decrease in the lower part of the spiral leads to a steepening in this part, which is also displayed in the surface width plotted in Figure 2.33 for different edge mobilities ν, where one can see an increase of the surface width for increasing values of ν. However, these plots suggest that there exists a limit of the curves $W = W(t)$ as $\nu \to \infty$.

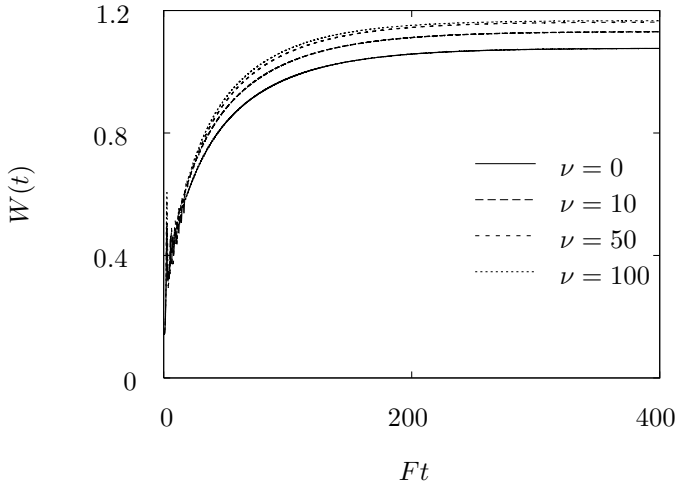

Figure 2.33: Surface width as a function of rescaled time for different values of edge mobility ν (TBC).

Numerical Results (KBC)

As a last example, we study the influence of the ES barrier, which is modelled in the diffuse-interface approach by the asymmetric mobility function (2.32). Here, we consider the domain $\Omega = (-L, L)^2$ with $L = 75$ and the attachment rates $k_+ = 10$ and $k_- = 1$ as well as the deposition flux rate $F = 0.1$. In Figure 2.34, one can see the smeared out height function ϕ at different time steps. These pictures and the cross sections shown in Figure 2.35 demonstrate that a remarkable steepening occurs in the case of kinetic boundary conditions, which yield a behaviour completely different from the case of thermodynamic boundary conditions (see Figure 2.29 and Figure 2.30). One also observes that there is a plateau-like part on the top of the spiral with a larger stepspacing. The steepening below this plateau is similar to results known for the growth of so-called wedding cakes, where the film grows due to nucleation of new islands on the top of the top island (see e.g. [MK04]). However, there is a limitation to the steepening in the diffuse-interface model due to the finite value of the diffuse interface width. This results in a maximal slope at the side of the spiral.

By defining $g \equiv 1$ one can reformulate (2.116) as

$$\varepsilon k^{-1} \partial_t \phi = -\mu \frac{\delta \mathcal{E}}{\delta \phi}$$

with a changed free energy

$$\mathcal{E}(\phi) = \int_\Omega \left(\varepsilon \frac{1}{2} |\nabla \phi|^2 + \varepsilon^{-1} G(\phi - \phi_s) - \mu^{-1} \phi w \right) \mathrm{d}x.$$

Thus, one can interpret the term $-\mu^{-1}\phi w$ as a reduction of the energy-barrier between two terrace heights. Consequently, for moderate values of ε and sufficiently

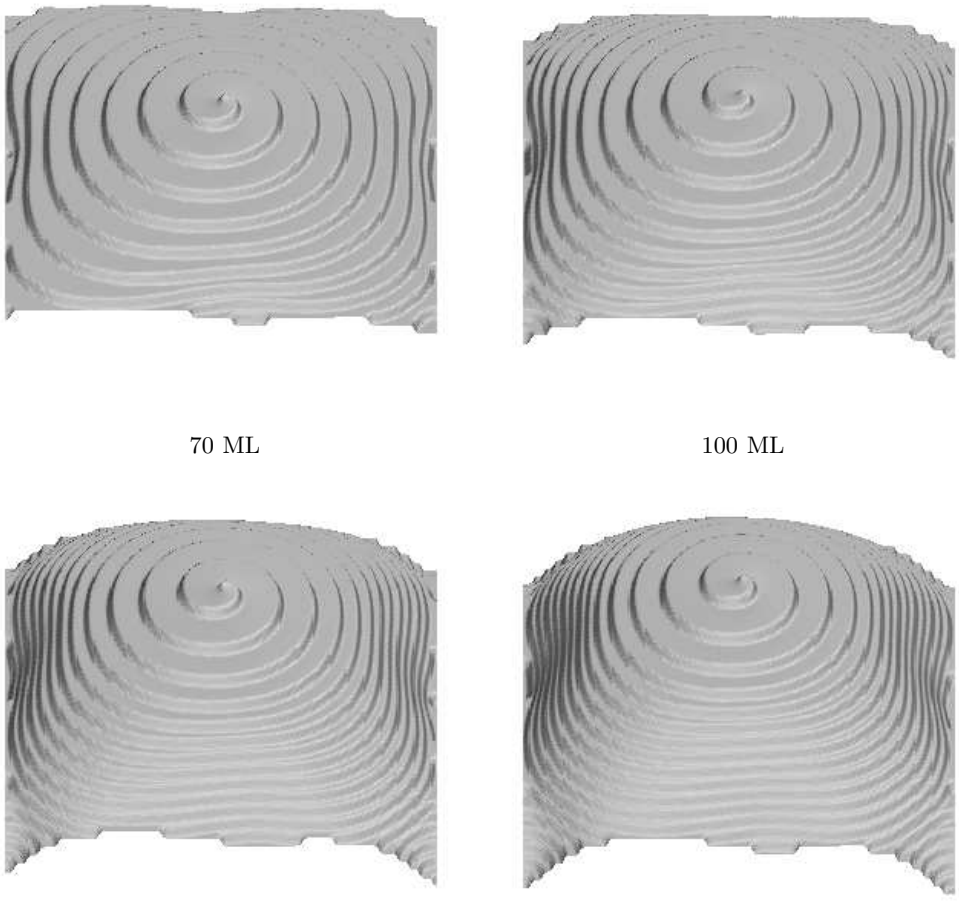

Figure 2.34: Profiles of smeared height function ϕ after growth of different numbers of monolayers (ML) with $F = 0.1$, $L = 75$ (KBC).

small step stiffness, the diffuse-interface model contains a nucleation, which can be seen in Figure 2.36, where we have a growth spiral in the centre of the domain surrounded by several mounds formed due to nucleation. Again, one can see a plateau on the top of the spiral and steepening in the lower part. Furthermore, one recognizes that the height of the spiral is larger compared to the height of the mounds surrounding it. However, a quantitative justification of the nucleation contained in this model has not been given yet. Although it does not contain stochastic aspects of a nucleation theory, it is in so far reasonable as nucleation occurs, where the adatom concentration is sufficiently large. At least, one gets realistic boundary conditions for the spiral in this way.

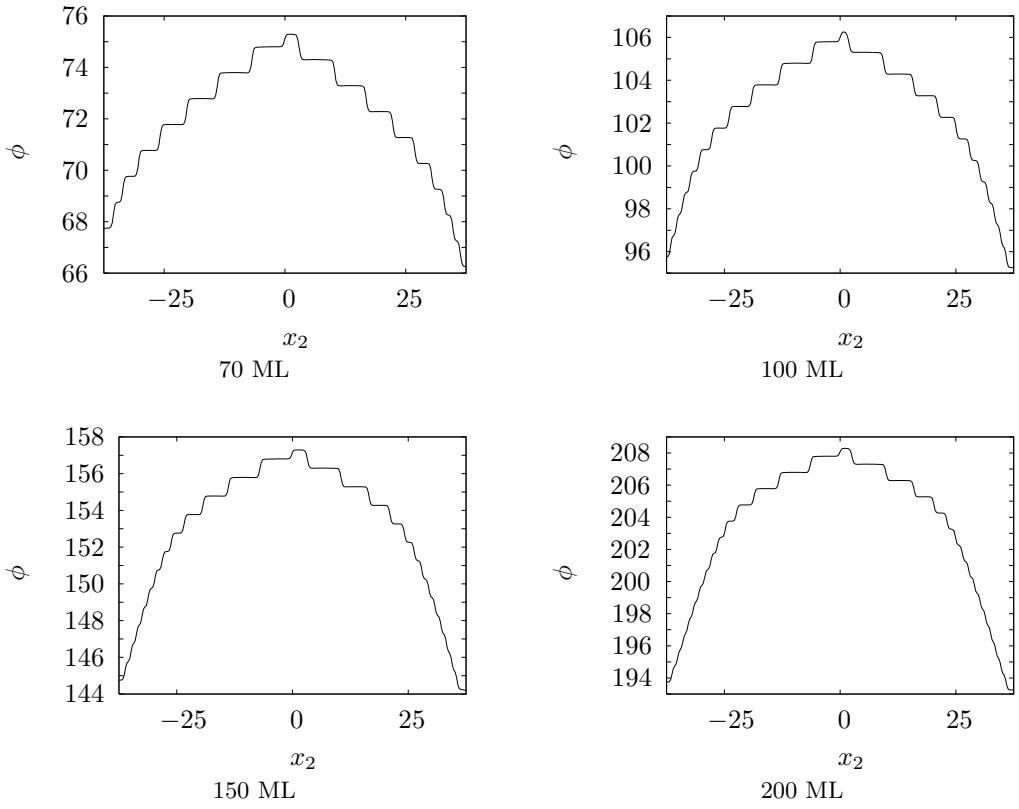

Figure 2.35: Cross sections ($x_1 = 0$) of profiles of smeared height function ϕ after growth of different numbers of monolayers (ML) with $F = 0.1$, $L = 75$ (KBC).

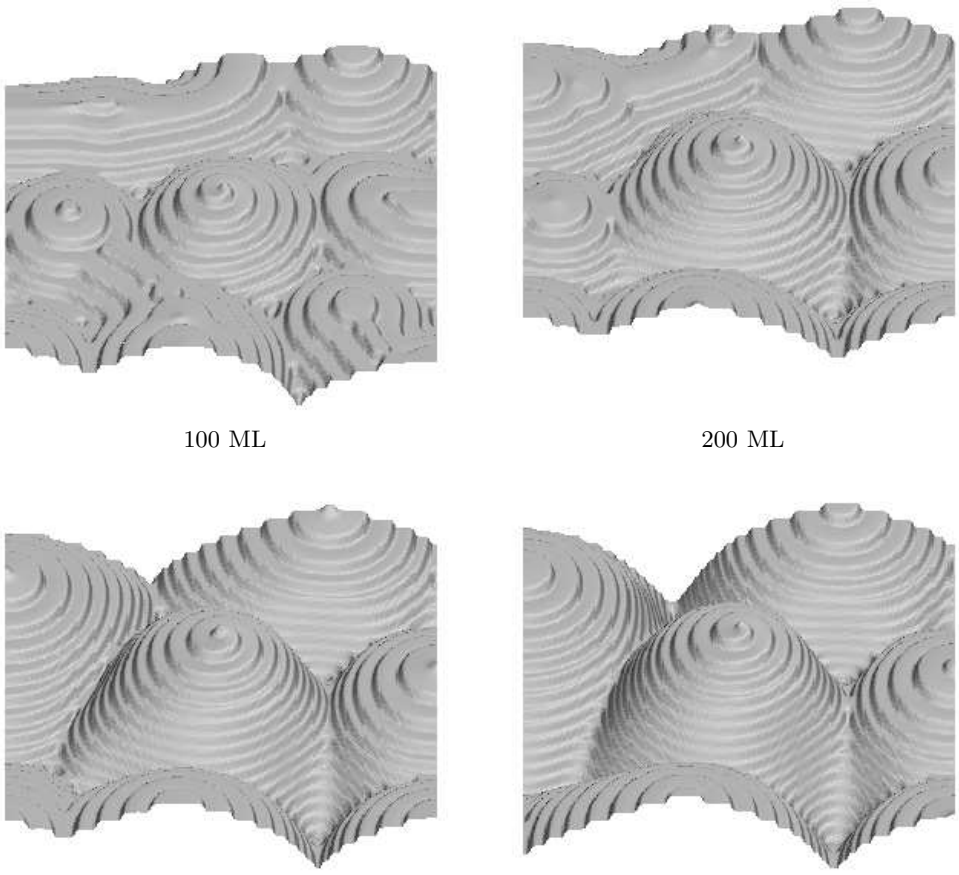

100 ML 200 ML

300 ML 400 ML

Figure 2.36: Profiles of smeared height function ϕ after growth of different numbers of monolayers (ML) with $F = 0.1$, $L = 75$ and $\mu = 0.025$ (KBC).

Chapter 3

Diffuse-Interface Approximation of Continuous Surface Models

In contrast to Chapter 2, we consider here epitaxial growth on a more coarse grained level. That means, we study the vapour-solid-interface of a film grown from the vapour onto a substrate on a continuum level. Starting from Mullins' work [Mul57] there has been a large interest in such continuum descriptions (see e.g. [CT94, GJ02]). Here, we concentrate on the homoepitaxial case, i.e. in principle, we neglect elastic energies resulting from a lattice mismatch between film and substrate in the case of heteroepitaxial growth, where the so-called Asaro-Tiller-Grinfeld (ATG) instability [AT72, Gri86, Sro89] may lead to a breakup of an unstable film into islands [GN99]. Following [CENC96, TC94], we will investigate a diffuse-interface approximation of motion by surface diffusion. In Section 3.1, we describe the sharp- and diffuse-interface model, which will be of interest here. Afterwards, in Section 3.2, we briefly discuss the numerical algorithm used in this case, which is nearly the same as the one presented in Section 2.3. As a numerical test case, we introduce in one dimension an artificial elastic energy density depending only on the film height in order to quantitatively reproduce a theoretically predicted instability. Afterwards, we investigate the smoothing property of the model in different one dimensional isotropic situations, before, for two dimensional surfaces, the evolution of initially prism-shaped surfaces is studied, where a pinch-off numerically predicted in [BMN05] by sharp-interface simulations is reproduced by a diffuse-interface approximation. Furthermore, we will investigate closed equilibrium shapes for anisotropic free energy densities and the behaviour under growth, if an additional anisotropy in the attachment is included.

Numerical investigations of elastically stressed films can be found in [ZB99, ZBL03, RS04] with a sharp-interface method and [EV02, WLKJ04, RRV06] using diffuse-interface approximations, and, in $1+1$ dimensions, approaches towards a continuum description derived from a step flow perspective have been performed by [Xia02, XE04, SF02], for example.

3.1 Model Description

In the following, a sharp-interface model similar to the one proposed by Cahn and Taylor [CT94] is described, before we introduce a diffuse-interface approximation based on the works [CENC96, TC94].

3.1.1 Sharp-Interface Model

The principle physical scenario we want to consider here is a film grown from the vapour onto a solid substrate (see Figure 3.1 for a simple discrete picture in one dimension).

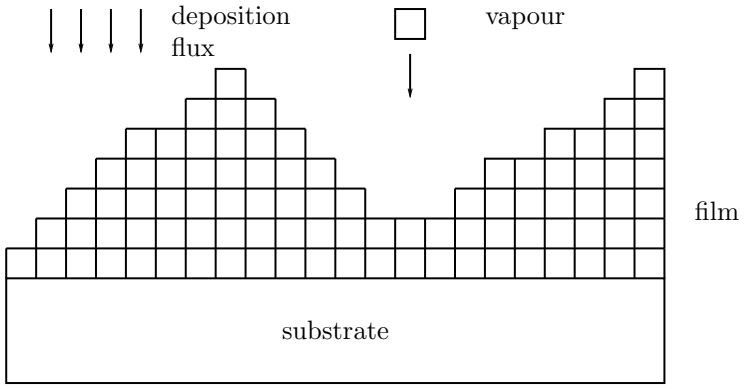

Figure 3.1: Schematic picture of a film grown from the vapour onto a substrate.

Geometric Objects and Quantities

However, here we concentrate on a continuum description of the above situation (see Figure 3.2), where the interface between the vapour and the solid is given by smooth $(d-1)$-dimensional orientable surface $\Gamma = \Gamma(t) \subset \Omega \subset \mathbb{R}^d$ evolving during a time interval $t \in [t_0, t_{\text{end}}]$, where we assume $\Gamma(t_0) = \Gamma_0$ as an initial condition for a given $(d-1)$-dimensional surface $\Gamma_0 \subset \mathbb{R}^d$. Thus, $\Gamma(t)$ separates Ω into two domains $\Omega_1(t)$ and $\Omega_0(t)$ satisfying $\overline{\Omega_1(t)} \cup \overline{\Omega_0(t)} = \overline{\Omega}$ and $\overline{\Omega_1(t)} \cap \overline{\Omega_0(t)} = \Gamma(t)$ and representing the two phases solid and vapour. The evolution of Γ can, therefore, also be displayed by the characteristic function $\phi_0 : \Omega \times [t_0, t_{\text{end}}] \to \mathbb{R}$, $\phi_0 = \chi_{\Omega_1}$ of Ω_1. Let $X(t, \cdot) : \Gamma(t) \to \mathbb{R}^d$, $t \in [t_0, t_{\text{end}}]$ be an immersion. Then, we define the basic geometric properties of Γ by denoting the normal pointing from the solid phase to the vapour phase with $N = N(t)$ and defining the normal velocity $v := \partial_t X \cdot N$. Furthermore, we consider the mean curvature

$$H = \sum_{i=1}^{d-1} \kappa_i$$

of Γ with the principal curvatures κ_i, where we assume the sign convention similar to the one in Chapter 2 (see Figure 2.2) stating that, if Γ is a closed surface with

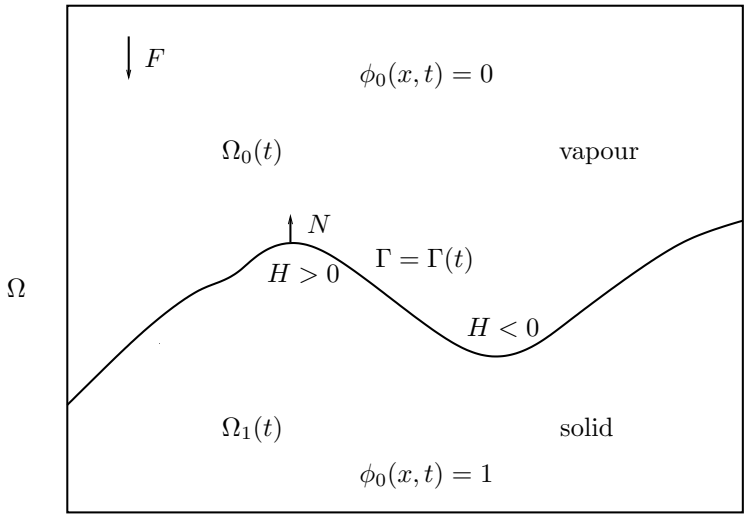

Figure 3.2: Continuous picture of a film; sign convention.

$\Gamma = \partial\Omega_1$, the mean curvature H is positive, if Ω_1 is convex. In addition, we assume that $H > 0$ holds, if Γ is given by the graph of a concave function with Ω_1 below Γ (see Figure 3.2). With ∇_Γ and Δ_Γ, we denote the surface gradient and the Laplace-Beltrami operator on Γ, respectively, whereas $\nabla_\Gamma \cdot Y$ is defined as the divergence of a vector field Y on Γ. Moreover, we have the induced metric $\langle \cdot, \cdot \rangle_\Gamma$ for vector fields $V, W \in T\Gamma$ given by

$$\langle V, W \rangle_\Gamma := DX(V) \cdot DX(W).$$

Surface Free Energy

Similar to the situation in Section 2.1.1, where we studied the free energy of a step, we consider here the surface free energy

$$\mathcal{S}_\varphi(\Gamma) := \int_\Gamma \varphi(N) \, \mathrm{d}A \tag{3.1}$$

including the $(d-1)$-dimensional Hausdorff measure $\mathrm{d}A = \mathrm{d}\mathcal{H}^{d-1}$ and a free energy density $\varphi = \mu_2 \gamma$, where $\mu_2 > 0$ is a constant dimensional quantity and $\gamma : \mathrm{S}^{d-1} \to \mathbb{R}$ a positive dimensionless anisotropy function. Furthermore, we assume that the one-homogeneous extension of γ defined by

$$\bar{\gamma}(p) := \begin{cases} |p| \gamma\left(\frac{p}{|p|}\right) & \text{for} \quad p \in \mathbb{R}^d \setminus \{0\}, \\ 0 \quad \text{for} \quad p = 0 \end{cases}$$

is a convex function and $\bar{\gamma} \in \mathrm{C}^2(\mathbb{R}^d \setminus \{0\})$. If one considers then the variational problem

$$\text{Minimize} \quad \mathcal{S}_\gamma(\Gamma) = \int_\Gamma \gamma(N) \, \mathrm{d}A \quad \text{such that} \quad |\Omega| = \text{constant} \tag{3.2}$$

with $\Omega \subset \mathbb{R}^d$ a smooth domain satisfying $\partial\Omega = \Gamma$, one obtains that the Wulff set

$$W_\gamma := \left\{ x \in \mathbb{R}^d \,:\, x \cdot n \leq \gamma(n) \; \forall n \in \mathrm{S}^{d-1} \right\}$$

is a solution of (3.2) (see [Tay78]), and one defines the Wulff shape $\mathcal{W}_\gamma := \partial W_\gamma$.

Weighted Mean Curvature

In order to state the result of the variational derivative $\frac{\delta \mathcal{S}_\gamma}{\delta \Gamma}$, we define the divergence of a non-tangential vector field (see [Cla02, CvdM01]).

Definition 1. *The divergence of a non-tangential vector field $Z : \Gamma \to \mathbb{R}^d$ on Γ given by an immersion $X : \Gamma \to \mathbb{R}^d$ is defined as*

$$\nabla_\Gamma \cdot Z := \operatorname{tr}\left((DX)^{-1} DZ(\cdot)^{\tan} \right), \tag{3.3}$$

where $DX(p) : T_p\Gamma \to [N(p)]^\perp$ and $DZ(p)^{\tan} : T_p\Gamma \to [N(p)]^\perp$, and $\eta^{\tan} := (\mathrm{Id} - N \otimes N)\eta$ denotes the tangential part of $\eta \in \mathbb{R}^d$ in $[N(p)]^\perp$ with $[N(p)]^\perp := \{y \in \mathbb{R}^d : y \cdot N(p) = 0\}$.

With this definition in mind, we now present the result of the computation of the variational derivative $\frac{\delta \mathcal{S}_\gamma}{\delta \Gamma}$ in

Lemma 2. *Let $\Gamma \subset \mathbb{R}^d$ be a compact hypersurface of dimension $d-1$ given by an immersion $X : \Gamma \to \mathbb{R}^d$ of class C^2 with normal N. For a smooth mapping $\Psi : \Gamma \to \mathbb{R}^d$, one gets the first variation*

$$\delta \mathcal{S}_\gamma(X, \Psi) := \frac{\mathrm{d}}{\mathrm{d}\varepsilon} \mathcal{S}_\gamma(X + \varepsilon\Psi)\big|_{\varepsilon=0} = \int_\Gamma \nabla_\Gamma \cdot (D\bar{\gamma}(N))N \cdot \Psi \, \mathrm{d}A \tag{3.4}$$

or, in other words,

$$\frac{\delta \mathcal{S}_\gamma}{\delta \Gamma} = \nabla_\Gamma \cdot (D\bar{\gamma}(N))N$$

and, therefore, one obtains for the weighted mean curvature

$$H_\gamma := \frac{\delta \mathcal{S}_\gamma}{\delta \Gamma} \cdot N = \nabla_\Gamma \cdot (D\bar{\gamma}(N)).$$

For a proof, we refer to [Cla02, CvdM01]. Thus, one obtains for surfaces of fixed enclosed volume an equilibrium condition stating that the weighted mean curvature is constant. Furthermore, in an isotropic case $\gamma = 1$, one has

$$H_\gamma = \nabla_\Gamma \cdot N = H.$$

Surface Diffusion and Interface Kinetics

Now, following [Mul57] and [CT94], we establish a model for surface diffusion in this situation. For this purpose, we first define the surface flux

$$J := -\nu\tilde{\Omega}\nabla_\Gamma w \tag{3.5}$$

with the positive mobility $\nu = \nu(N)$ and the potential w which will later be determined. Then, we assume the mass/volume preserving law for the normal velocity

$$v = -\nabla_\Gamma \cdot J. \tag{3.6}$$

For the chemical potential w, we introduce the equation

$$v = k\left(-\tilde{\Omega}\frac{\delta\mathcal{S}_\varphi}{\delta\Gamma} + w\right), \tag{3.7}$$

with a positive kinetic coefficient $k = k(N)$.

We measure length scales in atomic distances (i.e. $\tilde{\Omega} = 1$), energies in units of $k_B\Theta$ and consider non-dimensional times (cf. Section 2.1.1), and we rewrite system (3.5)–(3.7) as

$$v = -\nabla_\Gamma \cdot J, \tag{3.8}$$

$$J = -\nu\nabla_\Gamma w, \tag{3.9}$$

$$v = k\left(-H_\varphi + w\right). \tag{3.10}$$

Two Extreme Cases

There are two extreme cases of the system (3.8)–(3.10) which are of special interest. For the first one, we define the weighted mean value

$$\overline{H}_\varphi := \frac{\int_\Gamma kH_\varphi \,\mathrm{d}A}{\int_\Gamma k \,\mathrm{d}A}.$$

Then, for $\nu \to \infty$, the system (3.8)–(3.10) turns into volume preserving weighted mean curvature flow

$$v = -k\left(H_\varphi - \overline{H}_\varphi\right), \tag{3.11}$$

whereas the limit $k \to \infty$ yields the evolution law for classical (anisotropic) motion by surface diffusion

$$v = \nabla_\Gamma \cdot (\nu\nabla_\Gamma H_\varphi). \tag{3.12}$$

Note that in contrast to (3.11) the fourth order equation (3.12) is local. With the two extreme cases of volume preserving weighted mean curvature flow (3.11) and anisotropic surface diffusion (3.12), the system (3.8)–(3.10) can be viewed as an interpolation between these two cases.

Mass Conservation and Energy Dissipation

Now, we want to establish some basic properties of the model (3.8)–(3.10). The first result states volume/mass conservation, whereas the second one states the decrease of the energy $\mathcal{S}_\varphi$ of the surface. To be more precise, we have

Proposition 1. *For a family of hypersurfaces $\Gamma(t) \subset \mathbb{R}^d$ with interior $\Omega_1(t) \subset \mathbb{R}^d$ and without boundary satisfying the evolution law (3.8)–(3.10), we have the following two properties*

$$\frac{\mathrm{d}}{\mathrm{d}t}|\Omega_1(t)| = 0, \tag{3.13}$$

$$\frac{\mathrm{d}}{\mathrm{d}t}\mathcal{S}_\varphi \leq 0. \tag{3.14}$$

The results of Proposition 1 easily follow from

Lemma 3.

$$\frac{\mathrm{d}}{\mathrm{d}t}|\Omega_1(t)| = \int_\Gamma v \,\mathrm{d}A, \tag{3.15}$$

$$\frac{\mathrm{d}}{\mathrm{d}t}\mathcal{S}_\varphi = \int_\Gamma v H_\varphi \,\mathrm{d}A, \tag{3.16}$$

where (3.15) is a consequence of the transport theorem, and a proof of (3.16) can be found in [Law80] in the isotropic and in [DDE05a] in the anisotropic case or can be derived in a similar way as Lemma 2.

Proof of Proposition 1. For the proof of (3.13), we compute

$$\frac{\mathrm{d}}{\mathrm{d}t}|\Omega_1(t)| = \int_\Gamma v \,\mathrm{d}A = -\int_\Gamma \nabla_\Gamma \cdot J \,\mathrm{d}A = \int_\Gamma \langle J, \nabla_\Gamma 1\rangle_\Gamma \,\mathrm{d}A = 0.$$

Now, we prove (3.14).

$$\begin{aligned}\frac{\mathrm{d}}{\mathrm{d}t}\mathcal{S}_\varphi &= \int_\Gamma v H_\varphi \,\mathrm{d}A = \int_\Gamma v\left(w - \frac{1}{k}v\right)\,\mathrm{d}A \\ &= -\int_\Gamma \frac{1}{k}v^2 \,\mathrm{d}A + \int_\Gamma \nabla_\Gamma \cdot (\nu \nabla_\Gamma w)\, w \,\mathrm{d}A \\ &= -\int_\Gamma \frac{1}{k}v^2 \,\mathrm{d}A - \int_\Gamma \langle \nu \nabla_\Gamma w, \nabla_\Gamma w\rangle_\Gamma \,\mathrm{d}A \leq 0,\end{aligned}$$

which completes the proof of Proposition 1.

□

Remark 1. *One could also derive (3.14) by interpreting the evolution law (3.8)–(3.10) as a gradient flow of the energy functional $\mathcal{S}_\varphi$ [TC94].*

Existence results for the system (3.8)–(3.10) are only available for curves ([EG97]). For the non volume preserving isotropic version $v = -H$ of the extreme case (3.11), it could proven that for a smooth, compact and uniformly convex hypersurface $\Gamma_0 \subset \mathbb{R}^d$ there exists a finite time interval $[0, t_1)$ and a solution $\Gamma(t)$ with $t \in [0, t_1)$ and $\Gamma(0) = \Gamma_0$ such that the $\Gamma(t)$ converge to a point as $t \to t_1$, where the according to fixed volume rescaled surface shows a convergence towards a sphere as $t \to t_1$ (see [Hui84] for $d \geq 3$ and [GH86, Gra87] for a stronger result for $d = 2$). In [BMN07], a regularization method for mean curvature flow through higher order equations is established, where the convergence of the regularized problem towards the mean curvature flow for all times before the first singularity could be proven.

For a theoretical treatment in the anisotropic case $v = -H_\varphi$, we refer to [CGG91, Son93, Gag93]. Numerical studies of this model can be found in [DD02] in a graph formulation and in [Dzi99] in a parametric framework, for example. For level set approaches, we refer to [DDE05a] and references therein.

In the isotropic case of the volume preserving version of mean curvature flow (3.11) with $\phi = k = 1$, one was able to show that there exists a smooth solution $\Gamma(t)$ for $t \in [0, \infty)$, if Γ_0 is compact, uniformly convex and smoothly embedded in $\mathbb{R}^d$. Furthermore, $\Gamma(t)$ converges to a round sphere as $t \to \infty$ (see [Hui87] and [ES98] for generalization, if Γ_0 is sufficiently near to a sphere, as well as [Gag86] in the case of curves). Extensions to the anisotropic volume preserving situations can be found in [And01]. Numerical treatment of isotropic volume preserving mean curvature flow can be found in [May00].

In order to allow strong (non-convex) anisotropies in φ, a regularization of the energy

$$\varphi \rightsquigarrow \varphi + \frac{1}{2}\varepsilon_0 H^2, \quad \varepsilon_0 > 0$$

by a Willmore energy term has been proposed in [DGPG92]. The resulting regularized mean curvature flow has numerically been studied in [HV06] by a parametric approach. The regularization, thereby, leads to a smearing out of sharp corners on a length scale of order of ε_0. In a level set description, this has been studied in [BHSV07].

Now, we consider the second extreme case (3.12) of (3.8)–(3.10), where existence results are restricted to the isotropic case (see [EG97] for curves and [EMS98] for surfaces near spheres). A basic property of solutions to (3.12) is that perturbations of a sphere are smoothened. Obviously, spheres are stationary solutions of (3.12).

Numerically, the evolution law (3.12) has been investigated for graphs in [BMN04] in the isotropic case and in [DDE05b] in the anisotropic case. Parametric studies in isotropic situations can be found in [BMN05]. For level set approaches, we refer to [CHR+05] and references therein. Regularized approaches similar to the ones for weighted mean curvature are applied in [HV05a] in the parametric case, in [Bur05] for graphs and in [BHSV07] in a level set framework.

Deposition Flux

Finally, we want to mention that a vector valued deposition flux $F \in \mathbb{R}^d$ can be incorporated into the model (3.8)–(3.10) by adding the term $-F \cdot N$ to (3.8)

$$v = -\nabla_\Gamma \cdot J - F \cdot N, \tag{3.17}$$

where for later applications it is assumed that $F = F(N) \in \mathbb{R}^d$ may depend on the normal of the interface.

3.1.2 Diffuse-Interface Model

In the following, it is assumed that the interface $\Gamma(t) \subset \Omega$ is contained in a fixed domain $\Omega \subset \mathbb{R}^d$ for all times $t \in [t_0, t_{\text{end}}]$. Based on the idea of a degenerate mobility as introduced in [CENC96], Cahn and Taylor proposed in [TC94] for a small parameter $\varepsilon > 0$ and an energy density $E = E(z,p) : Q \subset \mathbb{R} \times \mathbb{R}^d \to \mathbb{R}$ a viscous Cahn-Hilliard equation

$$\partial_t \phi + \nabla \cdot j = 0, \tag{3.18}$$

$$j = -M_\varepsilon \nabla w, \tag{3.19}$$

$$\varepsilon \tilde{k}^{-1} \partial_t \phi = -\mu_2 \frac{\delta \mathcal{E}}{\delta \phi} + g(\phi) w = \mu_2 \left(\nabla \cdot E_p(\phi, \nabla\phi) - \varepsilon^{-1} G'(\phi) \right) + g(\phi) w \tag{3.20}$$

as a diffuse-interface approximation of (3.8)–(3.10) with $\phi, w : \Omega \times [t_0, t_{\text{end}}] \to \mathbb{R}$, $j : \Omega \times [t_0, t_{\text{end}}] \to \mathbb{R}^d$ and an initial condition $\phi(x, t_0) = \tilde{\phi}(x)$ for some $\tilde{\phi} : \Omega \to \mathbb{R}$ obtained by smearing out the discrete function $\phi_0(x, t_0)$ and, therefore, representing the initial surface Γ_0. As in Chapter 2, one additionally assumes Dirichlet or no flux boundary conditions for ϕ and w on $\partial\Omega$, or one assumes Ω-periodicity for ϕ and w or some combination of these boundary conditions on $\partial\Omega$. In this diffuse-interface model, the width of the interface is of order of ε. Similar to the case in Chapter 2 (see (2.24)), we, thereby, use the energy

$$\mathcal{E}(\phi) := \int_\Omega E(\phi, \nabla\phi) \, \mathrm{d}x := \int_\Omega \left(\frac{1}{2} \varepsilon |\gamma \nabla \phi|^2 + \varepsilon^{-1} G(\phi) \right) \, \mathrm{d}x \tag{3.21}$$

with the double well potential

$$G(\phi) = 18\phi^2 (1 - \phi)^2 \tag{3.22}$$

attaining its minimum $G = 0$ in $\phi = 0$ and $\phi = 1$ representing the two phases vapour and solid. Furthermore, the degenerate mobility function M_ε given by

$$M_\varepsilon(\phi) := \varepsilon^{-1} \tilde{\nu}(n(\nabla\phi)) B(\phi) \tag{3.23}$$

with $B(\phi) = 2G(\phi) = 36\phi^2(1-\phi)^2$ restricts diffusion to the interface. Moreover, we define the rescaled diffusion coefficient

$$\tilde{\nu}(n(\nabla\phi)) := \frac{\nu(n(\nabla\phi))}{\gamma(n(\nabla\phi))}. \tag{3.24}$$

Similarly, one introduces the kinetic coefficient

$$\tilde{k}(n(\nabla\phi)) := \frac{k(n(\nabla\phi))}{\gamma(n(\nabla\phi))}, \tag{3.25}$$

for reasons explained in the asymptotic analysis in Section 2.2.1. In this diffuse-interface approach, the interface is given by the level set

$$\Gamma(t;\varepsilon) := \left\{ x \in \Omega \,:\, \phi(x,t) = \frac{1}{2} \right\}.$$

The viscous Cahn-Hilliard equation (3.18)–(3.20) in so far differs from the usual and in [TC94] proposed one as it contains a stabilizing function

$$g = g(\phi) = 30\phi^2(1-\phi)^2, \tag{3.26}$$

which enforces the phase-field variable ϕ to stay in the phases outside the diffuse interface region without influencing the result of the asymptotic analysis (see [KR98]).

In addition, one can incorporate a deposition flux into the diffuse-interface model (3.18)–(3.20) by adding the term

$$\varepsilon^{-1}\tilde{F} = -\varepsilon^{-1}\frac{1}{\gamma(n(\nabla\phi))}B(\phi)F(n(\nabla\phi))\cdot n(\nabla\phi)$$

to the right hand side of (3.18), which yields

$$\partial_t\phi + \nabla\cdot j = -\varepsilon^{-1}\frac{1}{\gamma(n(\nabla\phi))}B(\phi)F(n(\nabla\phi))\cdot n(\nabla\phi), \tag{3.27}$$

see also [EV02]. As in Section 2.1.2, one gets a well defined weak formulation of the system (3.18)–(3.20) by regularizing the anisotropy functions $\tilde{\nu}\circ n$, $\tilde{k}\circ n$ and $F\circ n\cdot n/\gamma\circ n$ in (3.27) by continuous anisotropy functions coinciding with the previous ones for $|p| > \alpha(\varepsilon) = \mathcal{O}(\varepsilon)$ (see Section 2.1.2).

For existence results of (3.18)–(3.20) in the isotropic case, we refer to [EG96]. Cahn-Hilliard models with a degenerate mobility as in (3.23) have numerically been treated in many different applications in [BBG99, BBG01, EV02, WLKJ04], for example. Anisotropic phase-field models have been proposed and justified by matched asymptotic expansions in [MWB$^+$93]. A matched asymptotic analysis formally showing the convergence of the viscous Cahn-Hilliard equation (3.18)–(3.20) towards the sharp-interface model (3.8)–(3.10) as $\varepsilon \to 0$ has been given in [RRV06] and also follows from the analysis in Section 2.2 by setting $D = 0$, i.e. by forbidding diffusion outside the interface. In order to achieve more rigorous results, one would have to apply techniques from [ABC94].

3.2 Numerical Treatment

In this section, we mainly use the algorithm presented in Section 2.3.1, in order to obtain numerical results for the viscous Cahn-Hilliard equation in the continuous

application described in Section 3.1. In Section 3.2.1, we briefly specify the corresponding changes to the discretization in Section 2.3.1 which have been carried out. Afterwards, the model and the algorithm are validated for $d = 2$ by simulations of the ATG instability, where a prescribed analytic expression for the elastic energy density as in [BMN04] has been applied. Thereby, a comparison with results of sharp-interface simulations (the algorithm being described in [BHL$^+$04]) and of a stability analysis are shown for the two extreme cases volume preserving mean curvature flow (3.11) and surface diffusion (3.12) without anisotropy. As a second example, the smoothing property of the model is studied for closed curves and surfaces, and, finally, we investigate evolutions for $d = 2$ and $d = 3$ in anisotropic situations.

3.2.1 Discretization

We apply the algorithm presented in Section 2.3.1 (see also [RRV06]). In order to regularize the degenerate mobility (3.23), we add a small positive constant $\delta \ll \varepsilon$ to the mobility

$$M_\varepsilon(\phi) := \delta + \varepsilon^{-1}\tilde{\nu}(n(\nabla\phi))B(\phi).$$

In the numerical results, we have used the value $\delta = 10^{-4}$.

We solve the system in a cubic domain $\Omega = (-L, L)^d \subset \mathbb{R}^d$ with $L > 0$ and $d = 2$ or $d = 3$. For the definition of the boundary conditions of ϕ and w on $\partial\Omega$, we divide $\partial\Omega$ into the three parts (see Figure 3.3)

$$\Gamma_1 := \{x \in \partial\Omega \,:\, x_d = L\},$$
$$\Gamma_3 := \{x \in \partial\Omega \,:\, x_d = -L\},$$

and

$$\Gamma_2 := \{x \in \partial\Omega \,:\, |x_1| = L \text{ or } |x_2| = L\} \quad \text{for} \quad d = 3,$$
$$\Gamma_2 := \{x \in \partial\Omega \,:\, |x_1| = L\} \quad \text{for} \quad d = 2.$$

On the top of the cube, i.e. on Γ_1, the boundary conditions are prescribed by $\phi = w = 0$. The boundary conditions between film and substrate, i.e. on Γ_3 are zero flux for ϕ and w. On the lateral parts of the boundary Γ_2, we assume ϕ and w to be periodic.

For the weak formulation, we use the space of test functions

$$X := \left\{\psi \in \mathrm{H}^1(\Omega) \,:\, \psi_{|\Gamma_1} = 0, \psi_{|\Gamma_2}\text{periodic}\right\},$$

and for the discretization, the finite element space of globally continuous, piecewise linear elements

$$\mathbb{V}_h^m = \left\{v_h \in X \,:\, v_h|_T \in \mathbb{P}^1 \;\; \forall T \in \mathcal{T}_h^m\right\}$$

with a conforming triangulation $\mathcal{T}_h^m$ of Ω at time instant t_m. Concerning the term in (3.20) involving the function g (see (3.26)), we have explicitly treated the phase-field variable.

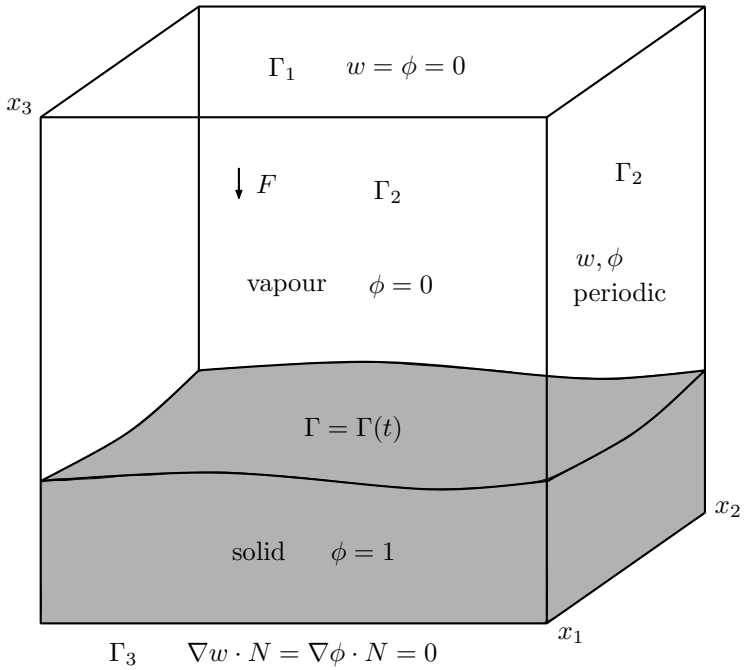

Figure 3.3: Computational domain and boundary conditions.

3.2.2 Crack Formation

In this section, we consider for $d = 2$ the physical situation as described in Figure 3.2. An elastic energy density Ψ resulting from a misfit in lattice parameters of film and substrate can be incorporated into the sharp-interface model (3.8)–(3.10) by changing (3.10) into

$$v = k\left(-H_\varphi + w - \Psi\right),$$

where one usually considers an elasticity problem, in order to determine the elastic energy density Ψ (see e.g. [RRV06]). Here, we follow [BMN04] and introduce a simplified (and unphysical) prescribed energy density depending only on the height of the film. This can easily be incorporated into the diffuse-interface model by changing (3.20) into

$$\varepsilon \tilde{k}^{-1} \partial_t \phi = \mu_2 \left(\nabla \cdot E_p(\phi, \nabla\phi) - \varepsilon^{-1} G'(\phi)\right) + g(\phi) w - g(\phi)\Psi$$

with $\Psi = \Psi(x_2)$ as defined below in (3.29).

In order to further demonstrate the validity of the viscous Cahn-Hilliard equation with elasticity, we compare the numerical solutions with the corresponding sharp-interface models in the limits $k \to \infty$ and $\nu \to \infty$ for $d = 2$, i.e. in the case of curves (see [RRV06]). For these equations and a prescribed elastic energy density, the Asaro-Tiller-Grinfeld instability can be used as a test case in two dimensions. In all simulations, we keep the parameter $\varepsilon = 0.1$ fixed.

Extreme Case $k \to \infty$

According to the extreme case $k \to \infty$, we introduce the evolution equation

$$v = \partial_{ss}(H + \Psi), \tag{3.28}$$

with ∂_s the derivative with respect to the arc length. The elastic energy density Ψ is given by

$$\Psi(x_2) = -\frac{C}{x_2 + L + r}, \quad -L = \inf_{x \in \Omega} x_2, \quad r > 0. \tag{3.29}$$

In the case of a graph formulation, (3.28) and (3.29) with $r = 0$ have been considered in [BMN04], in order to study crack formation. Here, the positive number r in (3.29) has a regularizing meaning. We consider the domain $\Omega := (-1, 1) \times (-1, 1)$, the flat interface

$$\Gamma := \{(x_1, x_2) \in \Omega \ : \ x_2 = 0\}$$

and a perturbed (with wavenumber $l = 1$ and amplitude $A_0 = 0.05$) interface

$$\tilde{\Gamma} := \{(x_1, x_2) \in \Omega \ : \ x_2 = -0.05 \cos(\pi x_1)\}. \tag{3.30}$$

Following the linear stability analysis in [BMN04], one obtains the growth rate

$$\omega(l = 1) = -\pi^4 + \frac{C}{(1 + r)^2}\pi^2. \tag{3.31}$$

For the numerical results presented here, the parameters $C = 50$ and $r = 1/2$ have been used, which yield the growth rate $\omega = \pi^2(\frac{200}{9} - \pi^2) \approx 121.92$. According to the perturbed interface (3.30), we assume for the viscous Cahn-Hilliard equation the initial condition

$$\phi(x, 0) = \frac{1}{2}\left(1 - \tanh\left(\frac{3(x_2 - A_0 \cos(l x_1))}{\varepsilon}\right)\right).$$

In Figure 3.4, a comparison of a sharp-interface simulation of (3.28) with a diffuse-interface simulation of (3.18)–(3.20) with $\varphi = 1$, $\nu = 1$ and $k = 500$ at different times is shown. For the sharp-interface simulations, the algorithm in [BHL$^+$04] is used. We show the plots of the evolving curve at three different times compared to the level sets $\{\phi = 1/2\}$ at corresponding times, which illustrates the good agreement of the two approaches. Figure 3.5 for one time t shows the approximation of the sharp-interface solution by the level sets of the results of the viscous Cahn-Hilliard equation for increasing kinetic coefficient k. This approximation can also be seen in the plots of the logarithm of the amplitudes

$$A = A(t) = \frac{1}{2}\left(\max_{x \in \Gamma(t)} x - \min_{x \in \Gamma(t)} x\right)$$

versus time in Figure 3.6, where Γ is either the numerically determined level set $\{\phi = 1/2\}$ or the result of the sharp-interface simulation. In order to compute the growth rate, linear fits of these plots have been performed to determine the slope (fit-interval: [0,0.01]). The result of this procedure can be seen in Table 3.1.

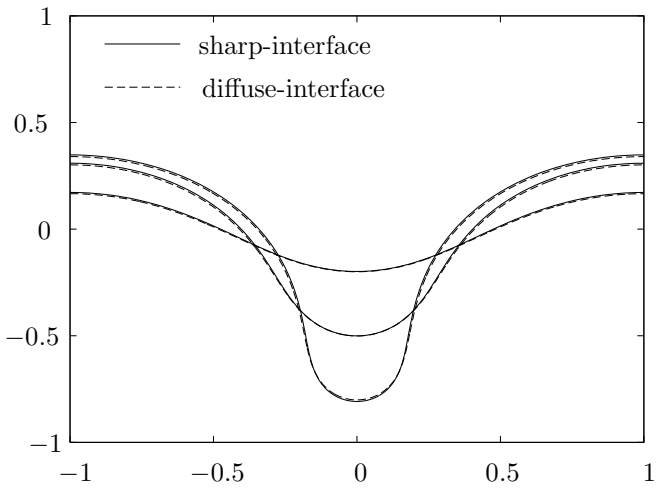

Figure 3.4: Sharp-interface versus diffuse-interface at times $t = 0.0108$, $t = 0.0171$ and $t = 0.0189$, where $k = 500$.

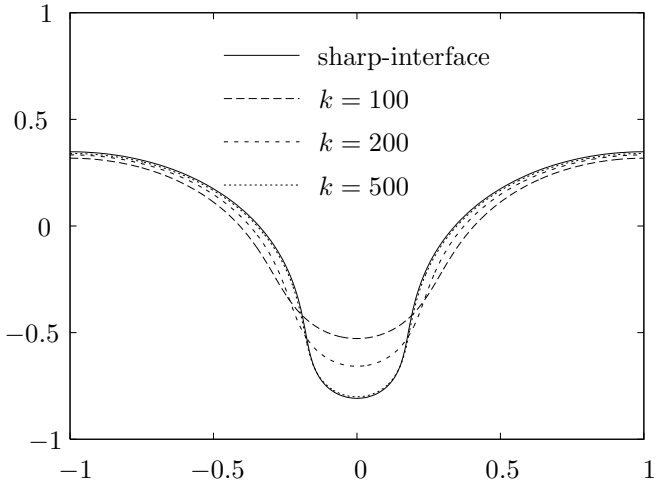

Figure 3.5: Comparison of sharp-interface results with level sets of diffuse-interface model for increasing k at time $t = 0.0189$.

	analytic	sharp-interface	$k = 500$	$k = 200$	$k = 100$
growth rate	121.92	121.45	120.17	116.41	110.69

Table 3.1: Comparison of growth rate computed by diffuse-interface model for increasing k with result of sharp-interface simulation and theoretically determined growth rate.

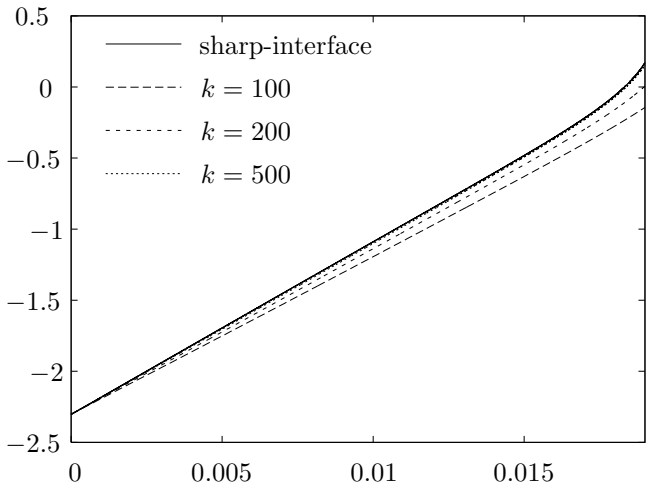

Figure 3.6: Approximation of amplitude computed by sharp-interface simulation by amplitude computed by diffuse-interface model for increasing k.

Extreme Case $\nu \to \infty$

As a second example, we introduce for the extreme case $\nu \to \infty$ the evolution law

$$v = -(H - \overline{H} + (\Psi - \overline{\Psi})), \tag{3.32}$$

where

$$\overline{H} := \frac{1}{|\Gamma|} \int_\Gamma H \, \mathrm{d}s \quad \text{and} \quad \overline{\Psi} := \frac{1}{|\Gamma|} \int_\Gamma \Psi \, \mathrm{d}s$$

and Ψ given by (3.29). Similar to the case of (3.28), a linear stability analysis yields the growth rate

$$\omega(l = 1) = -\pi^2 + \frac{C}{(1 + r)^2} = -\pi^2 + \frac{50}{2.25} \approx 12.35 \tag{3.33}$$

with C and r as before.

Concerning this weaker instability, a similar comparison as for the extreme case $k \to \infty$ is now presented for the second extreme case $\nu \to \infty$ corresponding to volume preserving mean curvature flow. Figure 3.7, thereby, shows the approximation of the result of a sharp-interface simulation of (3.32) by level sets of the phase-field function ϕ computed as a solution of the system (3.18)–(3.20) with $\varphi = 1$, $k = 1$ and $\nu = 16$ at different times. Again, the details of the algorithm used for the sharp-interface solution can be found in [BHL$^+$04]. In Figure 3.8, the convergence of the level sets resulting from phase-field computations with increasing ν to the sharp-interface solution for a selected time is indicated. Figure 3.9 shows the convergence of the logarithm of the amplitudes for increasing parameter ν towards the result of the sharp-interface computation. Table 3.2 shows the growth rates obtained from the linear fits of the curves in Figure 3.9 (fit interval [0,0.05]).

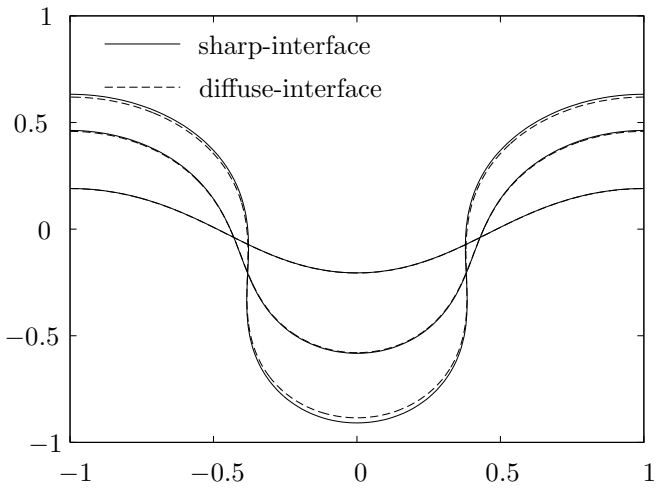

Figure 3.7: Sharp-interface versus diffuse-interface at times $t = 0.106$, $t = 0.163$ and $t = 0.177$, where $\nu = 16$.

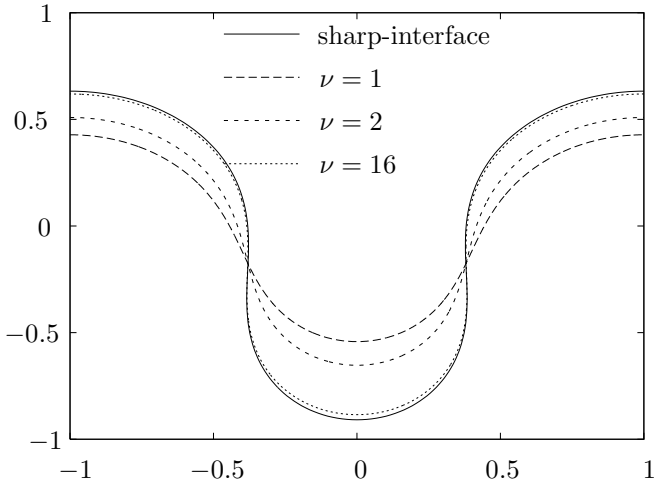

Figure 3.8: Comparison of sharp-interface results with level sets of solutions of diffuse-interface model for increasing ν at time $t = 0.177$.

	analytic	sharp-interface	$\nu = 16$	$\nu = 2$	$\nu = 1$
growth rate	12.35	12.58	12.52	11.97	11.41

Table 3.2: Comparison of growth rate computed by diffuse-interface model for increasing ν with result of sharp-interface simulation and theoretically determined growth rate.

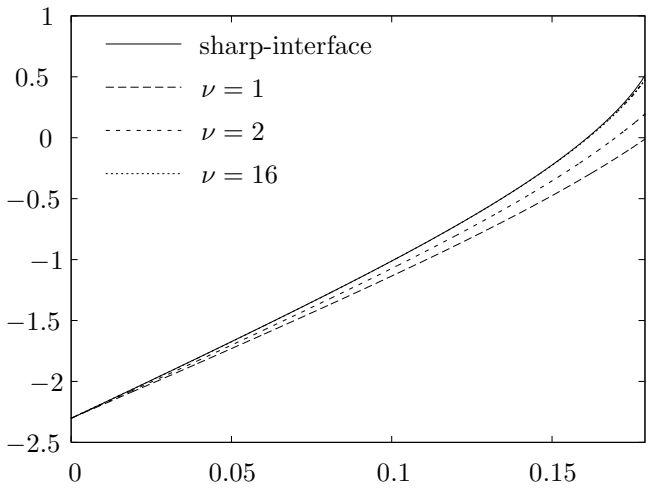

Figure 3.9: Approximation of amplitude computed by sharp-interface simulation by amplitude computed by diffuse-interface model for increasing ν.

For both extreme cases, the viscous Cahn-Hilliard equation shows excellent agreement with the sharp-interface results and the theoretically predicted growth rates. As a consequence, the viscous Cahn-Hilliard equation can be assumed to be valid in the whole parameter range going from surface diffusion to attachment-detachment dominated evolution.

3.2.3 Smoothing Property

In this section, we want to present basic properties of the evolution equations (3.8)–(3.10) and their extreme cases volume preserving mean curvature flow (3.11) and motion by surface diffusion (3.12) in the isotropic situation ($\varphi = 1$) by studying numerical results of the viscous Cahn-Hilliard equation (3.18)–(3.20), where we approximate the sharp-interface models with $k = 10^4$ and $\nu = 1$ for the extreme case (3.12), with $k = 1$ and $\nu = 16$ for the extreme case (3.11) and with $k = 100$ and $\nu = 1$ for an intermediate case. In all cases, we fix $\Omega := (-1, 1)^2$ and $\varepsilon = 0.1$.

As a first test case, we consider closed curves in Ω. In Figure 3.10, one can see the evolution of a perturbed circle (wavenumber $l = 12$, amplitude $A_0 = 0.1$, radius 0.5), i.e. we have started the simulations with

$$\phi(x, 0) := \frac{1}{2}\left(1 - \tanh\left(\frac{3(|x| - 0.5 + A_0 \cos(l\theta(x)))}{\varepsilon}\right)\right),$$

where $\theta(x)$ is the angle of x (see (2.35)). One notices that the interface converges in time towards the stationary solution given by a circle and that the amplitude of the perturbation shrinks fastest in the case of surface diffusion followed by the intermediate case and the extreme case of mean curvature flow.

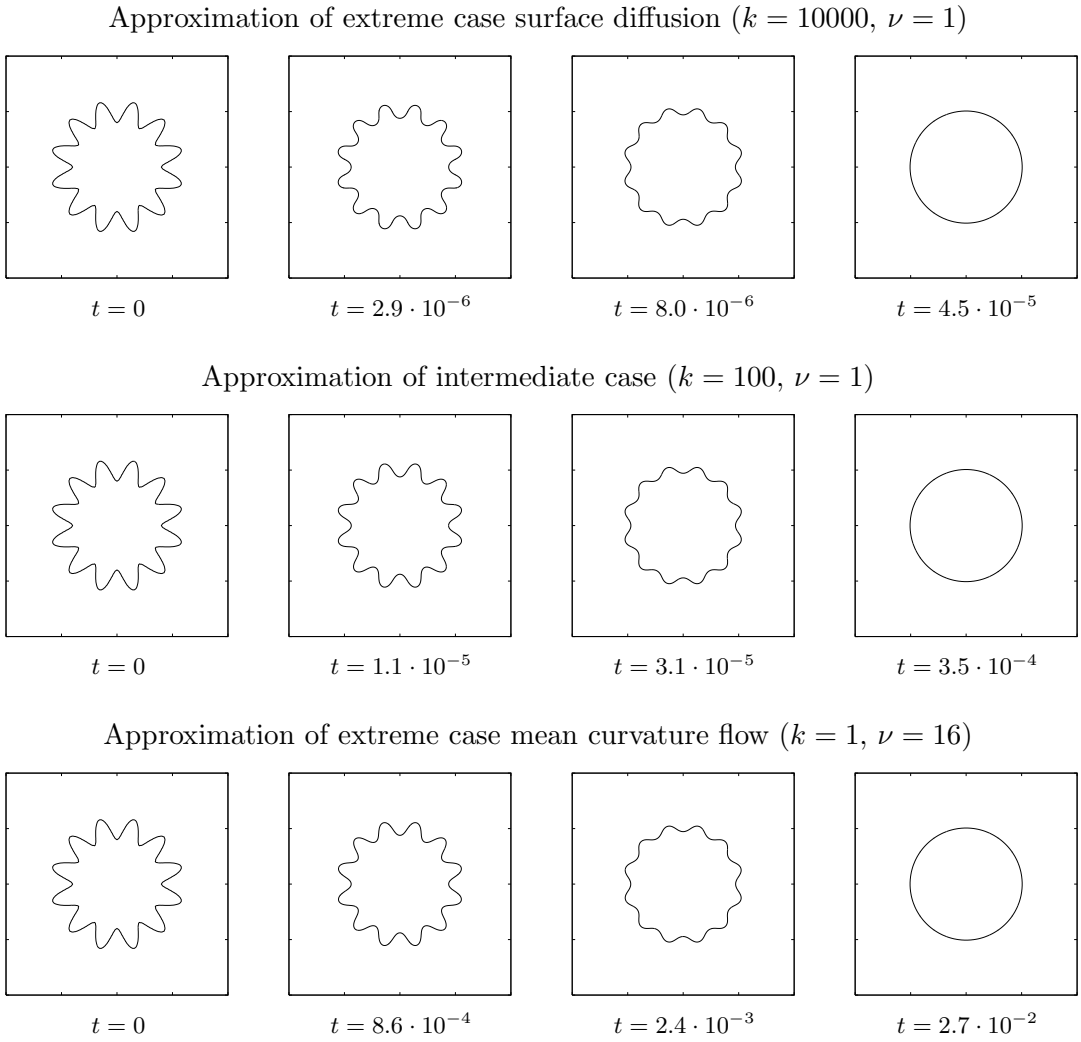

Figure 3.10: Evolution of perturbed circle (wavenumber 12) for different times and in different parameter regimes.

The second example in Figure 3.11 shows evolutions starting with a square-shaped interface in the same three cases as above. So, we change the initial condition into

$$\phi(x,0) := \frac{1}{2}\left(1 - \tanh\left(\frac{3(|x|_\infty - 0.5)}{\varepsilon}\right)\right),$$

where $|\cdot|_\infty$ denotes the maximum norm

$$|x|_\infty := \max(|x_1|, \ldots, |x_d|) \quad \text{for} \quad x \in \mathbb{R}^d.$$

Again, one notices the differences in the smoothing properties according to the time scales on which the equations relax. Furthermore, in the extreme case of surface

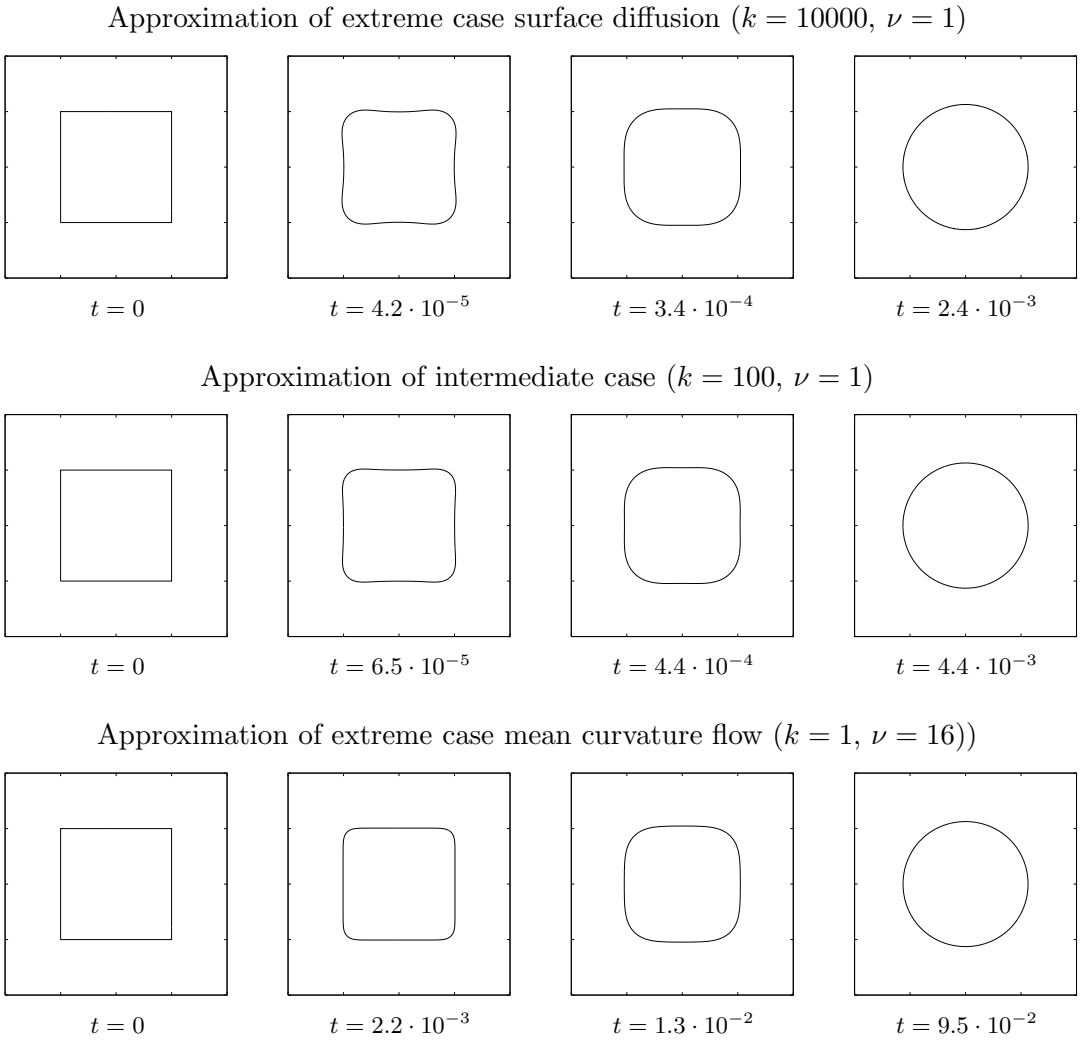

Figure 3.11: Evolution of square for different times in different parameter regimes.

diffusion one can see temporary non-convex shapes, which are more distinct than in the intermediate case. In the extreme case of mean curvature flow, however, these non-convex shapes do not appear.

3.2.4 Isotropic Evolution for $d = 3$

In this section, we follow [BMN05] and provide simulations describing the evolution of initial conditions $\phi(x, 0)$ with prism-shaped level sets $\{\phi(x, 0) = 1/2\}$ for $d = 3$. To be more precise, we use the initial condition

$$\phi(x, 0) := \frac{1}{2}\left(1 - \tanh\left(\frac{3(r(x))}{\varepsilon}\right)\right),$$

where $r = r(x)$ denotes the signed distance of a point $x \in \Omega := (-5,5)^3$ to the prism being positive inside and negative outside the prism. Furthermore, we assume throughout this section ϕ and w to be Ω-periodic and $\varepsilon = 0.25$. First, we consider for $d = 3$ an example similar to the one presented in Figure 3.11. Thereby, we begin with the parameters

$$k = 1000, \quad \nu = 1.$$

Thus, we are interested in an approximation of the extreme case (3.12) in the isotropic situation. In Figure 3.12, one can see the evolution of an initially cubic (with edge length 1) level set towards a sphere showing slightly non-convex shapes at intermediate times.

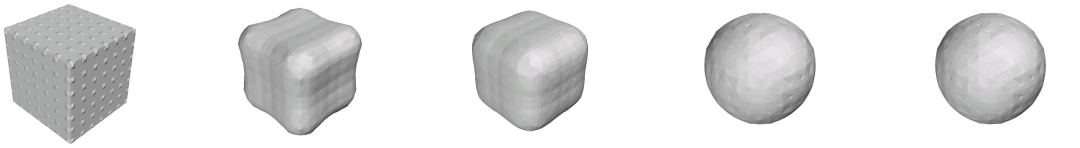

$t = 0$ $t = 7 \cdot 10^{-5}$ $t = 2.4 \cdot 10^{-4}$ $t = 2.28 \cdot 10^{-3}$ $t = 1.110 \cdot 10^{-2}$

Figure 3.12: Evolution of $1 \times 1 \times 1$ prism to a sphere.

As a second example, we have in Figure 3.13 the evolution of a $4 \times 1 \times 1$ prism towards a sphere, again, with non-convex intermediate shapes. Thereby, we have chosen in Figure 3.13 similar times as in the presentation of sharp-interface results for the same example in [BMN05], and we obtain a good qualitative agreement.

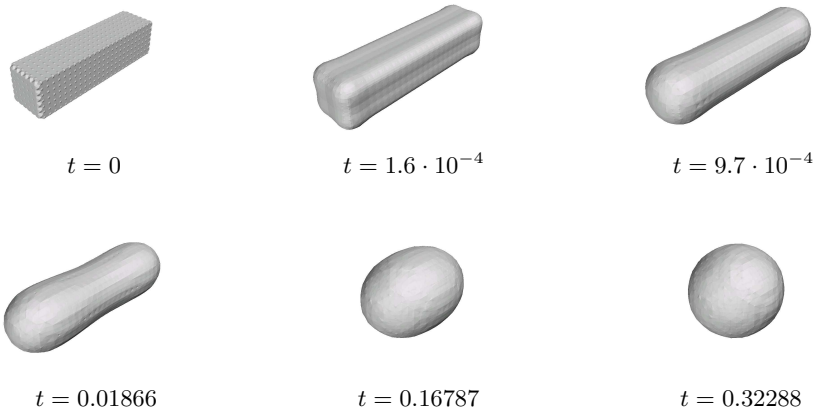

$t = 0$ $t = 1.6 \cdot 10^{-4}$ $t = 9.7 \cdot 10^{-4}$

$t = 0.01866$ $t = 0.16787$ $t = 0.32288$

Figure 3.13: Evolution of $4 \times 1 \times 1$ prism to a sphere.

Doubling the proportions of the edge lengths, i.e. considering the evolution of an $8 \times 1 \times 1$ prism, leads to a pinch-off (see Figure 3.14). As the stationary solution, we obtain two spheres of equal size. Again, the results of the diffuse-interface approximation qualitatively agree with those presented in [BMN05] for

corresponding time steps. Furthermore, the pinch-off time in the case of the diffuse-interface approximation has a deviation of $\approx 7.8\%$ compared to the sharp-interface pinch-off time in [BMN05]. Due to the fact that the entire surface area of two spheres of equal size is larger than the surface area of a single sphere enclosing the same volume as the two spheres together, this example shows that the evolution law (3.12) does not necessarily lead to the globally minimal equilibrium shape.

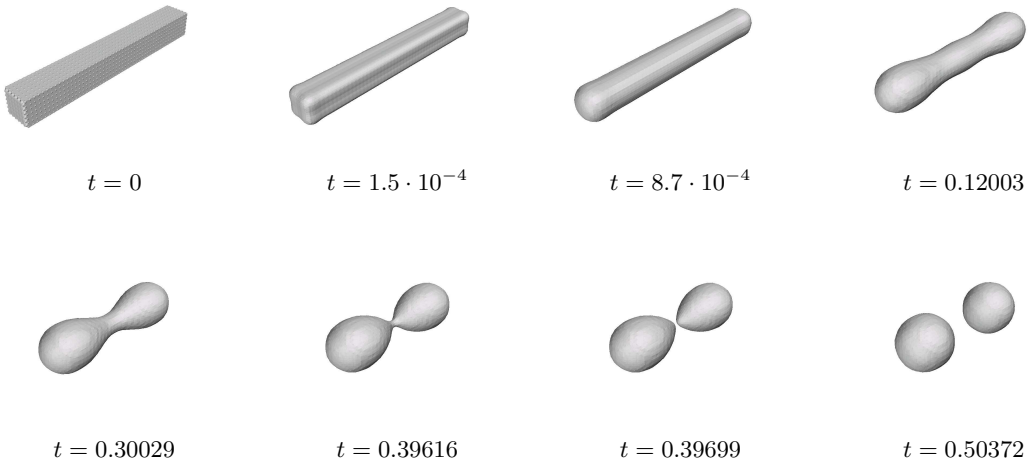

Figure 3.14: Evolution of a $8 \times 1 \times 1$ prism including pinch-off and two spheres of equal size as stationary solution.

Now, in Figure 3.15, we present results of a simulation in an intermediate parameter regime, where we chose

$$k = 10, \quad \nu = 1.$$

In contrast to the previous case, in Figure 3.14, a pinch-off does not occur and the equilibrium shape is a single sphere. However, one can still see rather strong non-convexities at several time steps.

Finally, in Figure 3.16, one can see in Figure 3.16 numerical results of a diffuse-interface approximation for the parameters

$$k = 1, \quad \nu = 20$$

as an approximation of the sharp-interface evolution law (3.11) in the isotropic situation, where the non-convex shapes from the previous example have vanished in this case.

3.2.5 Anisotropic Evolution for $d = 2$ and $d = 3$

As a last example, we analyze for $d = 2$ and $d = 3$ various anisotropies in the viscous Cahn-Hilliard equation (see [RRV06]). We consider a weak anisotropy in the free

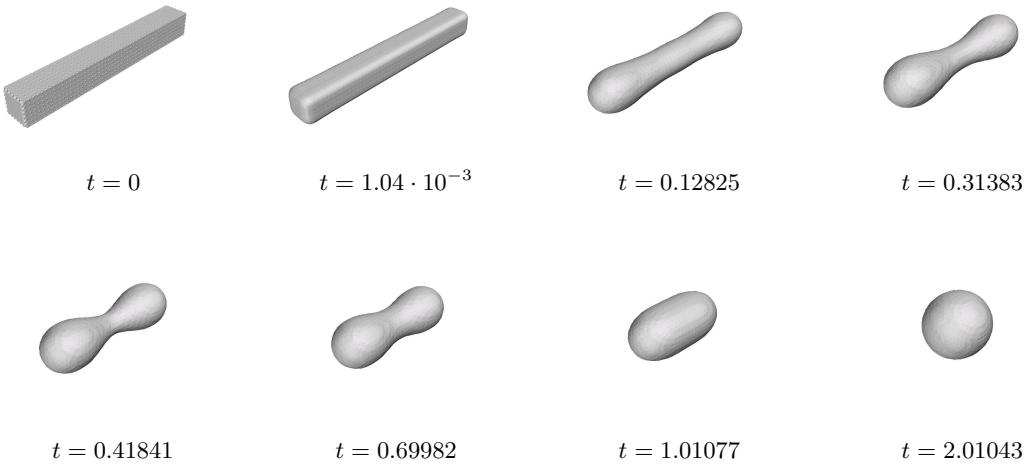

$t = 0$ $t = 1.04 \cdot 10^{-3}$ $t = 0.12825$ $t = 0.31383$

$t = 0.41841$ $t = 0.69982$ $t = 1.01077$ $t = 2.01043$

Figure 3.15: Evolution of a $8 \times 1 \times 1$ prism without pinch-off and with one sphere of equal size as stationary solution for intermediate parameters $k = 10$ and $\nu = 1$.

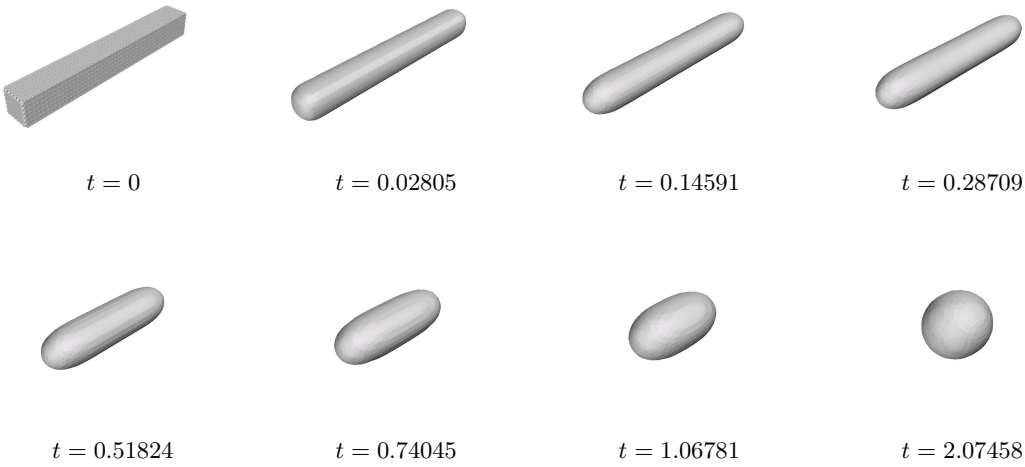

$t = 0$ $t = 0.02805$ $t = 0.14591$ $t = 0.28709$

$t = 0.51824$ $t = 0.74045$ $t = 1.06781$ $t = 2.07458$

Figure 3.16: Evolution of a $8 \times 1 \times 1$ prism without pinch-off and with one sphere of equal size as stationary solution for parameters $k = 1$ and $\nu = 20$.

energy density $\varphi(N) = \mu_2\gamma(N)$ and a strong anisotropy in the kinetic coefficient $k(N)$. The computational domain is $\Omega := (-1, 1)^d$, and we fix $\varepsilon = 0.1$, $\nu = 1$, $\mu_2 = 1$ as well as the initial condition

$$\phi(x, 0) := \frac{1}{2}\left(1 - \tanh\left(\frac{3(|x| - 0.2)}{\varepsilon}\right)\right)$$

representing a circle or sphere, respectively.

Anisotropic Free Energy Density

We first use an anisotropy function (see [Bur05]) $\gamma(N)$ of the form

$$\gamma(N) = 1 + \varepsilon_4 \sum_{i=1}^{d} N_i^4, \tag{3.34}$$

with $\varepsilon_4 = 0.3$, providing γ to be convex (see Figure 3.17 for a polar plot for $d = 2$). Figure 3.18 and Figure 3.19 show the evolution of a closed curve or surface towards

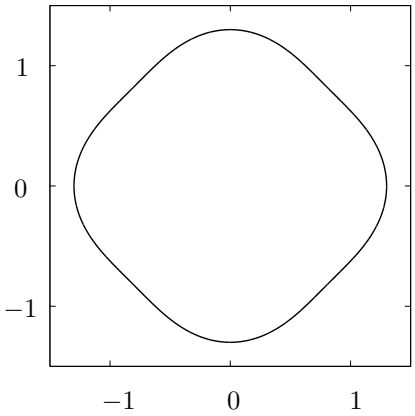

Figure 3.17: Polar plot of anisotropy function (3.34) for $d = 2$.

its Wulff shape in two and three dimensions, respectively, where we have solved the system (3.18)–(3.20) with isotropic kinetic coefficient $k = 1$, still leading to an anisotropic coefficient $\tilde{k}$ (see (3.25)).

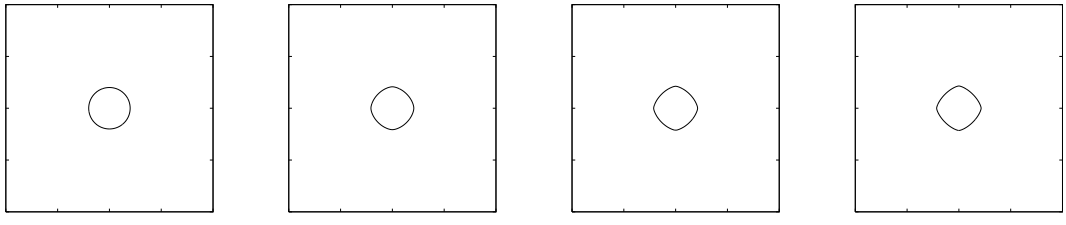

Figure 3.18: Evolution of level set $\{\phi = 1/2\}$ towards the Wulff shape for $d = 2$.

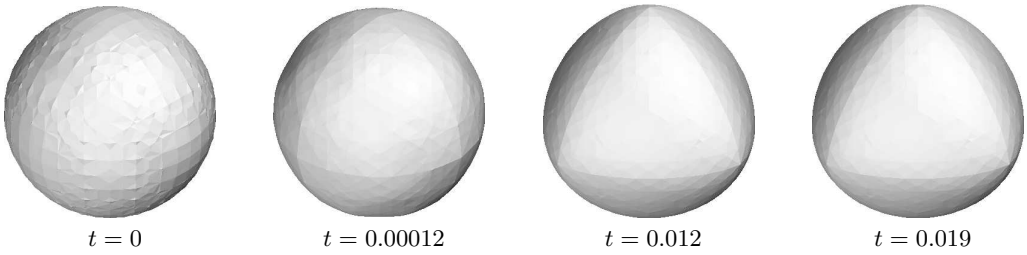

Figure 3.19: Evolution of level set $\{\phi = 1/2\}$ towards the Wulff shape for $d = 3$.

Anisotropic Kinetic Coefficient

Now, we additionally account for an anisotropy in the kinetic coefficient $k(N)$ (see [US03] for a similar anisotropic kinetic coefficient and Figure 3.20 for a polar plot)

$$k(N) = 1 - \tilde{\varepsilon}_4 + 2\tilde{\varepsilon}_4 \tanh\left\{ k_4 \left(\sqrt{d} - \sum_{i=1}^{d} |N_i| \right) \Big/ \left(1 - \sum_{i=1}^{d} N_i^4 \right) \right\} \tag{3.35}$$

with $k_4 = 50$ and $\tilde{\varepsilon}_4 = 0.9$. Figure 3.21 and Figure 3.22 then show the evolution of a

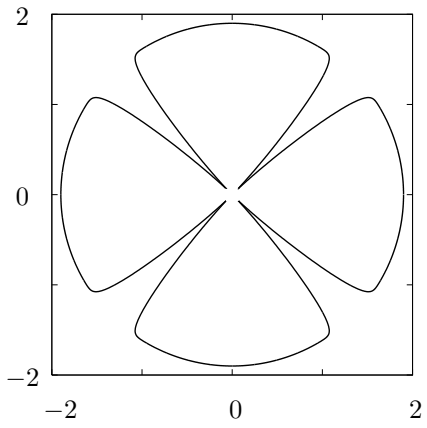

Figure 3.20: Polar plot of anisotropy function (3.35) for $d = 2$.

closed curve or surface towards its kinetic Wulff shape in two and three dimensions, respectively, where we solve (3.18)–(3.20) with an additional deposition flux (see (3.27)) with $F(N) = -10N$, for which (3.27) simplifies into

$$\partial_t \phi + \nabla \cdot j = \varepsilon^{-1} \frac{10}{\gamma(n(\nabla\phi))} B(\phi).$$

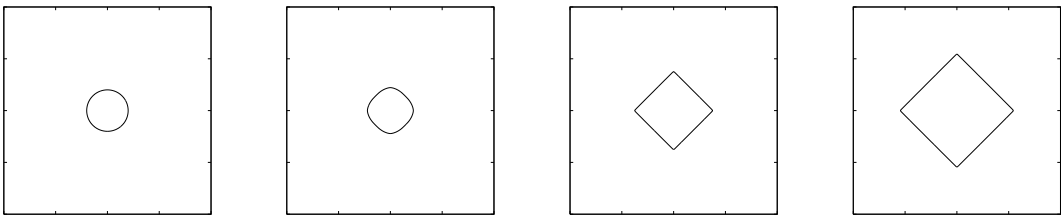

$t = 0$ $t = 0.0010$ $t = 0.010$ $t = 0.025$

Figure 3.21: Evolution of level set $\{\phi = 1/2\}$ towards the kinetic Wulff shape for $d = 2$.

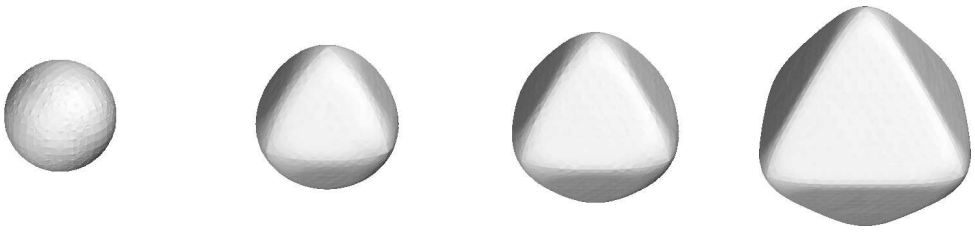

$t = 0$ $t = 0.0052$ $t = 0.0087$ $t = 0.015$

Figure 3.22: Evolution of level set $\{\phi = 1/2\}$ towards the kinetic Wulff shape for $d = 3$.

Bibliography

[ABC94] N.D. Alikakos, P.W. Bates, and X. Chen. The convergence of solutions of the Cahn-Hilliard equation to the solution of the Hele-Shaw model. *Arch. Rational Mech. Anal.*, 128(2):165–205, 1994.

[AC79] S.M. Allen and J.W. Cahn. Microscopic theory for antiphase boundary motion and its application to antiphase domain coarsening. *Acta Metall.*, 27(6):1085–1095, 1979.

[And01] B. Andrews. Volume-preserving anisotropic mean curvature flow. *Indiana Univ. J.*, 50(2):783–827, 2001.

[AT72] R. Asaro and W.A. Tiller. Interface morphology development during stress-corrosion cracking. 1. via surface diffusion. *Metall. Trans.*, 3(7):1789–, 1972.

[Avi71] M. Avignon. Role of interface kinetics on the shape stability of a two-dimensional nucleus on a substrate. *J. Crys. Growth*, 11:265–272, 1971.

[Avi72] M. Avignon. Shape stability of a two-dimensional nucleus. *J. Crys. Growth*, 13/14:113–120, 1972.

[BBG99] J.W. Barrett, J.F. Blowey, and H. Garcke. Finite element approximation of the Cahn-Hilliard equation with degenerate mobility. *SIAM J. Numer. Anal.*, 37(1):286–318, 1999.

[BBG01] J.W. Barrett, J.F. Blowey, and H. Garcke. On fully practical finite element approximations of degenerate Cahn-Hilliard systems. *Math. Model. Num. Anal. (M2AN)*, 35(4):713–748, 2001.

[BCE+06] L. Balykov, V. Chalupecky, C. Eck, H. Emmerich, G. Krishnamoorthy, A. Rätz, and A. Voigt. Multiscale Modeling of Epitaxial Growth: From Discrete-Continuum to Continuum Equations. In A. Mielke, editor, *Analysis, Modeling and Simulation of Multiscale Modeling*, pages 65–85. Springer, 2006.

[BCF51] W.K. Burton, N. Cabrera, and F.C. Frank. The growth of crystals and the equilibrium of their surfaces. *Phil. Trans. Roy. Soc. London Ser. A*, 243(866):299–358, 1951.

[BHL+04] E. Bänsch, F. Haußer, O. Lakkis, B. Li, and A. Voigt. Finite element method for epitaxial growth with attachment-detachment kinetics. *J. Comput. Phys.*, 194(2):409–434, 2004.

[BHSV07] M. Burger, F. Haußer, C. Stöcker, and A. Voigt. A level set approach to anisotropic flows with curvature regularization. *J. Comput. Phys.*, 2007. to appear.

[BHV05] E. Bänsch, F. Haußer, and A. Voigt. Finite element method for epitaxial growth with thermodynamic boundary conditions. *SIAM J. Sci. Comput.*, 26(6):2029–2046, 2005.

[BMN04] E. Bänsch, P. Morin, and R.H. Nochetto. Surface diffusion of graphs: variational formulation, error analysis, and simulation. *SIAM J. Numer. Anal.*, 42(2):773–799, 2004.

[BMN05] E. Bänsch, P. Morin, and R.H. Nochetto. A finite element method for surface diffusion: the parametric case. *J. Comput. Phys.*, 203(1):321–343, 2005.

[BMN07] G. Bellettini, C. Mantegazza, and M. Novaga. Singular Perturbations of Mean Curvature Flow. *J. Differential Geom.*, 2007. to appear.

[BP03] E. Burman and M. Picasso. Anisotropic, adaptive finite elements for the computation of a solutal dendrite. *Interfaces Free Bound.*, 5(2):103–127, 2003.

[Bur05] M. Burger. Numerical simulation of anisotropic surface diffusion with curvature-dependent energy. *J. Comput. Phys.*, 203(2):602–625, 2005.

[BWBK02] W.J. Boettinger, J.A. Warren, C. Beckermann, and A. Karma. Phase-field simulation of solidification. *Annu. Rev. Mater. Res.*, 32:163–194, 2002.

[BZ90] G.S. Bales and A. Zangwill. Morphological instability of a terrace edge during step-flow growth. *Phys. Rev. B*, 41(9):5500–5508, 1990.

[CENC96] J.W. Cahn, C.M. Elliott, and A. Novick-Cohen. The Cahn-Hilliard equation with a concentration-dependent mobility: Motion by minus the Laplacian of the mean curvature. *Euro. J. Appl. Math.*, 7:287–301, 1996.

[CGG91] Y.G. Chen, Y. Giga, and S. Goto. Uniqueness and existence of viscosity solutions of generalized mean curvature flow equations. *J. Differential Geom.*, 33(3):749–786, 1991.

[CH58] J.W. Cahn and J.E. Hilliard. Free energy of a non-uniform system i. interfacial free energy. *J. Chem. Phys.*, 28(2):258–267, 1958.

[Che02] L.-Q. Chen. Phase-field models for microstructure evolution. *Annu. Rev. Mater. Res.*, 32:113–140, 2002.

[CHR+05] U. Clarenz, F. Haußer, M. Rumpf, A. Voigt, and U. Weikard. On level set formulations for anisotropic mean curvature flow and surface diffusion. In A. Voigt, editor, *Multiscale modeling of epitaxial growth*, volume 149 of *ISNM*, pages 227–237. Birkhäuser, Basel, 2005.

[Cla02] U. Clarenz. Enclosure theorems for extremals of elliptic parametric functionals. *Calc. Var.*, 15(3):313–324, 2002.

[CMK+01] S. Chen, B. Merriman, M. Kang, R.E. Caflisch, C. Ratsch, L.T. Cheng, M.F. Gyure, R. Fedkiw, C. Anderson, and S. Osher. Level set method for thin film epitaxial growth. *J. Comp. Phys.*, 167(2):475–500, 2001.

[CR92] X. Chen and F. Reitich. Local existence and uniqueness of solutions of the Stefan problem with surface tension and kinetic undercooling. *J. Math. Anal. Appl.*, 164(2):350–362, 1992.

[CT94] J.W. Cahn and J.E. Taylor. Surface motion by surface-diffusion. *Acta Metall.*, 42(4):1045–1063, 1994.

[CvdM01] U. Clarenz and H. von der Mosel. Compactness theorems and an isoperimetric inequality for critical points of elliptic parametric functionals. *Calc. Var.*, 12(1):85–107, 2001.

[DD02] K. Deckelnick and G. Dziuk. A fully discrete numerical scheme for weighted mean curvature flow. *Numer. Math.*, 91(3):423–452, 2002.

[DDE05a] K. Deckelnick, G. Dziuk, and C.M. Elliott. Computation of geometric partial differential equations and mean curvature flow. *Acta Numerica*, 14:139–232, 2005.

[DDE05b] K. Deckelnick, G. Dziuk, and C.M. Elliott. Fully discrete finite element approximation for anisotropic surface diffusion of graphs. *SIAM J. Numer. Anal.*, 43(3):1112–1138, 2005.

[DGPG92] A. DiCarlo, M.E. Gurtin, and P. Podio-Guidugli. A regularized equation for anisotropic motion-by-curvate. *SIAM J. Appl. Math.*, 52(4):1111–1119, 1992.

[Dzi99] G. Dziuk. Discrete anisotropic curve shortening flow. *SIAM J. Numer. Anal.*, 36(6):1808–1830, 1999.

[EG96] C.M. Elliott and H. Garcke. On the Cahn-Hilliard equation with degenerate mobility. *SIAM J. Math. Anal.*, 27(2):404–423, 1996.

[EG97] C.M. Elliott and H. Garcke. Existence results for diffusive surface motion laws. *Adv. Math. Sci. Appl.*, 7(1):467–490, 1997.

[EH66] G. Ehrlich and F.G. Hudda. Atomic view of surface diffusion: tungsten on tungsten. *J. Chem. Phys.*, 44:1036–1099, 1966.

[Ell89] C.M. Elliott. The Cahn-Hilliard model for the kinetics of phase separation. In J. F. Rodrigues, editor, *Mathematical models for phase change problems*, volume 88 of *ISNM*, pages 35–73. Birkhäuser, Basel, 1989.

[EMS98] J. Escher, U.F. Mayer, and G. Simonett. The surface diffusion flow for immersed hypersurfaces. *SIAM J. Math. Anal.*, 29(6):1419–1433, 1998.

[EPS96] C.M. Elliott, M. Paolini, and R. Schätzle. Interface estimates for the fully anisotropic Allen-Cahn equation and anisotropic mean-curvature flow. *Math. Models Methods Appl. Sci.*, 6(8):1103–1118, 1996.

[ES98] J. Escher and G. Simonett. The volume preserving mean curvature flow near spheres. *P. Am. Math. Soc.*, 126(9):2789–2796, 1998.

[EV02] J.J. Eggleston and P.W. Voorhees. Ordered growth of nanocrystals via a morphological instability. *Appl. Phys. Lett.*, 80(2):306–308, 2002.

[Fif00] P.C. Fife. Models for phase separation and their mathematics. *Electron. J. Differ. Equ.*, Paper No.48, 26 p. (electronic only), 2000.

[FM91] I. Fonseca and S. Müller. A uniqueness proof for the Wulff theorem. *Proc. R. Soc. Edinb. A*, 119(1-2):125–136, 1991.

[FP95] P.C. Fife and O. Penrose. Interfacial dynamics for thermodynamically consistent phase-field models with nonconserved order parameter. *Electron. J. Differ. Equ.*, Paper No.16, 49 p. (electronic only), 1995.

[Gag86] M. Gage. On an area-preserving evolution equation for plane curves. In D. M. DeTurck, editor, *Nonlinear Problems in Geometry*, volume 51 of *Contemporary Mathematics*, pages 251–303. AMS, Providence, 1986.

[Gag93] M. Gage. Evolving plane curves by curvature in relative geometries. *Duke Math. J.*, 72:441–466, 1993.

[GH86] M. Gage and R.S. Hamilton. The heat equation shrinking convex plane curves. *J. Differential Geom.*, 23:69–96, 1986.

[GJ02] M.E. Gurtin and M.E. Jabbour. Interface evolution in three dimensions with curvature-dependent energy and surface diffusion: Interface-controlled evolution, phase transitions, epitaxial growth of elastic films. *Arch. Rat. Mech. Anal.*, 163(3):171–208, 2002.

[GN99] H.J. Gao and W.D. Nix. Surface roughening of heteroepitaxial thin films. *Ann. Rev. Mat. Sci.*, 29:179–209, 1999.

[Gra87] M.A. Grayson. The heat equation shrinks embedded plane curves to round points. *J. Differential Geom.*, 26:285–314, 1987.

[Gri86] M.A. Grinfeld. Instability of interface between nonhydrostatically stressed elastic body and melts. *Doklady Akademii Nauk SSSR*, 290(6):1358–1363, 1986.

[Hui84] G. Huisken. Flow by mean curvature of convex surfaces into spheres. *J. Differential Geom.*, 20:237–266, 1984.

[Hui87] G. Huisken. The volume preserving mean curvature flow. *J. Reine Angew. Math.*, 382:35–48, 1987.

[HV05a] F. Haußer and A. Voigt. A discrete scheme for regularized anisotropic diffusion: a 6th order geometric evolution equation. *Interfaces Free Bound.*, 7(4):353–369, 2005.

[HV05b] F. Haußer and A. Voigt. A finite element framework for Burton-Cabrera-Frank equation. In A. Voigt, editor, *Multiscale modeling of epitaxial growth*, volume 149 of *ISNM*, pages 97–114. Birkhäuser, Basel, 2005.

[HV06] F. Haußer and A. Voigt. A numerical scheme for regularized anisotropic curve shortening flow. *Appl. Math. Lett.*, 19:691–698, 2006.

[KP98] A. Karma and M. Plapp. Spiral surface growth without desorption. *Phys. Rev. Lett.*, 81:4444–4447, 1998.

[KR98] A. Karma and W.-J. Rappel. Quantitative phase-field modeling of dendritic growth in two and three dimensions. *Phys. Rev. E*, 57(4):4323–4349, 1998.

[Kru05] J. Krug. Introduction to step dynamics and step instabilities. In A. Voigt, editor, *Multiscale modeling of epitaxial growth*, volume 149 of *ISNM*, pages 59–95. Birkhäuser, Basel, 2005.

[Law80] H.B. Lawson. *Lectures on minimal submanifolds. Vol. I.* Mathematics Lecture Series, 9. Berkeley, California: Publish Perish, Inc. VI, 178 p., 1980.

[LM94] F. Liu and H. Metiu. Stability and kinetics of step motion on crystal surfaces. *Phys. Rev. E*, 49:2601–2616, 1994.

[LRV04] B. Li, A. Rätz, and A. Voigt. Stability of a circular epitaxial island. *Physica D*, 198:231–247, 2004.

[May00] U.F. Mayer. A numerical scheme for moving boundary problems that are gradient flows for the area functional. *Euro. J. Appl. Math.*, 11(2):61–80, 2000.

[MK04] T. Michely and J. Krug. *Islands, Mounds and Atoms*. Springer, 2004. Patterns and Processes in Crystal Growth Far from Equilibrium.

[Mul57] W.W. Mullins. Theory of Thermal Grooving. *J. Appl. Phys.*, 28(3):333–339, 1957.

[MWB+93] G.B. McFadden, A.A. Wheeler, R.J. Braun, S.R. Coriell, and R.F. Sekerka. Phase-field models for anisotropic interfaces. *Phys. Rev. E*, 48(3):2016–2024, 1993.

[NC88] A. Novick-Cohen. On the viscous Cahn–Hilliard equation. In J.M." Ball, editor, *Material instabilities in continuum and related mathematical problems*, pages 329–342", 1988.

[NC98] A. Novick-Cohen. The Cahn-Hilliard equation: Mathematical and modeling perspectives. *Adv. Math. Sci. Appl.*, 8(2):965–985, 1998.

[OPR+04] F. Otto, P. Penzler, A. Rätz, T. Rump, and A. Voigt. A diffuse-interface approximation for step flow in epitaxial growth. *Nonlin.*, 17:477–491, 2004.

[OPR05] F. Otto, P. Penzler, and T. Rump. Discretisation and Numerical tests of a Diffuse-Interface Model with Ehrlich-Schwoebel Barrier. In A. Voigt, editor, *Multiscale modeling of epitaxial growth*, volume 149 of *ISNM*, pages 127–159. Birkhäuser, Basel, 2005.

[Peg89] R. Pego. Front migration in the nonlinear Cahn-Hilliard equation. *Proc. Roy. Soc. London Ser. A*, 422:261–278, 1989.

[PL03] O. Pierre-Louis. Phase field models for step flow. *Phys. Rev. E*, 68(2):021604, 2003.

[POMZ99] D. Peng, S. Osher, B. Merriman, and H.-K. Zhao. The Geometry of Wulff Crystal Shapes and Its Relations with Riemann Problems. In E. DiBenedetto G. Q. Chen, editor, *Nonlinear partial differential equations*, volume 238 of *Contemporary Mathematics*, pages 251–303, 1999.

[PV98] A. Pimpinelli and J. Villain. *Physics of Crystal Growth*. Cambridge University Press, Cambridge, 1998.

[Rad91] E. Radkevich. Gibbs-Thomson law and existence of the classical solution of the modified Stefan problem. *Soviet Dokl. Acad. Sci.*, 43:274–278, 1991.

[RRV06] A. Rätz, A. Ribalta, and A. Voigt. Surface evolution of elastically stressed films under deposition by a diffuse interface model. *J. Comput. Phys.*, 214(1):187–208, 2006.

[RS04] A. Ramasubramaniam and V.B. Shenoy. Three-dimensional simulations of self-assembly of hut-shaped Si-Ge quantum dots. *J. Appl. Phys.*, 95(12):7813–7824, 2004.

[RV04] A. Rätz and A. Voigt. Phase-field models for island dynamics in epitaxial growth. *Appl. Anal.*, 83:1015–1025, 2004.

[RV05] A. Rätz and A. Voigt. A diffuse step-flow model with edge-diffusion. In A. Voigt, editor, *Multiscale modeling of epitaxial growth*, volume 149 of *ISNM*, pages 115–126. Birkhäuser, Basel, 2005.

[RV06] A. Rätz and A. Voigt. PDE's on surfaces – a diffuse interface approach. *Comm. Math. Sci.*, 4(3):575–590, 2006.

[Sch69] R.L. Schwoebel. Step motion on crystal surfaces II. *J. Appl. Phys.*, 40:614–618, 1969.

[SF02] V.B. Shenoy and L.B. Freund. A continuum description of the energetics and evolution of stepped surfaces in strained nanostructures. *J. Mech. Phys. Solids*, 50(9):1817–1841, 2002.

[Son93] H.M. Soner. Motion of a set by the curvature of its boundary. *J. Differ. Equations*, 101(2):313–372, 1993.

[Sro89] D.J. Srolovitz. On the stability of surfaces of stressed solids. *Acta Metall.*, 37(2):621–625, 1989.

[SS66] R.L. Schwoebel and E.J. Shipsey. Step motion on crystal surfaces. *J. Appl. Phys.*, 37:3682–3686, 1966.

[Tay78] J.E. Taylor. Crystalline variational problems. *Bull. Am. Math. Soc.*, 84:568–588, 1978.

[TC94] J.E. Taylor and J.W. Cahn. Linking anisotropic sharp and diffuse surface motion laws via gradient flows. *J. Stat. Phys.*, 77(1–2):183–197, 1994.

[US03] T. Uehara and R.F. Sekerka. Phase field simulations of faceted growth for strong anisotropy of kinetic coefficient. *J. Cryst. Growth*, 254(1–2):251–261, 2003.

[VV07] S. Vey and A. Voigt. AMDiS – adaptive multidimensional simulations. *Comput. Visual. Sci.*, 2007. to appear.

[WLKJ04] S.M. Wise, J.S. Lowengrub, J.S. Kim, and W.C. Johnson. Efficient phase-field simulation of quantum dot formation in a strained heteroepitaxial film. *Superlattice. Microst.*, 36(1–3):293–304, 2004.

[Wol01] Wolfram Research, Inc. *Mathematica, Version 4.1.* Champaign, Illinois, 2001.

[Wul01] G. Wulff. Zur Frage der Geschwindigkeit des Wachsthums und der Auflösung der Kristallflächen. *Zeitschrift der Kristallographie*, 34:449–530, 1901.

[XE04] Y. Xiang and W. E. Misfit elastic energy and a continuum model for epitaxial growth with elasticity on vicinal surfaces. *Phys. Rev. B*, 69(3):035409, 2004.

[Xia02] Y. Xiang. Derivation of a continuum model for epitaxial growth with elasticity on vicinal surface. *SIAM J. Appl. Math.*, 63(1):241–258, 2002.

[ZB99] Y.W. Zhang and A.F. Bower. Numerical simulations of island formation in a coherent strained epitaxial thin film system. *J. Mech. Phys. Solids*, 47(11):2273–2297, 1999.

[ZBL03] Y.W. Zhang, A.F. Bower, and P. Liu. Morphological evolution driven by strain induced surface diffusion. *Thin Solid Films*, 424(1):9–14, 2003.

Lebenslauf

Persönliche Daten

Name:	Andreas Rätz
	Geboren am 12.03.1975 in Bonn
Adresse:	Kölnstraße 118
	53111 Bonn
	Telefon: 0228/3360025
	e-mail: raetz@caesar.de

Schulausbildung

06/1994	Abitur am Geschwister-Scholl-Gymnasium Daun

Studium

10/1994	Beginn des Mathematik-Studiums an der Universität Bonn
02/1997	Vordiplom
04/1997-04/1999	Spezialisierung auf die Theorie der partiellen Differentialgleichungen
11/2001	Abgabe der Diplomarbeit unter der Betreuung von Prof. Hildebrandt mit dem Thema "Variationsprobleme und Liouville-Sätze für Euler-Gleichungen auf einem Torus"
06/2002	Abschluss der Diplomprüfungen
seit 08/2002	Arbeit an der Modellierung und Simulation von epitaktischen Wachstumsprozessen in der Arbeitsgruppe Crystal Growth am Forschungsinstitut caesar unter der Leitung von PD Dr. Axel Voigt
01/2007	Abgabe der Dissertion mit dem Titel "Modelling and Numerical Treatment of Diffuse-Interface Models with Applications in Epitaxial Growth"

Publikationen

1. B. Li, A. Rätz, A. Voigt. Stability of a circular epitaxial island. *Physica D*, 198:231–247, 2004.

2. A. Rätz, A. Voigt. Phase-field models for island dynamics in epitaxial growth. *Appl. Anal.*, 83:1015–1025, 2004.

3. F. Otto, P. Penzler, A. Rätz, T. Rump, A. Voigt. A diffuse-interface approximation for step flow in epitaxial growth. *Nonlinearity* 17 (2):477–49, 2004.

4. A. Rätz, A. Voigt. Various phase-field approximations for epitaxial growth. *J. Cryst. Growth*, 266:278–282, 2004.

5. A. Rätz, A. Voigt. Continuum modeling of nanostructure evolution. In P. Vincenzini, editor, *Proc. Computational Modeling and Simulation of Materials*, volume 44, pages 217–226. Techna Group, Advances in Science and Technology, 2004.

6. A. Rätz, A. Voigt. A diffuse step-flow model with edge-diffusion. In A. Voigt, editor, *Multiscale modeling of epitaxial growth*, volume 149 of *ISNM*, pages 115–126. Birkhäuser, Basel, 2005.

7. A. Rätz, A. Ribalta, A. Voigt. Surface evolution of elastically stressed films under deposition by a diffuse interface model. *J. Comput. Phys.*, 214 (1):187–208, 2006.

8. A. Rätz, A. Voigt. Higher order regularization of anisotropic geometric evolution equations in three dimensions. *J. Comput. Theor. Nanosci.*, 3 (4):560–564, 2006.

9. A. Rätz, A. Voigt. PDE´s on surfaces - diffuse interface approach. *Commun. Math. Sci.*, 4:3436–3445, 2006.

10. L. Balykov, V. Chalupecky, C. Eck, H. Emmerich, G. Krishnamoorthy, A. Rätz, and A. Voigt. Multiscale Modeling of Epitaxial Growth: From Discrete-Continuum to Continuum Equations. In A. Mielke, editor, *Analysis, Modeling and Simulation of Multiscale Modeling*, pages 65–85. Springer, 2006.

11. A. Rätz, A. Voigt. A diffuse-interface approximation for surface diffusion including adatoms. *Nonlinearity*, 20 (1): 177–192, 2007.